Experimental and Theoretical Studies of Reactive Transport Processes in Soluble Porous Rocks

by

Wei Li

B.S., Tsinghua University (2012)
S.M., Massachusetts Institute of Technology (2014)

Submitted to the Department of Civil and Environmental Engineering
in partial fulfillment of the requirements for the degree of

Doctor of Philosophy

at the

MASSACHUSETTS INSTITUTE OF TECHNOLOGY

June 2019

Signature redacted

Author . . . .
Department of Civil and Environmental Engineering
May 16, 2019

Certified by . . . . Signature redacted . . . .
Herbert H. Einstein
Professor of Civil and Environmental Engineering
Thesis Supervisor

Signature redacted

Accepted by . . . .
Heidi Nepf
Donald and Martha Harleman Professor
Chair, Graduate Program Committee

Experimental and Theoretical Studies of Reactive Transport Processes in Soluble Porous Rocks

by

Wei Li

Submitted to the Department of Civil and Environmental Engineering
on May 16, 2019, in partial fulfillment of the
requirements for the degree of
Doctor of Philosophy

Abstract

Underground reactive transport processes involve fluid flow and reactions (dissolution, precipitation, and pressure solution) driving the evolution of the rock-fluid systems, which may result in favorable processes such as increased oil production by reservoir acid stimulation, or undesired processes such as caves and subsidence. Flow and reaction in the rock matrix often induce wormholes, which are long, finger-like channels that form due to the dissolution heterogeneity in the matrix. These wormholes become major flow pathways, which greatly increase the permeability of the rock. To study the reactive transport processes and the formation of wormholes, experimental and theoretical studies were conducted.

More specifically, a new experimental setup and data analysis methods were introduced to the tube flow tests and core flood tests to experimentally study the evolution of the rock-fluid system. Theoretical studies with analytical and numerical models were used to simulate the experimental results and provide theoretical explanation for the experimental observations. Through the experimental and theoretical studies, this research improved the fundamental understanding of reactive transport processes in rock-fluid systems. This in turn provided accurate prediction of the evolution of the rock-fluid systems driven by the reactive transport processes.

Thesis Supervisor: Herbert H. Einstein
Title: Professor of Civil and Environmental Engineering

Acknowledgments

This thesis would not have been possible without the support and help from the following people.

First, I would like to express my deep and sincere gratitude to my advisor Professor Herbert H. Einstein. It has been a great honor and pleasure working with him, a great teacher, mentor and supervisor. His knowledge in a wide range of disciplines guided me through the challenges of accomplishing this work. He is always encouraging whenever I have a new idea to explore. His work ethic and enthusiasm encouraged me to overcome the obstacles in my research. He is compassionate and supportive, whenever life seems hard to me. He is truly a role model that I hope I can live up to.

I am also grateful to my committee members: Dr. Brown, Professor John Germaine, Professor Ruben Juanes and Professor Rita Sousa. I would like to thank Dr. Brown for his support and insights from a wide range of background. I want to thank Professor Germaine for providing such precious advice and hands-on assistance for my experimental design and methods. His knowledge of electronics, both analog and digital, have inspired my curiosity and passion of developing my own equipment for my tests. Professor Ruben Juanes provided great support to my work with his critical and insightful questions. His expertise in flow in porous media also expanded my vision in the research. Professor Rita Sousa provided enormous support in learning the GEOFRAC model and later the flow tests with gypsum.

I am grateful to have the opportunity to sit in the classroom of great professors. I would like to thank all the faculty who offered me the courses: Prof. Einstein, Prof. Whittle, Prof. Germaine, Dr. Jen, Prof. Juanes, Prof. Bathe, Prof. Ulm, Prof. Anand, and Prof. Bush. Thanks for all the wisdom, inspiration, ideas, stories, and of course knowledge.

The help of all the CEE staff is also deeply appreciated, especially Carolyn Jundzilo-Comer, Steven Rudolph, Pat Dixon, Kris Kipp, Kiley Clapper and Max Martelli. I would like to thank Carolyn for the sweet treats she brought us every week. I would like to thank Steven Rudolph's help in designing and manufacturing the experimental setup for my tests. He taught me so much in designing and machining.

I would also like to thank my colleagues in the research group. Professor Bruno Gonçalves da Silva who showed me his great life balancing skills being a father of two children and conducting rigid and careful experiments at the same time. Dr. Stephen P. Morgan who was like a big brother to the rest of group, always encouraging and passionate. Omar Al Dajani who has been the expert I turn to regarding field and industrial experience. He is always caring, supportive and easy to talk to. Bing Qiuyi Li, with his multi-cultural experience and great courage in his adventures showed me how life can be lived bravely and strongly. Working closely with Rafael L. Villamor and Hao Kang to setup the low pressure and medium pressure triaxial systems was an enriching experience. The lessons we learned, the problems we tackled and the final experimental setup we made possible have been one of the most unforgettable experience in my life. The visiting students, Victoire, Ray, Irina, Michael, Mohammad and Michela added a lot of fun to our group activities and shared a lot of interested life experience with us. I'm so lucky to be in this group for these years.

I'm grateful to my friend, Dan Li, for the being such a role model and good critic. I met him at Tsinghua University, and since then he have provided a lot of advice and help when I needed. I want to thank my friend, Xiaowei Zhang, for being such a great roommate, a big brother and a great example for life. In the four years we lived together, he was always there whenever I needed help.

To my dear parents, thank you for bring me to this wonderful world. Going to be a father of a child myself, I started to understand how hard it must be for letting their only child go living thousands of miles away. They tried to never let their problems get into my life, but they were always there when I needed them.

Finally, to my dearest wife, Guojun Cao, thank you for your love, strength, support and sense of humor. The five years I know you and loved you, I enjoyed every part of it. You made me a better man. Thank you for understanding me and giving me company all the time. I love you with all my heart and I look forward to spending the rest of our lives together.

Contents

List of Figures

List of Tables

Chapter 1

Introduction

Reactive transport processes in general consist of two processes: reaction and mass transport. The interplay between the reactions and mass transport drives the evolution of the rock-fluid systems in various space and time scales. In the underground rock-fluid systems, the reactive transport processes play an important role in a number of natural and industrial settings: (1) formation of karst; (2) glacier cave formation; (3) deeper Earth systems, such as earthquakes and ocean floor hydrothermal venting [Berkowitz, 2002]; (4) reservoir exploitation for water supply [Benito et al. 1995; Johnson, 2008]; (5) contaminant transport from subsurface waste repositories; (6) petroleum reservoir exploitation; (7) geothermal reservoir exploitation and heat storage; (8) mining and mineralization processes (in situ leaching and location of ore bodies); and (9) geotechnical applications (including effects on underground storage reservoirs, tunnels and other structures) [Cooper, 1986].

In the underground rock-fluid systems, the common reactions are dissolution and precipitation. The reactions affect the mass transport by changing the geometry of the flow paths such as holes, fractures and pores. The mass transport in turn affects reactions by changing the concentration of the solute in the fluid that reacts with the solid. Depending on the type of reaction and mass transport, positive or negative feedback between the reaction and transport can be observed in experimental and theoretical studies. It is important to have a fundamental understanding of the reactive transport processes and an accurate prediction of the evolution of the rock-fluid system.

1.1 Research Objectives

Given the importance of reactive transport processes in natural and industrial settings, the fundamental understanding of the reactive transport processes and accurate prediction of the evolution of the rock-fluid systems driven by reactive transport processes are the two main objectives of the research. New experimental setup and data analysis methods were introduced to the tube flow tests and core flood tests to experimentally study the evolution of the rock-fluid system driven by reactive transport processes. In the theoretical studies, analytical and numerical models were developed to simulate the experimental results, provide theoretical explanations for the experimental observations, and predict the evolution of the rock-fluid system. Through the experimental and theoretical studies, the two main objectives of the research were satisfied.

In the experimental study, the objectives were to study the reactive transport processes in a preexisting cylindrical tube in soluble rock and in the porous rock matrix. The experimental study started with flow in cylindrical tube as a simplified geometry for rock cavities in general (fractures and wormholes). Tube flow tests were conducted on this initial well-characterized geometry to study the evolution of the rock-fluid system resulting from different flow rates. The geometry of the tubes after the tube flow tests is also studied. The tube flow tests answer the research questions: how the geometry of the tube evolves, and how the dissolution kinetics evolves. The tube flow tests also serve as the experimental validation of the corresponding theoretical studies.

The experimental study then focused on the flow and dissolution in porous rock matrix. Similar to the tube flow tests, the evolution of the rock-fluid system regarding the permeability and dissolution kinetics are the major research questions to be answered. The wormholes resulting from different flow rates can be used to investigate the effect of flow rate on the formation of wormholes. Both the tube flow tests and core flood tests require good quality effluent concentration data to study the evolution of dissolution kinetics in the rock-fluid system. In addition, the dissolution induced changes, for example the final tube geometry and wormholes, need to be precisely captured to study the effect of dissolution. In this experimental study, an effluent chemistry monitoring system and 3D quantitative CT data analysis algorithms are developed to facilitate the effluent concentration measurement and geometric analysis. The dissolution in the tube and dissolution in porous rock matrix are studied with these advanced experimental methods to better understand the evolution of the rock-fluid system due to dissolution.

In the theoretical study, the flow and dissolution in a preexisting cylindrical tube in gypsum are studied first. As the flow and dissolution transform this tube into an enlarged tapered tube, the flow condition and boundary shape do not match the assumptions of the Graetz solution (Graetz, 1882) any more. A new analytical solution needs to be developed to model the flow and dissolution in an enlarged tapered tube. The experimental results of the tube flow tests can also be used as validation of this analytical solution. Then, dissolution in the porous rock matrix and formation of wormholes are studied theoretically based on the core flood tests. Dimensional analysis is used to study the controlling mechanism of dissolution in the porous medium and the wormholes. With a better understanding of the controlling mechanism, new physical insights can be gained from the experimental observations regarding the evolution of the dissolution kinetics. A new model is developed to predict the evolution of the rock-fluid system.

In sum, this research aims to use advanced experimental methods and new analytical models to achieve the fundamental understanding of the reactive transport processes and accurate prediction of the evolution of the rock-fluid systems driven by the reactive transport processes.

1.2 Thesis Structure

This thesis is structured as follows:

Chapter 2 presents an overview of the research background including the common dissolution processes in underground rock-fluid systems, the types of underground flows, and physical processes that control dissolution. A literature review of the current state of experimental and theoretical research regarding reactive transport processes is also presented.

In Chapter 3, the experimental setup and the testing processes are documented. The material used in this research, gypsum, is characterized in detail. The specimen preparation processes and the material properties resulting from these processes are discussed. The design and working principle of the effluent chemistry monitoring system (ECMS) is presented. The triaxial system used for the tube flow tests and core flood tests is described. Then, the experimental processes are discussed step by step for the tube flow tests and core flood tests. The work flow for the CT scan analysis after the flow tests is described.

In Chapter 4, the experimental results of the tube flow tests and core flood tests are analyzed and discussed. For the flow test on a preexisting cylindrical tube, the effluent concentration measured by the ECMS are used to study the evolution of the dissolution kinetics under different flow rates. The geometry of the tubes resulting from different flow rates are studied based on CT scanning. For the core flood tests, the pressure difference between the inlet and outlet and the effluent concentration are analyzed to study the evolution of the rock-fluid system during the core flood tests. The wormhole geometries resulting from different flow rates are analyzed with the help of 3D topological and morphological algorithms to study the effect of flow rate on wormhole formation.

In Chapter 5, an analytical model, the extended Graetz solution, is developed to simulate the dissolution in an enlarging tapered tube and evolving wormholes. A numerical model and the tube flow test results are used to validate the extended Graetz solution. In parallel, a continuum model was developed to simulate the dissolution in the rock matrix. They are followed by the development of a model for core flood tests combining the continuum model and the extended Graetz solution to simulate the growth of the wormholes, wormhole breakthrough, and the evolution of dissolution kinetics induced by wormhole formation. The results of the models are compared with the core flood test results.

Chapter 6 summarizes the results and findings of the research and gives recommendations for future work.

Chapter 2

Background

This background chapter includes the definition of reactive transport process, as well as an extensive literature review of previous experimental and theoretical research conducted on the reactive transport processes in various rock-fluid systems. The reactive transport process is defined by introducing the common reactions and transport processes and discussing how the two processes are coupled. A review of previous experimental work conducted on various rock-fluid systems is presented. This chapter finishes with a review of reactive transport modeling using analytical and numerical models.

Given the various reactions and transport processes in the complex Earth system, reactive transport process occur over a wide range of temporal and spatial scales. Li et al. [2017] developed a schematic of the temporal and spatial scales at which the reactive transport processes are relevant, as shown in Figure 2-1. The studies presented in the thesis cover parts of the fields of hydrogeology and geomorphology in Figure 2-1. Also, the following sections only focuses on the processes that are relevant to the experimental and theoretical research.

2.1 Reactions in Underground Rock-Fluid Systems

The reactions in underground rock-fluid systems include geochemical reactions (e.g., mineral dissolution and precipitation, ion exchange, surface complexation), and bio-

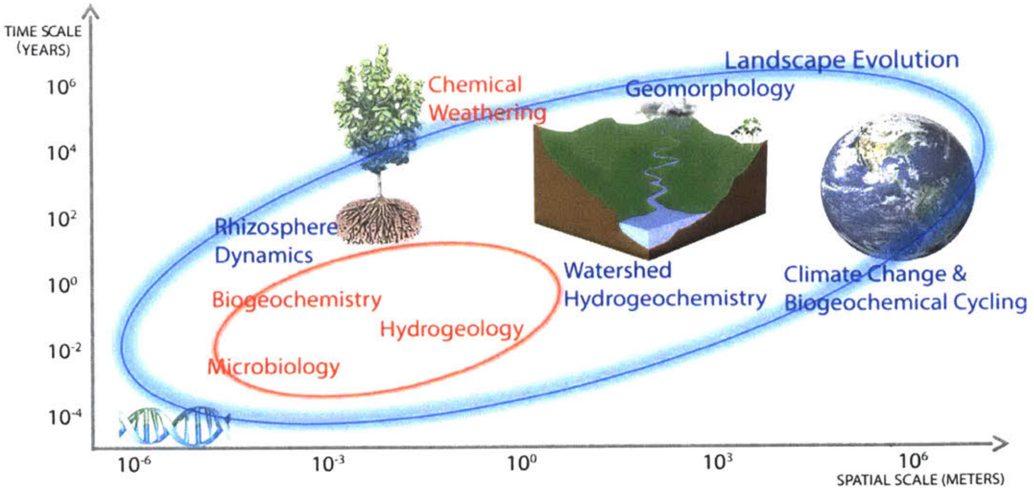

Figure 2-1: Reactive transport processes occur at a wide range of temporal and spatial scales [Li et al., 2017]. The red circle indicates the processes that researchers have been interested in studying in the past three decades. The blue circle reflects the overall scale where it is relevant.

geochemical reactions (e.g., microbe-midiated redox reactions, biomass growth and decay) [Li et al., 2017]. In this study, only dissolution reactions are investigated in the context of the reactions in the underground rock-fluid systems.

Dissolution describes a mixing process. In the context of this study, the discussion of dissolution is limited to the mixing of a solid in an aqueous solution. The dissolution of a solid in an aqueous solution without further chemical reaction of the dissolved ions involves two processes: the chemical reaction at the solid-fluid interface and the mass transport of the ions away from the interface. In this section, the common chemical reactions at the solid-fluid interface are presented first. Then, the dissolution mechanisms are discussed by comparing the reaction rate and mass transport rate. The section ends by introducing the experimental methods to determine the reaction rate.

2.1.1 Chemical Reactions

The chemical reactions at the solid-fluid interface are usually reversible. When the solution can no longer dissolve the solute, the solute and solvent reaches thermodynamic equilibrium, which is referred to as saturated solution. The equilibrium concentration

Table 2.1: Soluble minerals

Mineral class	Mineral name	Chemical Composition
Chlorides	Halite	$NaCl$
	Sylvite	KCl
	Carnallite	$KMgCl_3 \cdot 6H_2O$
	Kainite	$KMgSO_4 \cdot 3H_2O$
Sulfates	Anhydrite	$CaSO_4$
	Gypsum	$CaSO_4 \cdot 2H_2O$
	Kieserite	$MgSO_4 \cdot H_2O$
	Langbeinite	$K_2Mg_2(SO_4)_3$
	Polyhalite	$K_2Ca_2Mg(SO_4)_6 \cdot H_2O$
Carbonates	Dolomite	$CaMg(CO_3)_2$
	Calcite	$CaCO_3$
	Magnesite	$MgCO_3$

is also referred to as the solubility. When the solution is under-saturated, the solute continues to dissolve in the solvent. When the solution is over-saturated, the solute precipitates from the solution.

In the dissolution processes in the underground rock-fluid systems, the solvents are usually water or an acidic aqueous solution, while the solutes are soluble minerals. Some of the rocks containing water-soluble minerals are often referred to as evaporites, because of their crystallization process usually involves evaporation of water. Common water-soluble or slightly soluble minerals are summarized by their class in Table 2.1.

The chemical reactions related to the dissolution of some minerals, for example gypsum ($CaSO_4 \cdot H_2O$) dissolution in water, is a simple dissociation process. The gypsum at the gypsum-water interface dissociates into calcium ions and sulfate ions:

$$CaSO_4 \cdot H_2O(s) \rightleftharpoons Ca^{2+}(aq) + SO_4^{2-}(aq) + 2H_2O. \tag{2.1}$$

The existence of other ions affects the dissolution of gypsum, but not to a significant extent. The equilibrium concentration of gypsum in water is around 2.6g/L. The chemical reactions related to the dissolution of other minerals, such as calcite ($CaCO_3$), is more complicated. The partial pressure of CO_2 from the atmosphere also affects the chemical equilibrium of calcite dissolution in water. The related reactions are listed as follows:

$$\mathrm{H_2O} + \mathrm{CO_2}(aq) \rightleftharpoons \mathrm{H_2CO_3}(aq); \tag{2.2a}$$

$$\mathrm{H_2CO_3}(aq) \rightleftharpoons \mathrm{HCO_3^-}(aq) + \mathrm{H^+}(aq); \tag{2.2b}$$

$$\mathrm{CaCO_3}(s) + \mathrm{HCO_3^-}(aq) + \mathrm{H^+}(aq) \rightleftharpoons \mathrm{Ca^{2+}}(aq) + 2\mathrm{HCO_3^{2-}}(aq). \tag{2.2c}$$

As shown in Equation (2.2), the dissolution of calcite is affected by the amount of CO_2 in water. The chemical equilibrium of calcite-water solution is determined by not only the temperature but also the partial pressure of CO_2. At atmospheric levels of ambient CO_2, the equilibrium concentration of calcite in water is around 47mg/L.

In the field of petroleum engineering, acid stimulation has been a common method to increase the permeability of reservoirs and enhance oil production. The operation of acid stimulation uses acid to dissolve the formation rock. The choice of acid depends on the formation. Hydrochloric acid (HCl) is used for carbonate reservoirs, while hydrofluoric acid (HF) is used for sandstone reservoirs.

In reservoir conditions, the product of the reaction, CO_2, is usually in the aqueous solution phase instead of gas phase because of the high pressure, as shown in Equation (2.3).

$$\mathrm{CaCO_3}(s) + 2\mathrm{HCl}(aq) = \mathrm{Ca^{2+}} + 2\mathrm{Cl^-} + \mathrm{H_2}O + \mathrm{CO_2}(aq) \tag{2.3}$$

Quartz will in general not be attacked by acids. The prominent exception is hydrofluoric acid (HF), which decomposes quartz to form first silicon fluoride SiF4, then hydrofluorosilicic acid,

$$SiO_2(s) + 6HF(aq) = H_2SiF_6(aq) + 2H_2O. \tag{2.4}$$

The chemical reactions discussed above are common reactions that lead to the dissolution of rock minerals. However, the dissolution is not only controlled by the chemical reactions but also the mass transport. The experimental methods to measure rate of the chemical reactions are introduced after the discussion of the controlling mechanisms for dissolution.

2.1.2 Dissolution Mechanisms

As discussed by many researchers [Jeschke et al., 2001; Li and Einstein, 2017], the dissolution of a solid in an aqueous solution without further chemical reaction of the dissolved ions is controlled by two processes: the chemical reaction at the solid-fluid interface and the mass transport of the ions away from the interface. Figure 2-2 shows the dissolution process in a gypsum-water system: the calcium ions and sulfate ions dissociate at the interface, then they diffuse from the interface to the adjacent fluid and are transported further away from the interface. The mass transport in this case includes ion diffusion from the interface and advection with the flow of fluid. Therefore, there are three processes in total that influence the dissolution, namely: reaction, diffusion and advection.

Among the three processes, the slowest process is the limiting mechanism for the dissolution. Based on the limiting mechanism, the dissolution is characterized as reaction-controlled dissolution or transport-controlled dissolution. In a reaction-controlled dissolution system, the reaction rate is lower than the diffusion process and advection process. The interface between the fluid and solid is not in thermodynamic equilibrium, so the reaction at the interface controls the dissolution rate. Since the mass transport is relatively fast, the solute concentration in the solvent is relatively uniform (Figure 2-3(a)). In a transport-controlled dissolution system, the mass transport (diffusion or advection) from the interface to the fluid is slower than the reaction. The reaction is so fast to make up for the diffused ions that the interface

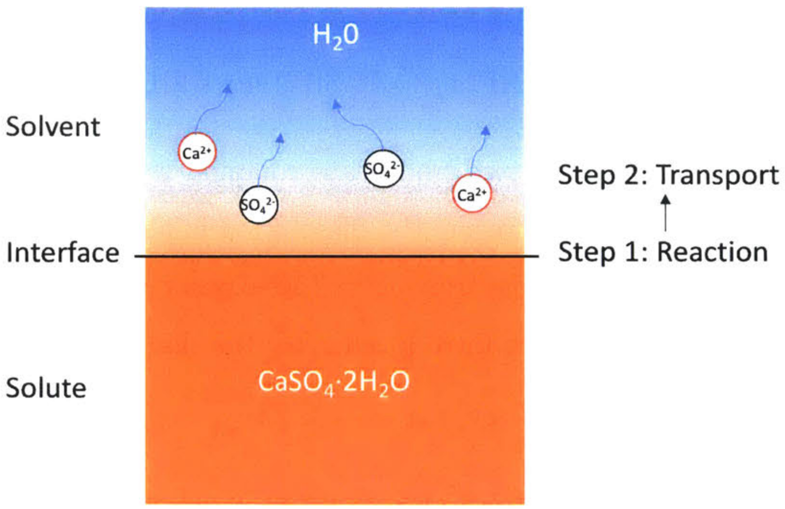

Figure 2-2: A schematic of dissolution of a solid in an aqueous solution.

between the fluid and solid is in thermodynamic equilibrium. Since the mass transport is relatively slow, the solute concentration in the solvent is not uniform (Figure 2-3(b)). In the underground rock-fluid systems, the dissolution of gypsum in water is generally considered as transport-controlled, while the dissolution of calcite in water is generally considered as reaction-controlled.

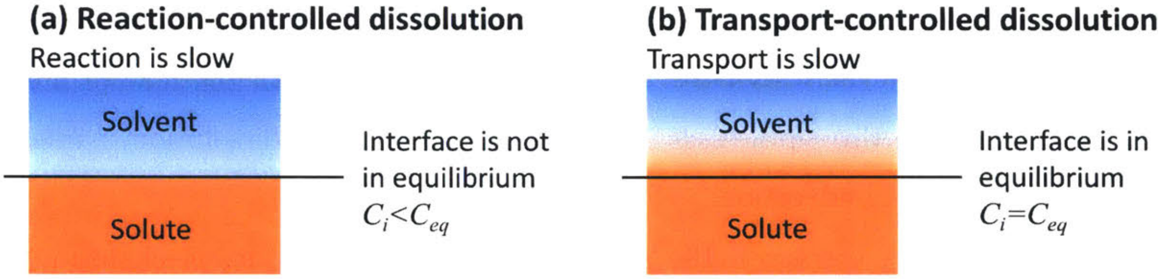

Figure 2-3: A schematic of reaction-controlled dissolution and transport-controlled dissolution. (a) Reaction-controlled dissolution. (b) Transport-controlled dissolution.

Dimensional analysis is often used to determine the control mechanisms of the dissolution. In the dimensional analysis, dimensionless numbers are defined as the ratio of the rate of one process to the other to compare the rates of the two processes. For example, the Damköhler number (D_a) is defined as the ratio of reaction rate to diffusion rate. When $D_a \ll 1$, the reaction rate is much slower than diffusion rate, the dissolution is reaction-controlled. The detailed definition will be discussed in Section

5.2.

2.1.3 Chemical Reaction Rate Measurement

Understanding the three processes involved in the dissolution process also inspired the experimental design for measuring the rate of chemical reaction in a dissolution process. The reaction rate (R) is often defined as the rate of change for the amount of substance, or mass of substance:

$$R = \frac{\partial n_i}{\partial t} \text{ or, } R = \frac{\partial m_i}{\partial t}, \tag{2.5}$$

where n_i is the amount of the substance i in moles; m_i is the mass of the substance i. Similarly, the dissolution rate is defined as the rate at which the solid dissolved into the solvent. When the dissolution is reaction controlled, the dissolution rate is the same as the reaction rate.

Reaction rates are often measured using crushed minerals in well-mixed laboratory systems [Li et al., 2006]. These systems uses stirrers or rotating plates to induce high mass transport rate so that the dissolution is reaction-limited. Hence the rate of reaction in a dissolution process can be measured by measuring the dissolution rate. The rotating disk method (Figure 2-4) has been used to study the dissolution kinetics of gypsum by various researchers [Barton and Wilde, 1971; Innorta et al. 1980; Gobran and Miyamoto, 1985; Raines and Dewers, 1997]. The rotation of a disk initiates transport due to advection and diffusion, such that the reaction rate coefficient is a function of the rotation speed. Liu and Nancollas [1970, 1971 and 1973] conducted a series of experiments to study the dissolution and precipitation of calcium sulfate dihydrate at different temperatures and in the presence of other ions using pure synthesized uniform gypsum crystals. Jeschke et al. [2001] used both the batch tests and the rotating disk method to study the influence of temperature and of salinity.

Figure 2-4 shows a schematic of the rotating disk setup. The mineral of interest is ground into powder form and hard pressed into the blind hole at the center of the disk. The mineral can also be polished to a pill shape that fits into the blind hole at the center of the disk. The rotation of the disk induces a centrifugal flow (Figure 2-5(a)), which in turn through mass conservation induces an upward flow pointing at the mineral (Figure 2-5(b)) [Raines and Dewers, 1997]. The mass transport of the flow has been well characterized by Levich [1962]. By increasing the rate of rotation, the rotating disk setup creates a high mass transport rate so that the dissolution is reaction-controlled and the rate of which can be measured.

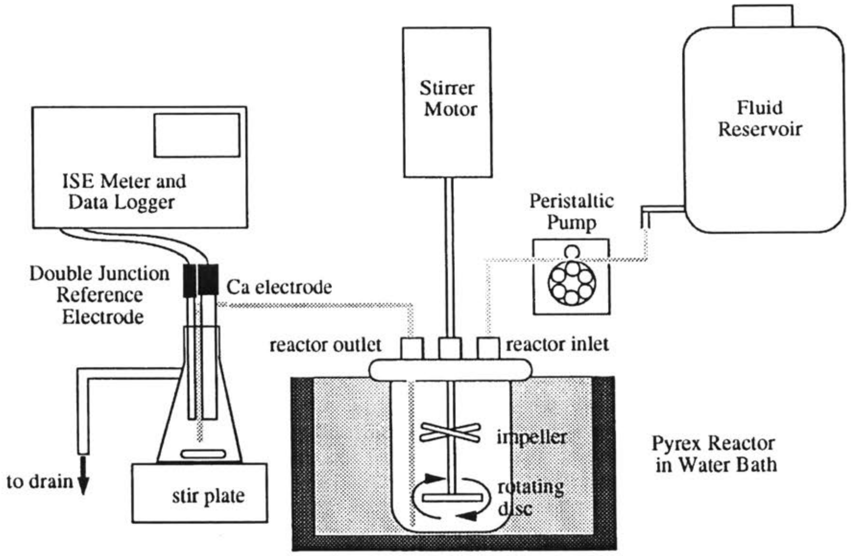

Figure 2-4: Rotating disk method for reaction rate measurement [Raines and Dewers, 1997]

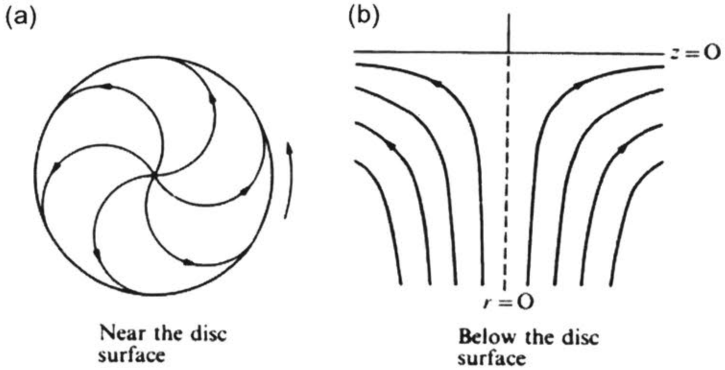

Figure 2-5: Flow in a rotating disk apparatus [Levich, 1962]. (a) Flow on the bottom surface of the rotating disk. (b) Vertical flow near the bottom surface of the rotating disk.

Similarly, the dissolution reaction rate is measured in batch tests by dissolving well characterized (size, surface area) pure mineral crystals in the solvent. Magnetic stirrers are often used to create a high mass transport rate so that the dissolution is reaction-controlled and the rate of which can be measured.

During the rotating disk test or batch test, the concentration of the solution (C) in the vessel is monitored continuously using ion specific probes or electric conductivity probes. The dissolved solid in the vessel is: $V_c \cdot C$, where V_c is the volume of the solution. As defined in Equation 2.5, the reaction rate is:

$$R = \frac{\partial V_c \cdot C}{\partial t}. \tag{2.6}$$

The measured dissolution flux q_w is the reaction rate normalized by the area of the solid-solvent interface area A_c, which can be expressed as:

$$q_w = \frac{1}{A_c} \cdot \frac{\partial V_c \cdot C}{\partial t}. \tag{2.7}$$

For the rotating disk method, the solid-solvent interface area (A_c) is the cross section area of the blind hole, where the solid sits in. For the batch test with crystals, the solid-solvent interface area (A_c) is the total surface area of the crystals. The general rate equation for the dissolution can be expressed as:

$$q_w = \kappa \left(1 - \frac{C}{C_{eq}}\right)^{n_r}, \tag{2.8}$$

where κ is the intrinsic reaction rate coefficient; n_r is the order of reaction. Equations (2.7) and (2.8) are used to calculate the reaction rate coefficient κ, based on the test results. When the reaction is first-order, the dissolution flux is also expressed as:

$$q_w = k_r(C_{eq} - C), \tag{2.9}$$

where k_r is the reaction rate coefficient. Based on Equations (2.8) and (2.9), $k_r = \kappa \cdot C_{eq}$. The dissolution of common minerals is usually first-order, or can be approximated as first order, so the formulation in Equation (2.9) is often used.

2.2 Flow in Underground Rock-Fluid Systems

Flow occurs in various underground rock-fluid systems: groundwater flow in the aquifers, oil flow in underground oil reservoirs, natural gas flow in the gas rich shale formations, seepage in rock fractures, underground rivers in karst formations, and flow in glacial caves. According to the fluid properties, the flow in underground rock-fluid systems can be categorized as: single-phase or multi-phase flow, compressible- or incompressible flow. According to the flow conductive media, the flow can be categorized as: flow in the porous matrix, flow in wormholes, flow in fractures, and flow in open channels. In this research, only the incompressible single-phase flow in the porous matrix, wormholes and fractures is studied. A brief background will be provided for these types of flow in the following sections.

2.2.1 Flow in Porous Matrix

The fluid flow in the porous matrix has been well studied in the field of groundwater hydrology and petroleum engineering. The experimental study was pioneered by Darcy, [1856], when he investigated the flow through packed sand. Figure 2-6 shows a schematic of the experimental setup. Different hydraulic heads were used to produce flow through the packed sand, while the corresponding flow rates were measured.

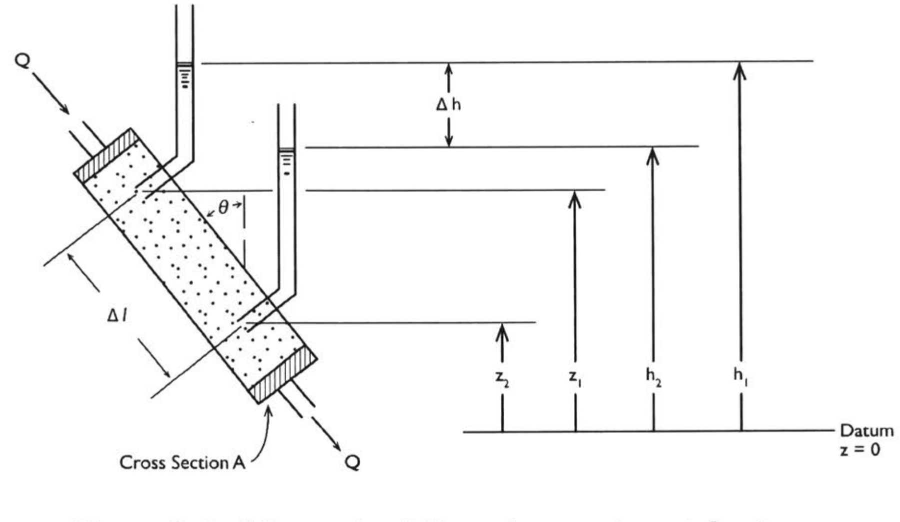

Figure 2-6: Schematic of Darcy's experimental setup.

Based on his experiments, Darcy [1856] concluded that the flow rate through the porous medium (Q) is proportional to the head loss (Δh) and is inversely proportional to the length of the flow path (Δl). This empirical relation is Darcy's law:

$$Q = A \cdot K \frac{\Delta h}{\Delta l}, \tag{2.10}$$

where K is the hydraulic conductivity. The flow rate (Q) normalized by the cross-section area (A) is the flux (q), which is defined as the Darcy velocity (u). The head loss (Δh) over the length of flow path (Δl) is the hydraulic gradient (i_h). Therefore, Darcy's law can also be simplified as:

$$q = u = K \cdot i_h. \tag{2.11}$$

Darcy's experiment was designed for the flow of groundwater in porous media. The property of the fluid (water) is accounted for in the hydraulic conductivity (K). However, in the petroleum industry, the property of the fluid (oil) varies from reservoir to reservoir. Another parameter, permeability (k) is introduced to quantify the ability of the rock matrix in conducting the fluid. In this case, Darcy's law is expressed as:

$$u = \frac{k}{\mu} \frac{\Delta P}{\Delta l}, \tag{2.12}$$

where μ is the dynamic viscosity; and ΔP is the pressure difference along the direction of Δl. By taking the vector form of the Darcy velocity in 3D dimensional space and accounting for the gravitational effect, Darcy's law can be expressed as:

$$\mathbf{u} = -\frac{1}{\mu}\mathbf{k}(\nabla P - \rho \mathrm{g}), \tag{2.13}$$

where $\mathbf{u}$ is the Darcy velocity vector ($\mathbf{u} = (u_1, u_2, u_3)$); $\mathbf{k}$ is the permeability tensor; ∇P is the gradient of pressure; ρ is the density of the fluid; $\mathbf{g}$ is the gravitational constant vector. The permeability tensor:

$$\mathbf{k} = \begin{bmatrix} k_{11} & k_{12} & k_{13} \\ k_{21} & k_{22} & k_{23} \\ k_{31} & k_{32} & k_{33} \end{bmatrix}, \tag{2.14}$$

accounts for the dependence of flow rate in one direction on pressure differences in the same and orthogonal directions. The relation between the hydraulic conductivity and the permeability can be expressed as:

$$K = \frac{\rho g}{\mu} k \tag{2.15}$$

Darcy's experimental study proposed the linear relation between flow rate and pressure gradient. It is valid for laminar flow through porous media. The scale, at which the Darcy's law is valid, is limited. For example, the Darcy's law will not hold at the scale of individual pores. A representative elementary volume (REV) needs to be properly defined to represent the properties of the porous matrix. The length scale of the REV could be millimeters for studying flow in fine-grained sandstone, and kilometers for studying the flow in an oil reservoir. The scale of REV is also referred to as Darcy scale.

With the improvement of imaging technology, the pore structure in a porous medium can been observed in 3D using the X-ray computed tomography (CT). Computational fluid dynamics simulations have been applied based on 3D models of porous media. Figure 2-7 shows the flow streamlines in a small porous rock cube [Muljadi et al., 2016]. The flow paths are tortuous and not uniformly distributed over the porous rock. To resolve the detailed features of the flow, a very fine mesh is needed and a high number of elements or nodes are needed. These simulations usually require high computational power, and can only simulate porous media in the scale of centimeters. This scale of study is also known as pore scale.

The methodology of Darcy's law is to capture the averaged over all flow at the scale of the REV without worrying about the detailed flow velocity in each pore. This method is effective especially at the large scale simulations where the REV can

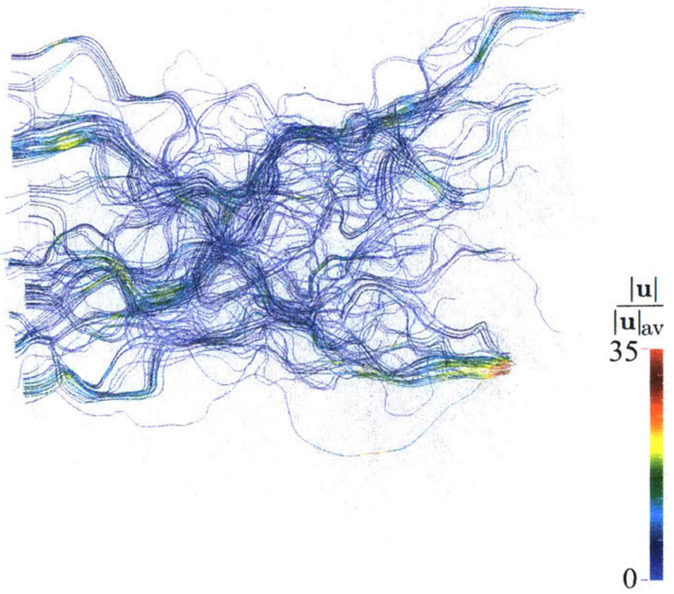

Figure 2-7: Computational fluid dynamics simulation of the flow in a porous rock [Muljadi et al., 2016].

be at the scale of meters. On the other hand, the pore scale studies have provided fundamental understanding on the complex flow field in the pore networks. It also provided an accurate basis for studies at Darcy scale.

2.2.2 Flow in Fractures

In underground formations, natural fractures (related to tectonic history, near surface geomorphologic processes, cooling) and artificially induced fractures (excavation, hydraulic fracturing) are common. They are major flow pathways in the underground rock-fluid systems due to their high conductivity. The existence of fractures in a porous medium could significantly affect the behavior of the rock-fluid system during reactive transport processes. The flow in single fractures and fracture networks has been studied extensively for enhanced geothermal systems, nuclear waste storage, hydraulic fracturing for shale gas, and carbon sequestration.

The flow in a single fracture is often idealized as flow between two parallel plates [Witherspoon et al., 1980], as shown in Figure 2-8. The fluid flows between two plates both parallel to the $x - y$ plane. The distance between the two plates (aperture) is

2δ. The flow is only in the x direction, for which the velocity profile is a function of z ($u = u(z)$)

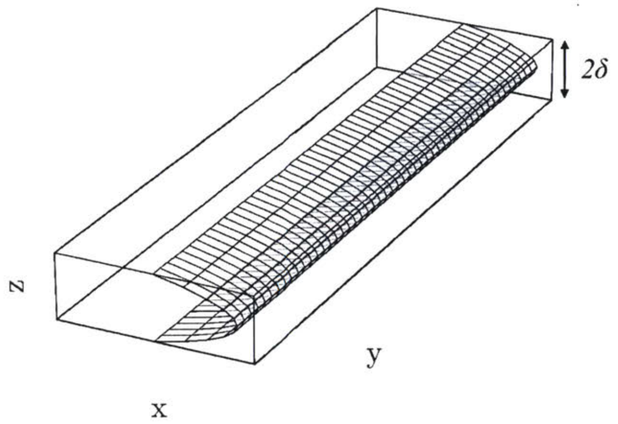

Figure 2-8: Velocity profile of steady state laminar flow between two parallel plates [Witherspoon et al., 1980].

The governing equation for the steady-state laminar flow can be derived by simplifying the Navier-Stokes equation:

$$\frac{\partial P}{\partial x} = \mu \frac{\partial^2 u}{\partial z^2}, \tag{2.16}$$

where P is the pressure; μ is the dynamic viscosity, and u is the velocity in x direction. With a no slip boundary condition $u|_{z=\pm\delta} = 0$ and symmetric boundary conditions $\frac{\partial u}{\partial z}|_{z=0} = 0$, the differential equation has the solution:

$$u(z) = -\frac{1}{2\mu}\frac{\partial P}{\partial x}(\delta^2 - z^2). \tag{2.17}$$

In Equation (2.17), the negative sign indicates that the flow direction is the direction of pressure decrease. The velocity profile along the aperture direction (z) is parabolic as indicated by Equation 2.17 and shown in Figure 2-8. By integrating velocity along the direction of the aperture, the flow rate in the fracture is:

$$Q = -\frac{1}{12\mu}\frac{\partial P}{\partial x} w(2\delta)^3, \tag{2.18}$$

where w is the width of the fracture. Since the flow rate is proportional to the cube of the aperture ($(2\delta)^3$), Equation (2.18) is often called the "cubic law" [Witherspoon et al., 1980; Zimmerman et al., 1991].

The cubic law provides a good theoretical estimation of the conductivity of the fractures. However, the flow in a natural fracture is much more complicated than the ideal case of parallel plates. The surface roughness of a fracture, the variation of aperture, the tortuosity of the flow path and the contact areas in the fracture all add to the complexity of the flow in a natural fracture.

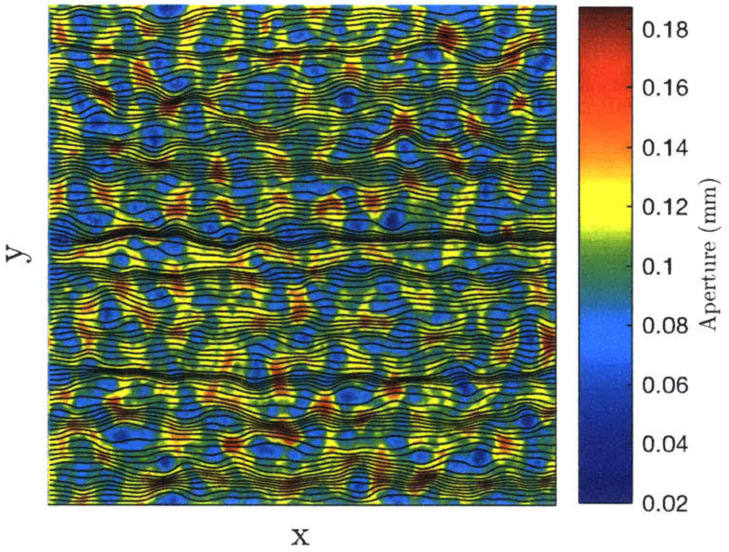

Figure 2-9: Aperture field and flow streamline resulting from local cubic law simulation [Kang et al., 2016].

To simulate the flow in a single natural fracture, the cubic law is integrated into numerical models. These model discretize the natural fracture into grid blocks each with a constant aperture. Each grid block is simulated locally using the cubic law, while the flow among all the blocks is balanced using mass conservation. These numerical models are often referred to as "local cubic law models". The local cubic law is effective in simulating the flow and mass transfer in a single fracture with known aperture field [Kang et al., 2016]. In Figure 2-9, the flow in a natural fracture is simulated with color indicating the aperture field and streamlines indicating the flow. The flow concentrates in areas where the fracture aperture is larger, which is also known as flow channeling.

The local cubic law assumes that the flow is laminar and that the cubic law holds at the scale of the grid block. However, the local cubic law tends to overestimate the permeability of the fracture because it neglects the surface roughness. Computational fluid dynamics is also applied to study the local turbulence caused by the surface roughness in the fracture. Figure 2-10 shows the cross section of a fracture with rough upper and lower surfaces [Briggs et al., 2017]. The major flow streams look laminar, which is also confirmed by the Reynolds number ($Re = 500$). However, there is local turbulent flow as indicated by the vortices near the rough surfaces. These vortices not only affect the prediction of flow, but also add complexity when estimating dissolution or precipitation.

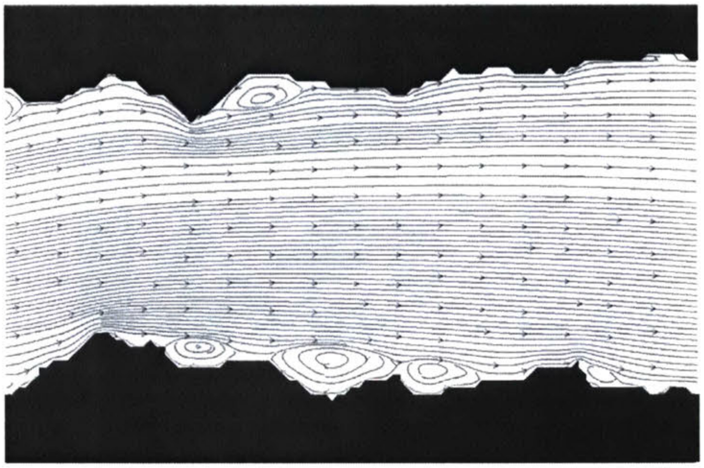

Figure 2-10: Simulated flow streamlines in a fracture at a Reynolds number of 500 [Briggs et al., 2017].

2.2.3 Flow in Wormholes

The flow and dissolution in porous media and fractures often induce wormholes, which are long, finger-like channels that form due to the flow and dissolution heterogeneity in the porous matrix and fractures, respectively. These wormholes become major flow pathways, which significantly increase the permeability of the rock. Figure 2-11 shows the wormholes in a gypsum specimen after a core flood test, of which the details will be discussed in Chapter 3. The wormholes developed from the inlet (bottom) of the specimen, but only one major wormhole reached the outlet (top). There are a lot of branches developed on the major wormhole. Despite the complex geometry of the wormholes, the flow in each wormhole can be approximated using pipe flow.

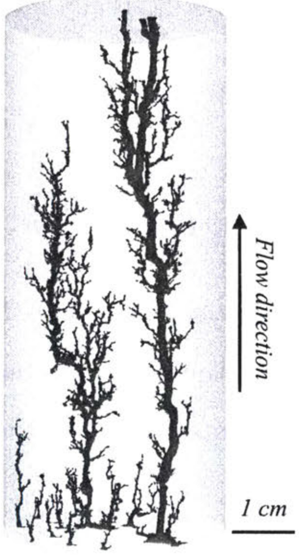

Figure 2-11: Wormholes resulting from core flood tests (refer to Section 4.2.5).

The governing equation for the steady-state laminar flow can be derived by simplifying the Navier-Stokes equation in cylindrical coordinates ($r - x$):

$$\frac{\partial P}{\partial x} = \mu \frac{1}{r} \frac{\partial}{\partial r} \left(r \frac{\partial u}{\partial r} \right). \tag{2.19}$$

With no slip boundary conditions $u|_{r=\pm R} = 0$ and symmetric boundary conditions $\frac{\partial u}{\partial r}|_{r=0} = 0$, the differential equation has the solution:

$$u(r) = -\frac{1}{4\mu} \frac{\partial P}{\partial x} (R^2 - r^2). \tag{2.20}$$

In Equation (2.20), the negative sign indicates the flow is in the direction in which the pressure decreases. The velocity profile in the radial direction is parabolic, as shown in Figure 2-12. By integrating velocity in the radial direction, the flow rate

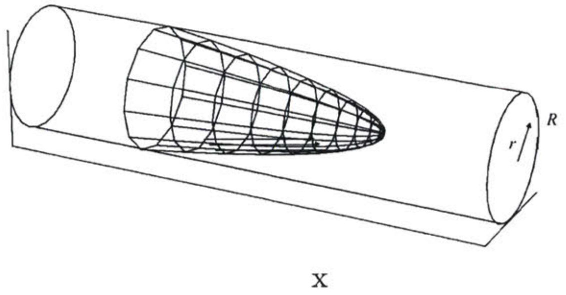

Figure 2-12: Velocity profile of steady state laminar flow in a tube.

in the pipe can be expressed as:

$$Q = -\frac{\pi}{8\mu}\frac{\partial P}{\partial x}R^4. \tag{2.21}$$

Equation (2.21) is also known as Poiseuille's law, which indicates that the flow rate in the pipe is proportional to the fourth power of the pipe radius. Equation 2.21 also shows that the flow rate is proportional to the pressure gradient in the pipe.

2.2.4 Summary of Flow in Underground Rock-Fluid Systems

In the above three sections, the types of flow in a porous matrix, fractures and wormholes are introduced briefly. In underground rock-fluid systems, the flow rate is usually low, so the flow is laminar. A similarity among these types of flow is that the flow rate is proportional to the pressure gradient, therefore, one type of flow could be used to simulate the other. Flow in tube networks was used to simulate the flow in fracture networks by Groves and Howard [1994a]. Flow between parallel plates was used simulate flow in porous media, for example, the Hele Shaw cell experiments [Faisal, 2015].

In the underground rock-fluid systems, the flow could be either one of the above three cases or combinations of them. However, due to the drastic difference in conductivity, usually the flow path with high conductivity will be dominant. For example, when there are fractures in a porous matrix, the flow will usually concentrate in the fractures instead of the porous matrix.

2.3 Reactive Transport Processes

Reactive transport processes in the underground rock-fluid system involve reactions (geochemical- and biogeochemical reactions) and fluid flow (flow in the porous matrix, fractures, and wormholes) driving the evolution of the rock-fluid systems. The reaction and mass transport are two processes that are coupled in various ways and that direct the system evolution in various directions.

More specifically, the reactions affect the mass transport by changing the geometry of the flow paths and the fluid properties. For example, dissolution and precipitation in the rock-fluid system are accompanied by widening and narrowing of the flow paths, respectively. These flow paths include the pore network, fractures and wormholes. Dissolution and precipitation also affect the concentration of solute in the fluid, which changes the density and viscosity of the fluid. The change in the flow paths and fluid properties affect the mass transport by changing the flow distribution, flow velocity and flow type. For example, the flow and dissolution in the porous rock matrix usually induces wormholes, which gather almost all the flow. The flow type changes from matrix flow to wormhole flow.

The mass transport in turn affects reactions by influencing the contact area and contact time between the rock and reactive fluid. For example, the reactive fluid flowing in the porous rock matrix usually has larger contact area and longer contact time with the rock, while the reactive fluid flowing in wormholes and fractures has smaller contact area and shorter contact time. The flow also affect the length of the entrance region, which affect the thickness of the diffusion layer, which will be discussed in detail in Chapter 5. Depending on the type of reaction and mass transport, the two coupled processes could enhance or hinder each other resulting in a positive or negative feedback, respectively. The positive or negative feedback between the reaction and mass transport have been observed in both theoretical and experimental studies [Elkhoury et al., 2013; Ameli et al., 2014]

The reactive transport processes in underground rock-fluid systems occur at various time and dimension scales. Natural rock dissolution such as limestone and gypsum karst formations usually occur with slow groundwater flow. The evolution of the dissolution in natural rock-fluid system lasts for years [Groves and Howard, 1994; Dreybrodt, 1996; Johnson, 2008; Kaufmann and Romanov, 2008]. In industrial applications such as oil reservoir acid stimulation, several days of rock dissolution will significantly increase the permeability of the reservoir [Daccord, 1987; Hoefner and Fogler, 1988; Gomaa and Nasr-El-Din, 2010; Taylor and Nasr-El-Din, 2002]. In the following sections, common rock-fluid systems are used as examples to illustrate the effect of the reactive transport processes.

2.3.1 Karst

Karst is characterized by the predominance of rock dissolution over mechanical erosion, and is typical of present temperate (cold and warm) and tropical environments [Ford and Williams, 2013]. In karst terrains, surface and subsurface geomorphology and hydrology are largely governed by dissolution of carbonate and/or evaporite rocks. In the most classical (common) situation, surface waters, acidified by CO_2 from the air and soil, slowly dissolve carbonate rocks while percolating downwards and flowing down-gradient in the phreatic (saturated) zone towards the discharge points, typically springs.

Gypsum karst is also very commonly known in almost all areas underlain by gypsum, and extends down to depths of at least 30 m below the land surface [Johnson, 1996]. Gypsum is about 10 to 30 times more soluble than limestone [Bögli, 2012] and it commonly has a lower mechanical strength. The dissolution of gypsum also forms caves, sinkholes, disappearing streams, and other karst features (Figure 2-13) that are typically found in limestones and dolomites.

As shown in Figure 2-13, the flow in the porous rock matrix and fractures induces dissolution of the soluble rocks. The dissolution enlarges the flow paths and changes the flow condition in these flow paths. The flow in turn changes the dissolution of the soluble rocks. The flow and dissolution form positive feedback mechanism, thus the enlarged wormholes and fractures will be further enlarged into sinkholes and caves.

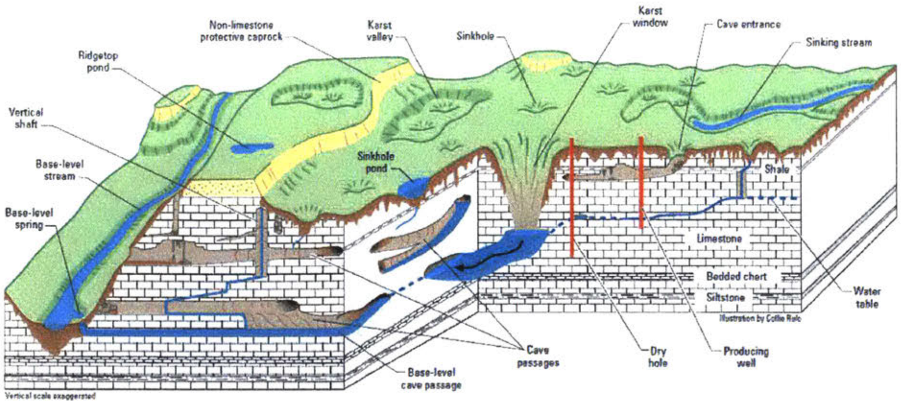

Figure 2-13: A schematic of the sinkholes and caves in a karst formation [Taylor and Greene, 2008].

2.3.2 Oil Reservoir Acid Stimulation

In the field of petroleum engineering, acid matrix stimulation has been a common method to enhance oil production [Economides and Nolte, 1989]. In acid stimulation projects, acid is pumped into wells to dissolve limestone, dolomite and calcite cement between the sediment grains of the reservoir rocks (Figure 2-14). By increasing pore sizes and creating high permeable flow paths, acid stimulation increases the permeability of the reservoir and thus oil production.

There are two types of acid treatment: matrix acid stimulation and fracture acid stimulation. In matrix acid stimulation, acid is pumped into the formation at or below the fracturing pressure. It is useful for stimulating both sandstone and carbonate reservoirs. The objective of matrix acid stimulation in carbonate matrix is to allow the acid to create wormholes near the wellbore region, reaching as far as possible into the formation. Carbonate matrix acid stimulation is also useful to treat carbonate cemented sandstones and formation damage around the well that reduces permeability or sulfide scales on the well wall [McLeod, 1984; Gidley, 1985; Nitters et al., 2000].

In fracture acid stimulation, acid is pumped above the fracturing pressure of the reservoir rock, which creates long, open channels from the wellbore penetrating deep into the formation. Fracture acid stimulation is usually carried out in carbonate reservoirs, which have lower permeability than sandstone reservoirs. It can be used to either remove formation damage or stimulate undamaged formations to produce conductive channels within the fracture such that oil and gas can migrate.

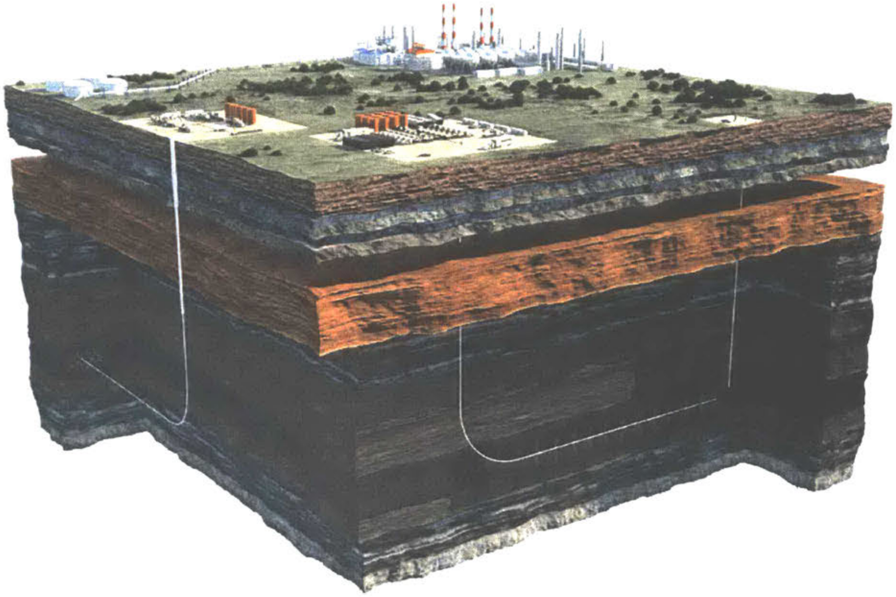

Figure 2-14: Acid stimulation operation in the oil industry.

The reactions in acid stimulation operations have been discussed in Section 2.1.1. Unlike the time scale of karst formations, acid stimulation usually occurs at a much faster rate and a much shorter time scale. Typical acid stimulation operations take about two days so that oil production can be resumed promptly.

2.3.3 Carbon Dioxide Sequestration

With the increasing concerns of global warming caused by greenhouse gases, especially carbon dioxide (CO_2), carbon dioxide sequestration has been proposed to reduce the amount of CO_2 emission in the atmosphere. CO_2 sequestration begins with capture of CO_2 at its source, such as coal fired power plants, transporting the CO_2 to a location where it can be sequestered or stored safely away from the Earth's atmosphere and oceans. Three types of CO_2 sequestration are under way: terrestrial sequestration, geologic sequestration, and mineralization (Figure 2-15). Terrestrial (or biologic) sequestration means using plants to capture CO_2 from the atmosphere and then storing it as carbon in the stems and roots of the plants as well as in the soil. Geologic sequestration is storage of CO_2 within geological formations under the Earth's surface. Oil, gas, unmineable coal and saline water reservoirs are those best suited for CO_2 sequestration [Pashin and Dodge, 2010]. An alternative to conventional geologic sequestration is carbon mineralization, where CO_2 is reacted with metal cations such as magnesium, calcium, and iron to form carbonate minerals [Romanov et al., 2015].

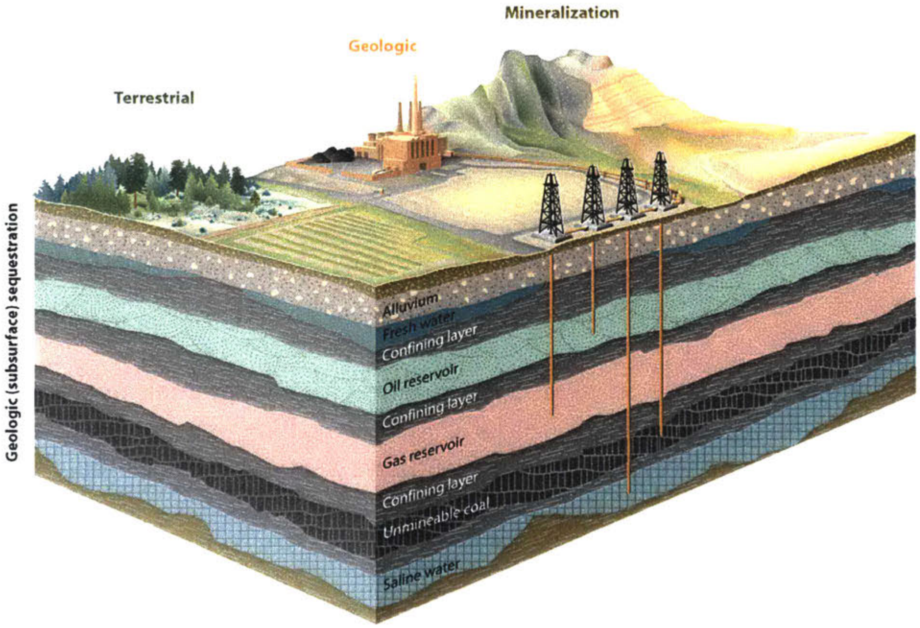

Figure 2-15: A schematic of carbon dioxide sequestration. Geological sequestration can be used to store CO_2 in underground formations such as oil, gas, and saline water reservoirs [Pashin and Dodge, 2010].

In the CO_2 storage reservoir, the injected CO_2 induces several types of reactive transport processes at different time scales (Figure 2-16). Initially, part of the injected CO_2 is trapped by capillary pressure as shown in Figure 2-16(A). The other part of the injected CO_2 is mobile and floats near the caprock of the reservoir, due to its lower density. Then, the mobile CO_2 dissolves into the pore fluid (brine), increasing the density of the pore fluid and inducing vertical convection (2-16(B)). The dissolved CO_2 reacts with carbonate minerals, for example calcite (Equation (2.2)). The dissolution changes the permeability of the rock, which in turn affects the vertical convection. The slow vertical convection and reactions could last for hundreds of years. In sum, multiple processes at different time scales are involved in the rock-CO_2-water system after CO_2 injection.

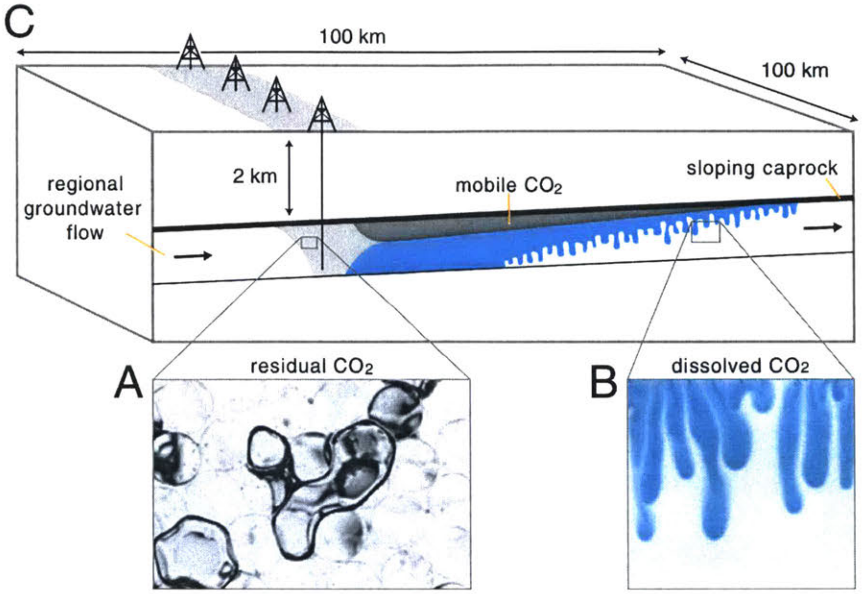

Figure 2-16: Reactive transport processes in the CO_2-water-rock system after CO_2 injection. (A) Shows blobs of gas immobilized by capillary effect. (B) The dissolved CO_2 increases the density of the fluid and induces vertical convection. (C) Reactive transport processes in the CO_2-water-rock system at field scale. [Szulczewski et al., 2012]

2.3.4 Summary on the reactive transport processes

The above three examples show the cases, in which flow and dissolution, as coupled reactive transport processes, play a major role in the evolution of the rock-fluid system. They also represent the civil-, energy- and environmental engineering settings where a good understanding of the reactive transport processes is crucial for predicting the evolution of the system and planning the engineering operations accordingly.

2.4 Experimental Study on Reactive Transport Processes

The three examples discussed in Section 2.3 have spurred many experimental studies focusing on different aspects of the reactive transport processes in various conditions.

These studies have provided fundamental understandings of the physical processes as well as propositions for the related engineering applications.

In the experimental studies, there are three general steps: initial material characterization, flow tests and final material characterization. More specifically, the material of the specimen is characterized for the properties relevant to the reactive transport processes. Flow tests are usually designed to simulate the flow in natural and engineering applications. During the flow test, the evolution of the rock-fluid system is monitored through the pressure, effluent concentration and visual change. The specimens after the flow tests are characterized and compared with their initial states to study the changes induced by the reactive transport processes. The experimental methods used to study the reactive transport processes are summarized in the following sections.

2.4.1 Material characterization

The properties of the material are often characterized using various laboratory techniques before and after the flow tests. The physical-, chemical-, transport properties, and their anisotropy and heterogeneity are often characterized using various laboratory techniques.

The bulk physical properties, such as density, specific gravity and porosity can be measured using phase relations, as shown in Figure 2-17. By measuring the masses and volumes of the sample and its solid phase, the density, specific gravity, porosity, and fluid saturation of the sample can be calculated [Germaine and Germaine, 2009].

The bulk properties describe the overall physical properties of the material. However, the detailed properties such as pore size distribution and specific surface area needs to be measured using methods such as gas absorption and mercury intrusion porosimetry (MIP).

The microscopic properties of the material can also been investigated using scanning electron microscopy (SEM), energy-dispersive X-ray spectroscopy (EDS), X-ray computed tomography (CT), thin-section analysis and atomic force microscopy (AFM). These analyses provide a microscopic view on a 2D section or a 3D volume

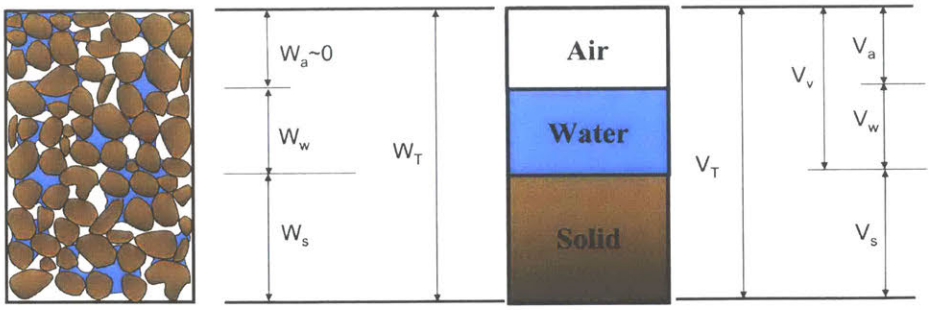

Figure 2-17: A schematic of phase relations in a porous medium. The masses and volumes of each phase can be used to calculate the density, porosity and fluid saturation.

of the material. By using EDS, the minerals and phases on a sample surface can be differentiated. Figure 2-18 shows different minerals and phases in the Opalinus shale as an example [Seiphoori et al., 2017]. X-ray CT scan provide a 3D intensity mapping of the material of interest, as shown in Figure 2-19(a). It can be used to differentiate different phases in the specimen and reconstruct the 3D geometry of the phase of interest (Figure 2-19(b)). The vuggy gypsum from Masdar city is used as an example to show how X-ray CT scanning can be used to reconstruct the clay pockets in the gypsum core. In sum, the pore structure, pore size distribution, mineral composition, and heterogeneity can be studied using these methods.

The chemical composition of the material is usually measured using X-ray powder diffraction (XRD). The atoms arrayed in a crystalline structure cause a beam of incident X-rays to diffract into many specific directions. The x-ray diffraction method records the angles and intensities of the diffracted beams. One can distinguish the type of minerals and the composition of different mineral types by analyzing the diffraction pattern. This method is used in addition to the imaging methods such as SEM and EDS for a comprehensive characterization of the mineral composition in the rock material.

The transport properties, for example permeability, can be measured before flow tests. Inert gas (argon) is often used to measure the permeability of the material since it won't react with the material. This measured permeability is used as reference and initial permeability for the flow tests. The flow tests with reactive fluid as will be

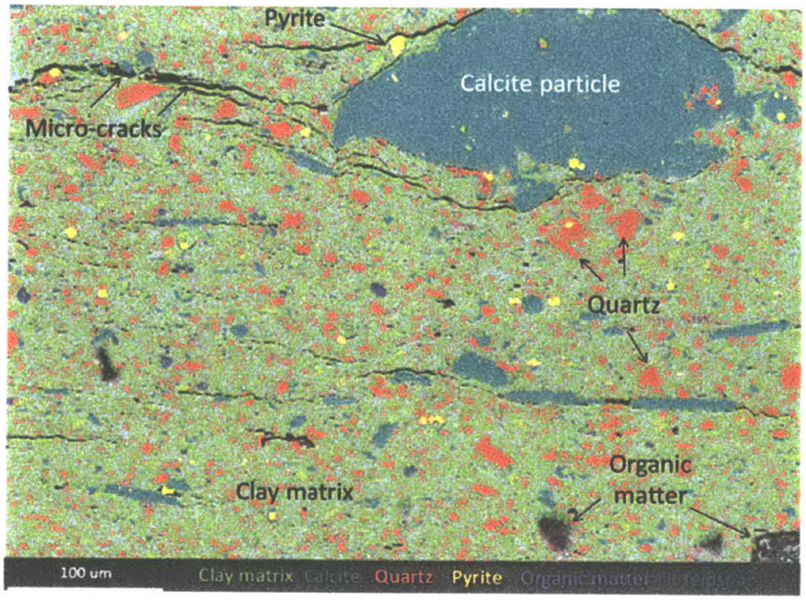

Figure 2-18: EDS map of natural Opalinus shale. The image shows on a cross section of the shale, there are multiple minerals with various structures.

discussed in the next section often changes the permeability of the material, so an initial measurement with inert gas is necessary for some studies.

2.4.2 Flow Tests

To study the reactive transport processes in the rock-fluid systems, laboratory scale flow tests are designed with various configurations to simulate different underground conditions. The common laboratory scale flow tests are discussed in this section as a basis for the experimental design in Chapter 3.

Core flood test

Core flood tests can be conducted in various ways depending on the convenience and requirements of specific applications and/or the interpretation methods available [Civan, 2015]. This can be used to measure permeability, relative permeability, saturation change, or interactions between the fluid and the rock. A flow cell with pumps, sensors, controllers and a data acquisition system work together to control and monitor the reactive transport processes in the flow cell. Figure 2-20 is a schematic of

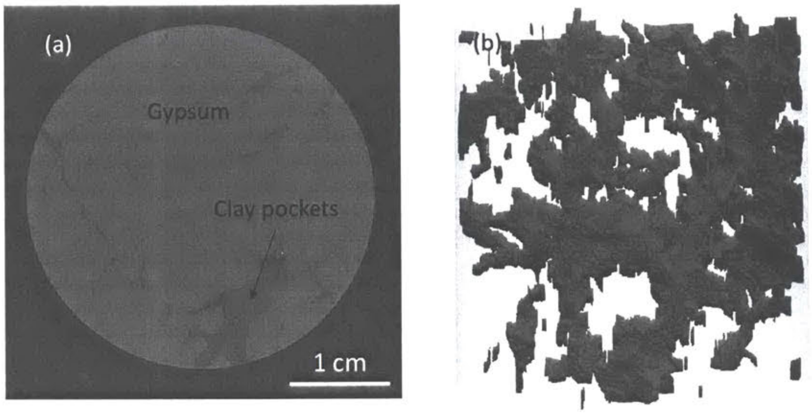

Figure 2-19: X-ray CT scanning of vuggy gypsum from Masdar City. (a) A cross-section view of the gypsum specimen based on the CT data. The gypsum is brighter, while the clay pockets are darker in the cross-section view. (b) The clay pockets (dark parts) in the specimen. The clay pockets are extracted from the 3D CT model and reconstructed in 3D.

the experimental setup of a core flood test [Izgec, 2009]. Depending on the specific requirements, the setup varies. However, most core flood test setups are similar to the one shown in Figure 2-20.

The core flood testing method can be used to study the flow in porous media and in fractures. The rock specimen (with or without fractures) is housed in the core holder, from which the axial and radial stress is applied to simulate the underground stress conditions. The injection fluid (acid, brine, CO_2 solution) is prepared and injected using a piston pump or peristaltic pump. The injection pumps either pump with a constant flow rate or a constant pressure. The specimen is back pressurized with a regulator or back pressure reservoir to elevate the pore pressure in the specimen to the designed level. The inlet pressure, outlet pressure, confining stress, axial stress and deformations can all be controlled and monitored through the computer. In some test, the effluent of the core flood test is sampled for chemical analysis, which will be discussed in Section 2.4.3.

The core flood test has been widely used in the oil industry to test the performance of injection fluids (acid, gel, and brine) in enhancing oil production. It is also used to investigate the reactive transport processes in CO_2 reservoirs. It provides good

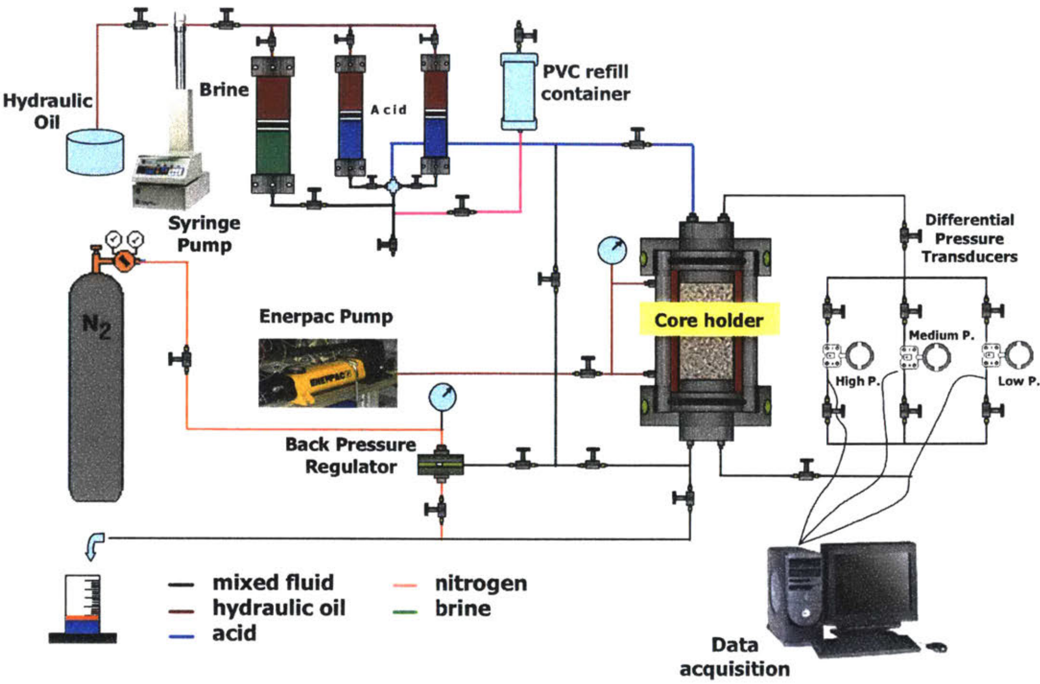

Figure 2-20: A schematic of the experimental setup for a core flood test [Izgec, 2009]. Syringe pumps are used to inject fluids of interest (acid, gel, and brine) into the core specimen (top left of the schematic). A core holder or a flow cell is used to hold the core and apply confining stress and axia stress. Pressure transducers are used to monitor the pressure difference between the inlet and outlet. An back pressure regulator or reservoir is used to controlled the specimen pressure at the outlet. The effluent of the tests are sometimes collected for chemical analysis.

flexibility in controlling stress, deformation, injection flow rate and pressures. Core flood tests are conducted on natural rock cores or analog materials. Usually, the core flood testing method cannot accommodate visual measurement due to the thick steal cell wall of the core holder and the rock specimens. X-ray CT devices have been integrated in the core flood system to provide observations on the specimen [Frash et al., 2018]. Analog materials or transparent flow cells have also been developed for visual observations on the reactive transport processes as discussed in the following section.

Test using analog materials

Since the natural rock specimens usually have inconsistent physical, chemical and transport properties, analog materials are used instead to study the reactive transport processes in underground rock-fluid systems. These analog materials simulates the behavior of natural rocks but at the same time have consistent material properties and are easier to fabricate. Some tests even facilitates visual measurement of aperture and transport that is not possible in natural rock [Detwiler, 2008; Szulzewski et al, 2013]. Such analog tests have provided fundamental understandings of the physical processes of interests.

Daccord [1987] used a gypsum-water system to study the dissolution process during acid stimulation in a calcite-HCl sytem. Gypsum specimens were prepared in disk and cylindrical shapes using Plaster of Paris. Distilled water was injected through the specimen in axial and radial directions. The dissolution patterns were studied by directly taking pictures of the patters or obtaining moldings of the dissolution pattern using low-melting-point alloy. As shown in Figure 2-21, the dissolution patterns induced by water flow in the porous gypsum specimen are often referred to as wormholes. As demonstrated by Daccord [1987] in Figure 2-21(c and d), higher flow rates result in more complex wormhole geometries.

Detwiler [2008] formed an analog fracture with a textured glass (nonreactive) and a polished, flat, transparent rock crystal (KH_2PO_4 potassium-dihydrogen-phosphate (KDP) crystal) to study the reactive transport processes in a single fracture (Figure 2-22). By using transparent material (glass and KDP), the fracture aperture can be measured using the light transmission method. KDP is soluble in water and its reaction with water is relatively simple. By flowing distilled water through the fracture, the dissolution of KDP induces the evolution of the fracture aperture, which in turn affects the flow and dissolution. The evolution of the fracture aperture can be monitored using the light transmission method. The flow and dissolution can then be calculated based on the measured fracture aperture field. This test can be used to study the reactive transport processes in rough fractures formed by one soluble surface and one insoluble surface.

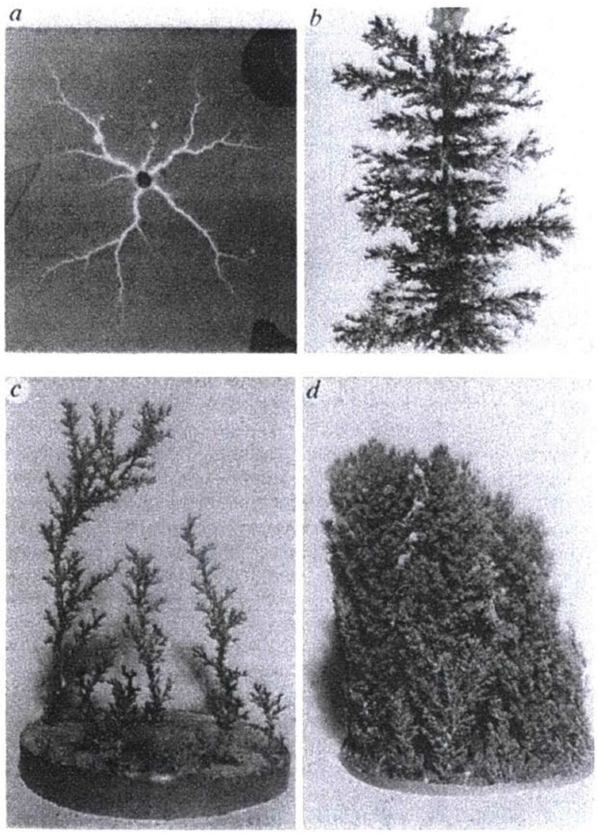

Figure 2-21: Dissolution patterns obtained for different flow conditions [Daccord 1987]. a, photograph of the 2D dissolution patterns on a gypsum disk. b, 3D moldings of the dissolution patterns induced by radial flow in a cylindrical specimen. c, d, 3D moldings of the dissolution patterns induced by axial flow.

Test using analog flow cells

Chen [1989] analyzed viscous fingering in a Hele-Shaw cell to study acidizing (dissolution) patterns in the fractures of a reservoir. When a less viscous fluid displaces a more viscous one, the boundary between the fluids is usually uneven and the less viscous fluid "fingers" into the more viscous one. This process can be used as an analog process to study the dissolution patterns (wormholes) induced by injecting acid in fractures. Figure 2-23 shows the viscous fingering caused by the injection, which is used to study acidizing in fractures by Chen [1989].

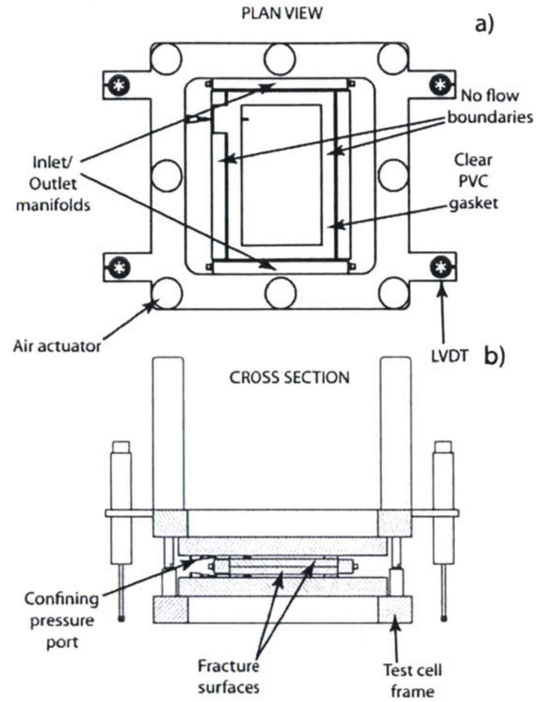

Figure 2-22: Analog fracture formed using a textured glass and KDP crystal.

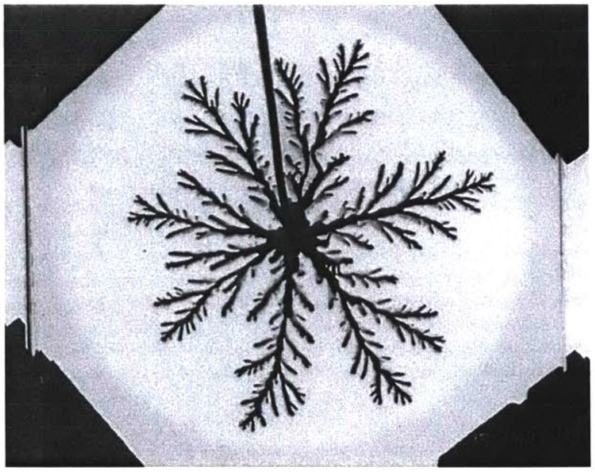

Figure 2-23: Viscous fingering resulting from injecting a less viscous fluid into a more viscous one.

Microfluidic testing

Microfluidic reactive transport experiments are also designed to study the reactive transport processes in basic flow conditions such as Poiseuille flow. Li et al. [2008]

flowed CO_2 rich water through a cylindrical pore in a single crystal of calcite, as shown in Figure 2-24. The effluent of this flow test is sampled for pH measurements. The experimental results were used to validate kinetic models for calcite dissolution.

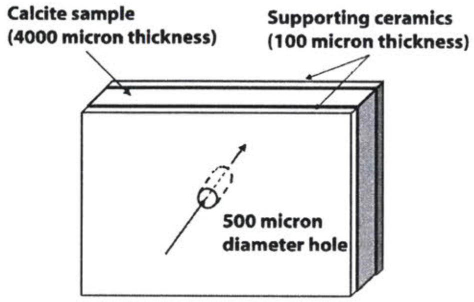

Figure 2-24: Microfluidic reactive transport experiment for dissolution kinetics model validation.

Osselin et al., [2016] designed a microfluidic device to study the onset of reactive-infiltration instability in a single fracture (Figure 2-25). Similar to the setup described by Detwiler [2008], the fracture is formed with one observing glass plate and one cast gypsum plate as the analog soluble rock. Different flow rates were used to study the effect of flow rate on the reactive-infiltration instability. A profilometer was used to measure the gypsum surface after the flow then quantify the reactive-infiltration instability.

The aforementioned experimental studies showed the various testing methods to study the reactive transport processes in the underground rock-fluid systems. Some methods are suitable for testing the rock specimen from the formation of interest, while others are only suitable for analog material or testing methods for visual observations. These testing methods have provided a lot of insights into the evolution of the rock-fluid system and better fundamental understanding of the physical processes.

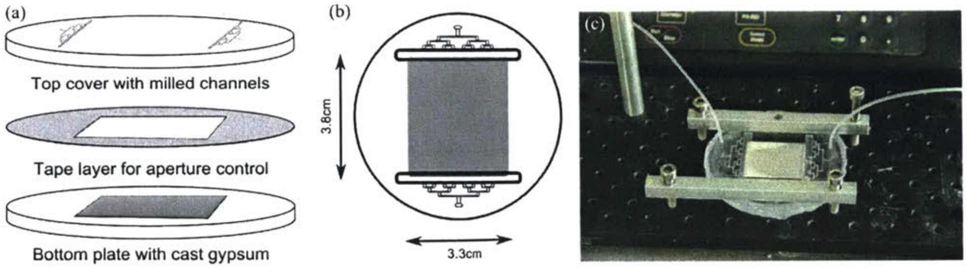

Figure 2-25: Microfluidic reactive transport experiment to study reactive-infiltration instability. (a) The analog fracture is formed with a transparent top cover with milled channels, a tape layer for aperture control and a bottom plate with cast gypsum. (b) The analog fracture assembly. (c) The microfluidic setup with an injection port and outlet port.

2.4.3 Effluent Chemistry Analysis

The chemistry of the effluent is often analyzed to study the evolution of the rock-fluid systems during the flow test. The effluent chemistry reflects the overall reactions in the rock-fluid system during the flow tests. The evolution of the effluent chemistry indicates the evolution of the reactions in the rock-fluid system. The effluent chemistry can be analyzed by sampling the effluent for chemical analysis or measuring the concentration directly in the drainage line.

Effluent sampling

If the core flood setup uses a back pressure regulator, the effluent can be directly sampled from the outlet of the back pressure regulator (Figure 2-26). If a back pressure reservoir is used, the effluent is then sampled using a sampling valve from the reservoir. This second method usually samples the mixture of effluent produced since the start of the core flood test. The effluent samples are sequenced corresponding to the time of sampling, then brought to chemical analysis.

The effluent samples are then analyzed chemically for the concentration of chemical species of interest. Usually,the effluent samples are diluted or acidized to a certain ratio so that no solute precipitates from solution during the sampling processes.

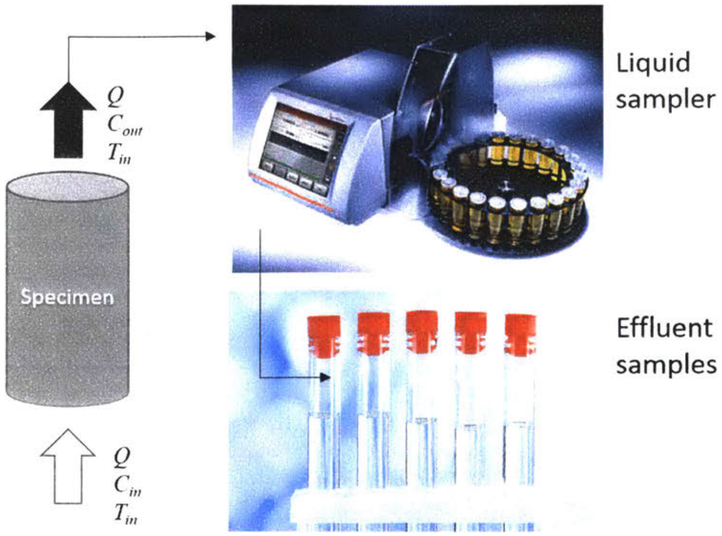

Figure 2-26: A schematic of effluent sampling. The effluent from the specimen is collected by a liquid sampler then filled in the tubes for chemical analysis.

Inductively coupled plasma-mass spectroscopy (ICP-MS), ion chromatograph (IC) analysis, ion-specific electrode analysis, or pH probes can be used to measure the concentrations of the chemical species of interest in the effluent samples [Noiriel et al., 2005, 2009; Mohamed et al., 2013; Smith et al., 2013, 2014, 2017; Al-Khulaifi et al., 2018]. The effluent concentration data can then be used to study the evolution of the rock-fluid system during the flow test.

Smith et al. [2013] used core flood tests to study the dissolution of Marly dolostone in CO_2 rich brine. In their tests, the effluent was sampled from a back pressure regulator and filtered through 0.2 μm polypropylene filters before storage and analysis. The concentrations of the calcium ion, magnesium ion, inorganic carbon, and the pH of the solution are measured for the effluent chemistry analyses using ICP-MS, IC, and phosphoric acid digestion, respectively. Figure 2-27 shows the concentrations of the calcium ion, magnesium ion, total inorganic carbon and pH of the effluent concentration sampled during the core flood tests. The time axis is zeroed at the wormhole breakthrough, when the effluent concentrations have sudden changes.

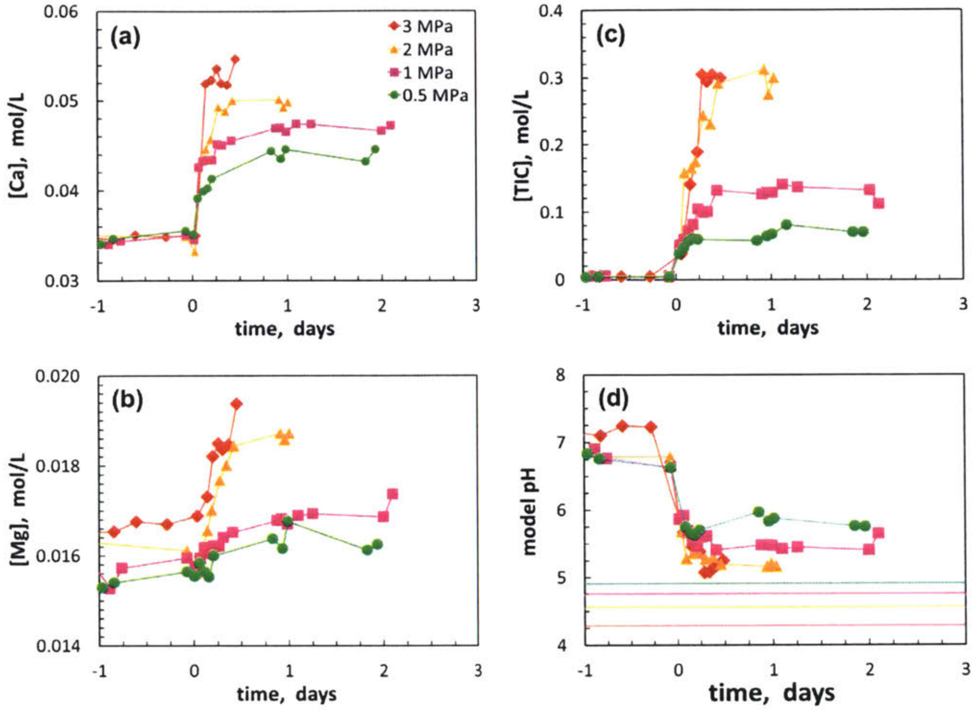

Figure 2-27: Effluent chemistry. (a) calcium; (b) magnesium; (c) total inorganic carbon, TIC; (d) modeled pH versus time for Marly dolostone samples reacted with $p\mathrm{CO}_2$ 0.5-3 MPa brines. Horizontal lines in (d) indicate the pH of corresponding input (unreacted) brine-CO_2 solutions.

Direct effluent chemistry monitoring

The effluent concentration can also be measured directly by integrating probes into the effluent drainage line or the back pressure reservoir. James and Lupton [1978] used a two-probe electric conductivity meter to monitor the electric conductivity of the effluent during a core flood test. A peristaltic pump was used to circulate fluid through the specimen. In the circulation line, a conductivity cell was integrated to measure the electric conductivity of the fluid. In the conductivity cell, a nitrogen stream was used to mix the fluid in the cell (Figure 2-28).

The experimental design by James and Lupton [1978] provides direct and continuous measurement on the electric conductivity of the fluid. Since the conductivity cell had a relatively large volume, the conductivity measured is the conductivity of the mixture of fluid. Thus, sudden changes in the effluent concentration would not be captured easily.

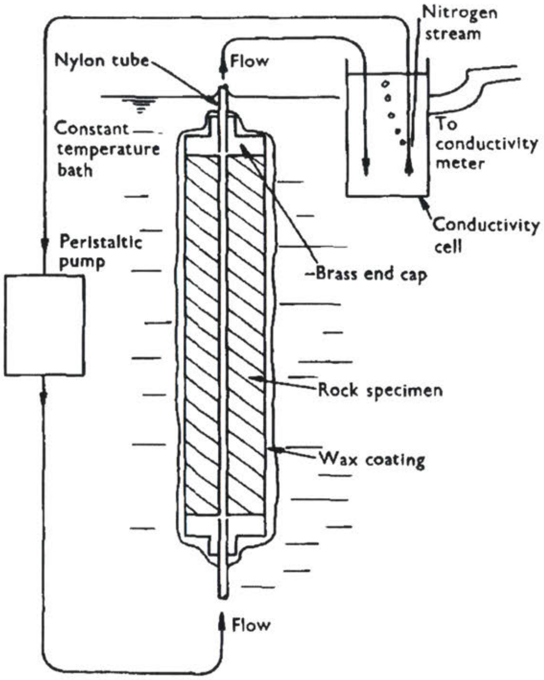

Figure 2-28: Core flood test with effluent electric conductivity measurement [James and Lupton, 1978

Ramsay [1996] studied contaminant transport in wetland deposits using core flood tests. He integrated a four-probe electric conductivity sensor, an oxidation-reduction potential sensor and a temperature sensor in the pedestal of a triaxial cell (Figure 2-29). With this pedestal, the effluent conductivity, oxidation-reduction potential and temperature could be measured immediately after the effluent exited the specimen.

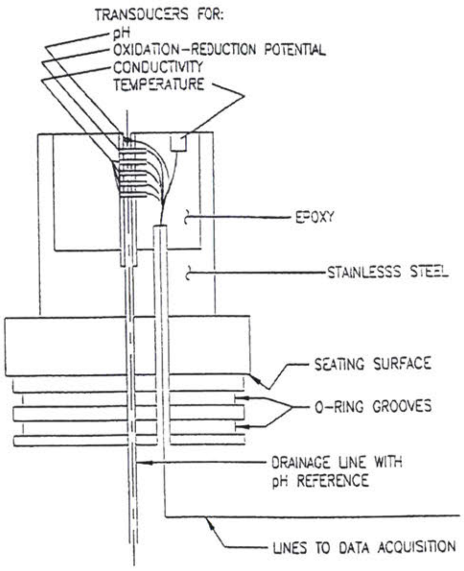

Figure 2-29: Triaxial pedestal with integrated sensors for effluent chemistry analysis [Ramsay, 1996].

The transport properties such as permeability and breakthrough curves are obtained for the wetland deposits using the pedestal. The continuous effluent concentration measurements provided good insights into the behavior of groundwater flow in wetland deposits. This experimental setup also inspired the development of the effluent chemistry monitoring system, as discussed in Section 3.2.2.

The effluent concentration is a useful parameter for studying the reactions in the rock-fluid system. It can be used to calculate the overall reaction rate of the mineral in the rock-fluid system and study the evolution of the rock-fluid system. The two methods discussed above each has their advantages and disadvantages. Effluent sampling usually provides concentrations of all the chemical species of interest, but the number of samples are limited and the accuracy is affected by the handling of the samples (prone to pressure and temperature change). The direct effluent chemistry monitoring is more convenient and provides continuous data for effluent concentration. However, only a limited number of chemical species can be measured.

2.5 Theoretical Study on Reactive Transport Processes

There have been many theoretical studies on the various underground rock-fluid systems. These theoretical studies can provide a better understanding of the behavior of the rock-fluid systems and better predict the evolution of the rock-fluid systems. In the following sections, four types of models used to study the reactive transport processes in the underground rock-fluid systems are briefly discussed.

2.5.1 Analytical Models

Analytical models are usually developed for simple geometries with homogeneous material properties. The major processes in the reactive transport processes (for example, flow and dissolution) are formulated with partial differential equations and solved analytically. The flow in the analytical reactive transport models is usually calculated with existing analytical solutions for Darcy flow, Poiseuille flow, and flow between parallel plates. The dissolution model is chosen according to the dissolution mechanisms (transport-controlled dissolution, reaction-controlled dissolution). The analytical solutions are able to predict the breakthrough curve, the evolution of permeability and the effluent concentrations.

The analytical reactive transport models for porous media are usually developed using the concept of the representative elementary volume (REV). In an REV, averaged parameters such as porosity, Darcy velocity and pore fluid concentration are used to represent its state. The governing equations are also formulated based on this REV. For example, the mass conservation equation (Equation (2.22)) describes the conservation of solute mass:

$$\frac{\partial(nC_i)}{\partial t} = \nabla \cdot (nD_i \nabla C_i) - \nabla \cdot (n\mathbf{u}C_i) - \sum_{r=1}^{N_r} \nu_{ir} R_i - \sum_{m=1}^{N_m} \nu_{im} R_m, \tag{2.22}$$

where the subscript i denotes the chemical species i; n is the porosity; C is the solute concentration; D is the molecular diffusivity (or dispersion coefficient); $\mathbf{u}$ is the Darcy velocity vector; ν_{ir} and R_i are stoichiometry coefficient and reaction rate for reactions in the solution, respectively; ν_{im} and R_m are stoichiometric coefficient and reaction rate for reactions in the mineral, respectively. Equation (2.22) describes that the change of solute i's concentration C_i depends on to the diffusion $(\nabla \cdot (nD_i \nabla C_i))$, advection $(\nabla \cdot (n\mathbf{u}C_i))$, reaction rates in the solution $(\sum_{r=1}^{N_r} \nu_{ir} R_i)$ and reaction rates with the rock minerals $(\sum_{r=1}^{N_r} \nu_{ir} R_i)$, as discussed in Section 2.1. The change of porosity caused by the reactions can be expressed as:

$$\frac{\partial n}{\partial t} = V_m R_m, \tag{2.23}$$

where V_m is the molar volume of the mineral. The change of porosity also induces the change in permeability. In this case, constitutive models for the porous media, for example the Kozeny-Carman relation [Carman, 1939], are often used to relate permeability and porosity. Analytical solutions are usually obtained with assumptions, such as constant porosity and permeability [Van Genuchten and Wierenga, 1976; Cameron and Klute, 1977].

Similarly, analytical reactive transport models can be developed by using solute mass conservation equations for flow in a single fracture or a series of equal-spaced parallel fractures imbedded in a semi-infinite porous rock matrix (Figure 2-30). The first analytical treatment of such a reactive transport process is generally attributed to Tang et al. [1981], who considered the reactive transport of contaminants in a single fracture imbedded in a semi-infinite porous rock matrix. The contaminants' absorption and radioactive decay are the two reactions considered by Tang et al. [1981]. Similarly, Sudicky and Frind, [1982] studied the contaminant transport in a series of equal-spaced parallel fractures in a semi-infinite porous rock matrix. Lowell et al. [1993][investigated silica precipitation in fractures and the resultant permeability evolution in seafloor hydrothermal upflow zones. Berkowitz and Zhou [1996] analyzed transport of sorbing chemical species in a single fracture, emphasizing interphase mass transfer between the fluid and the fracture walls. The surface reaction models that they considered include irreversible first-order kinetics, instantaneous reversible reactions, and reversible first-order kinetics. Steefel and Lichtner [1998] developed an analytical solution of silica transport in a single fracture without considering the molecular diffusion and mechanical dispersion for sake of simplicity. A recent paper [Yang, 2012] derived general analytical solutions to describe reactive silica transport in a single fracture embedded in an impervious host rock matrix, subject to both longitudinal advection and hydrodynamic dispersion.

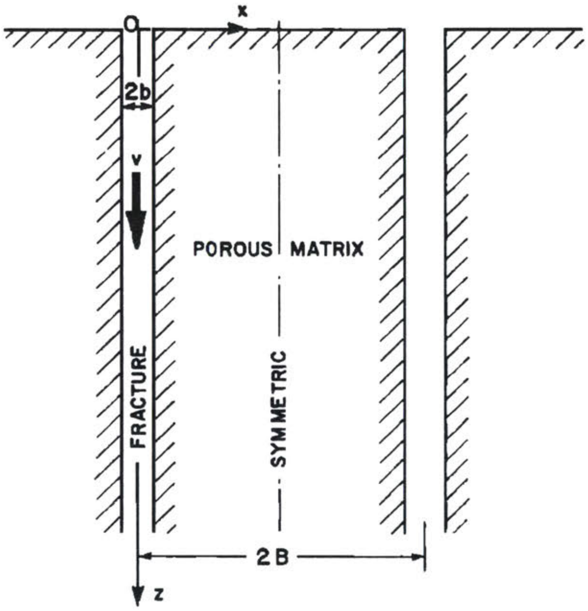

Figure 2-30: Equal-spaced parallel fractures in a semi-infinite porous rock matrix [Sudicky and Frind, 1982].

2.5.2 Continuum Numerical Models

Continuum numerical models usually try to solve the problem described by Equation (2.22). Given the versatility of computational methods, more processes, such as heat transfer and mechanical deformation, can be coupled in the numerical models to better study the reactive transport processes. The continuum numerical models for porous media are also based on the concept of REV. The pore flow, heat transfer, and reactions can all be simulated at the same time. In the review by Steefel et al., [2005], a comprehensive summary was made for single phase reactive transport modeling.

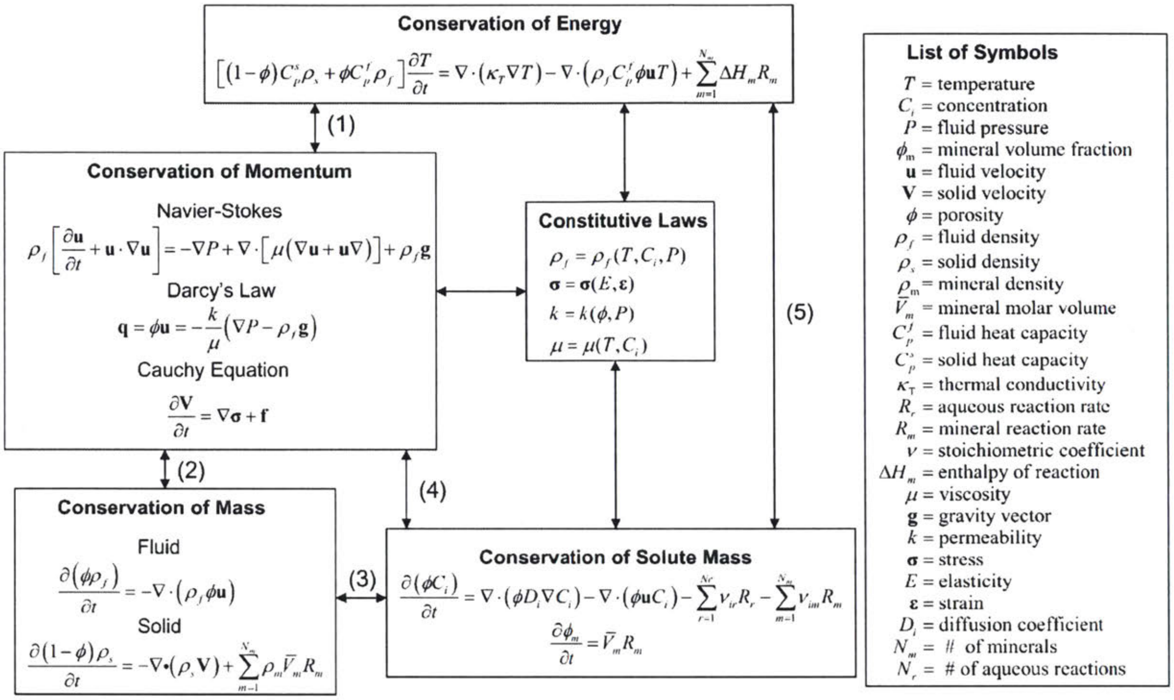

Figure 2-31: Governing equations for a single phase coupled reactive transport system, including conservation of momentum (Darcy's Law, Navier-Stokes, and Cauchy equation), the conservation of energy, the conservation of solute mass (the convection-diffusion-reaction equation), conservation of solid and fluid mass, and constitutive laws. The five arrows indicate the possible coupling between the processes.

There have been many studies using continuum reactive transport models to simulate the evolution of underground rock-fluid systems. For example, Smith et al., [2017] used the Nonisothermal Unsaturated-Saturated Flow and Transport code (NUFT) to simulate the core flood tests on carbonate-CO_2-brine system. X-ray CT scan and SEM were used to identify the minerals and their distributions in the specimen. The assumed permeability of each mineral is mapped in the continuum model to obtain the 3D permeability field of the specimen (Figure 2-32).

As described in Figure 2-31, constitutive laws, for example the porosity-permeability relationship, are used to determine the dynamic variation of permeability with porosity change due to mineral dissolution. The power law was used by Smith et al. [2017]:

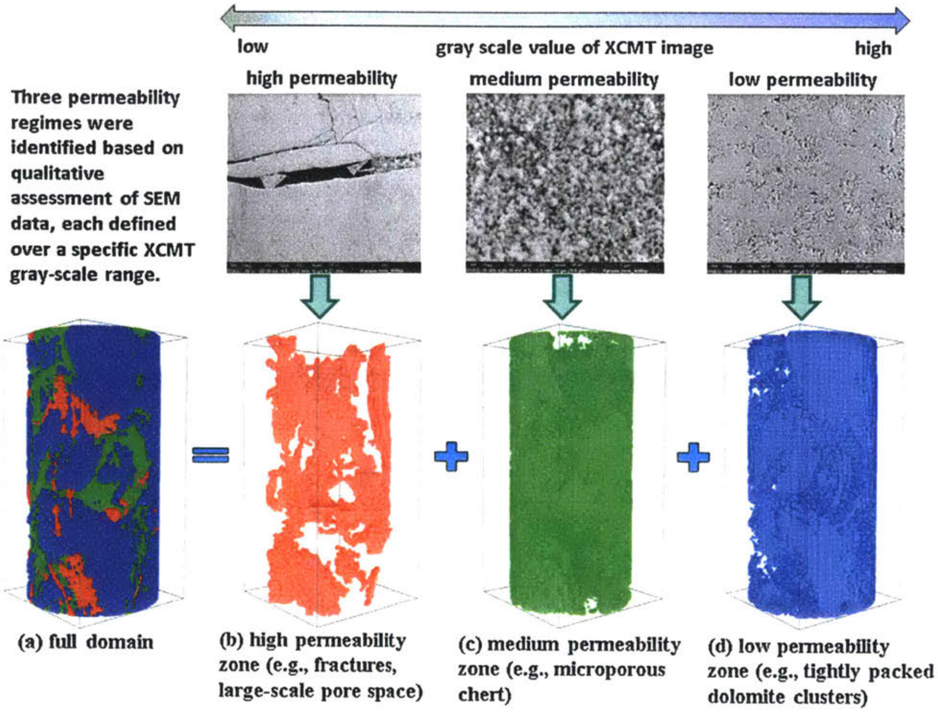

Figure 2-32: Sample partitioning procedure. (a) the full model domain as a combination of zones of three porous media types: (b) high permeability (e.g., fractures and connected macro-pores); (c) medium permeability (e.g., micro-porous chert); and (d) low permeability (e.g., tightly packed massive dolomite); identified based on CT gray-values and qualitative SEM assessment.

$$k_t = k_0 \cdot \left(\frac{n_t}{n_0} \right)^{\phi}, \tag{2.24}$$

where k_t and n_t are the permeability and porosity of the porous medium element at time t, respectively; k_0 and n_0 are the initial permeability and porosity, respectively; ϕ is the power of dependence. The dissolution patterns (wormholes), effluent chemistry, pressure difference can be predicted using this simulator. This method was used to study the qualitative correlation between the permeability contrast (ratio of high permeability to low permeability) and the stability of dissolution patterns (Figure 2-33). When the permeability contrast is low, the specimen has a relatively uniform permeability. A stable dissolution front is predicted by the model, for example Cores M0.5, M2 and A1567A, in Figure 2-33. When the permeability contrast is high, the dissolution front is not stable and wormholes form according to the simulation, for example cores A1444, A1447, V3, V1, V0.5, in Figure 2-33.

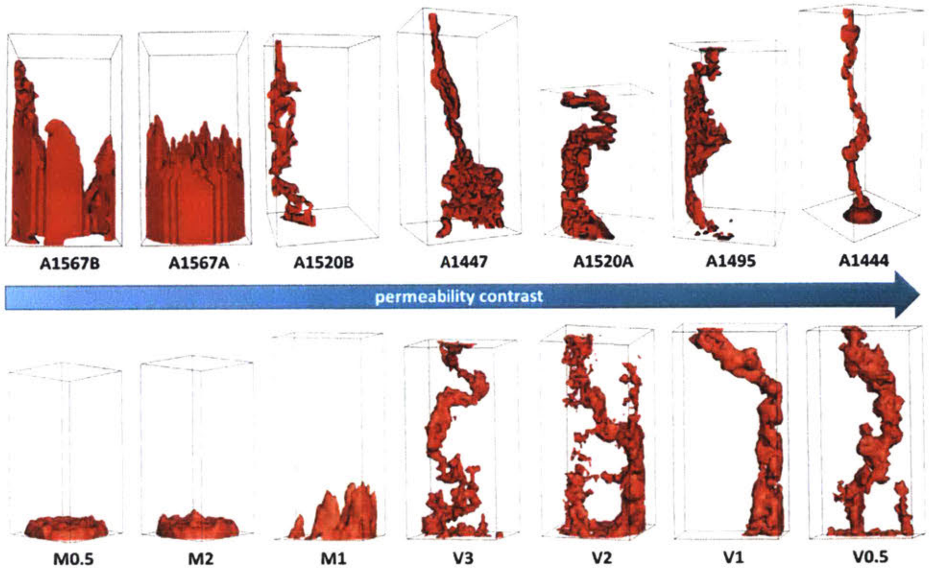

Figure 2-33: Qualitative correlation between permeability contrast (increasing towards the right) and evolution of dissolution patterns from stable to less stable [Smith et al., 2017]. A stable dissolution front tends to form in more homogeneous and permeable rocks, where the permeability contrast is small (1567A-B). As the permeability contrast increases, a sharper, more unstable dissolution front is likely to develop, as observed in the cores (A1447, A1495, and A1444). The Arbuckle samples display a relatively wide permeability contrast distribution, ranging from 2 to 5000. As a result, they exhibit a variety of dissolution features including uniform reaction front development (A1567A), fracture-dominated dissolution pathways (A1520B), and clear unstable preferential flowpath development (A1444).

As shown in the above example, continuum reactive transport models, in general, do not represent the microscopic reactive transport processes. Instead, constitutive laws for dissolution kinetics and porosity-permeability are used to model the reactive transport processes in the continuum. For example, when calculating the dissolution in each porous medium element, the surface area that is reactive with the pore fluid is calculated based on its constitutive relation with the porosity. These constitutive laws are usually calibrated for specific rock formations and for limited range of variance. For example, when the wormholes formed in the porous medium, a power law relation for porosity and permeability may not hold.

Similar continuum models have also been developed to simulate the reactive transport in a single fracture [Detwiler and Rajaram, 2007; Szymczak and Ladd, 2009]. In these continuum models, the local cubic law is used to simulate the flow in a fracture. The mechanical models, chemical models and thermodynamic models are used to calculate the changes in fracture geometry induced by compression, dissolution and pressure solution [Yasuhara et al., 2006]. Quasi-steady state simulation is often used to study the evolution of the rock-fluid system [Ameli et al., 2014]. In an underground reactive transport system, the timescale required for the pressure and concentration fields to reach equilibrium is much shorter than the timescale required for significant alteration of the fracture geometry. This allows one to use quasi-steady state concentration to calculate the rate of change in the porous media and update the geometry for the next step of the transport calculation (Figure 2-34). The continuum models can predict the change in the fracture geometry (aperture field) and study the effect of each process in the reactive transport processes.

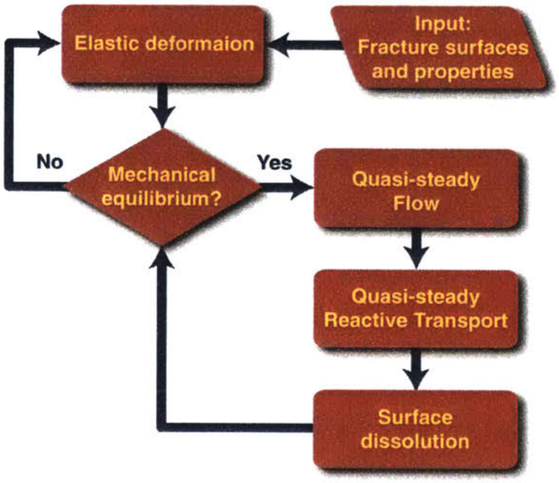

Figure 2-34: A flow chart of the computational model for coupling normal deformation and reactive flow and dissolution.

Ameli et al., [2014] simulated the fracture flow with and without mechanical deformation, as shown in Figure 2-35. The local cubic law is used to simulate the flow in the fracture. The mechanical model developed by Pyrak-Nolte and Morris, [2000] was used to predict the deformation of the fracture under compression. The reactive transport model in a single fracture by Detwiler and Rajaram, [2007] was used to calculate the alteration of fracture surfaces due to dissolution. Their study showed that the size and distribution of initial contact regions may influence the behavior of fractures subjected to coupled mechanical deformation and chemical alteration.

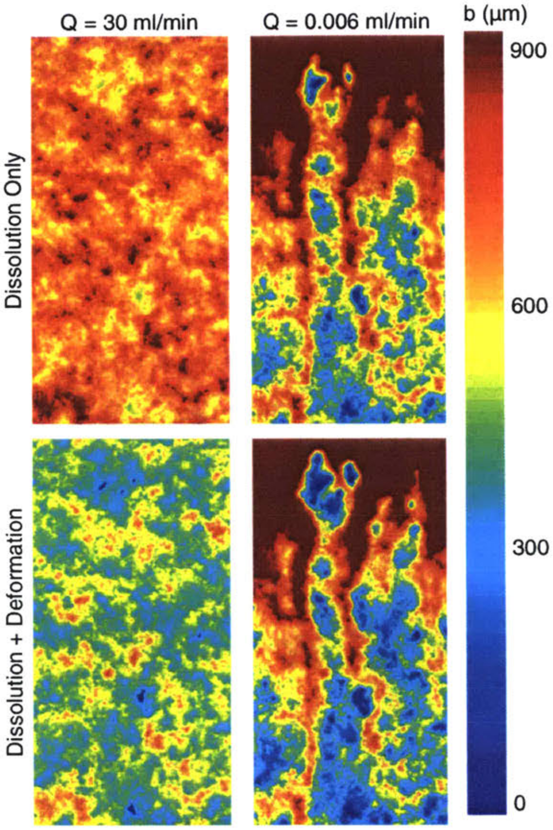

Figure 2-35: The fracture aperture field resulting from coupled dissolution and deformation [Ameli et al., 2014]. The dissolution in the fracture is more uniform with higher flow rate (30 mL/min), while the dissolution results in wormholes with lower flow rate (0.006 mL/min). When mechanical deformation is considered for the fracture, the fracture aperture is smaller.

2.5.3 Network Models

The network models discussed in this section refer to the field-scale discrete fracture network models that simulate the reactive transport processes in underground fracture networks, as well as the micro-scale pore network models that simulate the reactive transport processes in a single fracture or porous medium. In these models, the flow and transport in each fracture or pore are calculated explicitly, based on Poiseuille flow or flow between parallel plates. The reactions and transport are calculated based on analytical models such as the Graetz solution. The conservation laws for the masses of the fluid and the solute are imposed over the network. The network models are able to simulate the evolution of the network induced by reactions. Several examples of network models are discussed below to show how the underground reactive transport processes are simulated.

Network models were developed to simulate the karst formation in limestone and gypsum rocks [Sudicky and Frind, 1984; Groves and Howard, 1994a, 1994b; Howard and Groves, 1995; Gabrovšek and Dreybrodt, 2001; Birk et al., 2003; Yang, 2012]. For example, an orthogonal grid of fractures was used to simulate the flow in the fracture network [Gabrovšek and Dreybrodt, 2001]. The prominent fractures are assigned in the fracture network to simulate the major flow-conducting fractures. Due to dissolution, the fractures widen and conduct more flow, which in turn induce more dissolution. The evolution of the aquifer for 200, 1000, and 1200 years are predicted as shown in Figure 2-36.

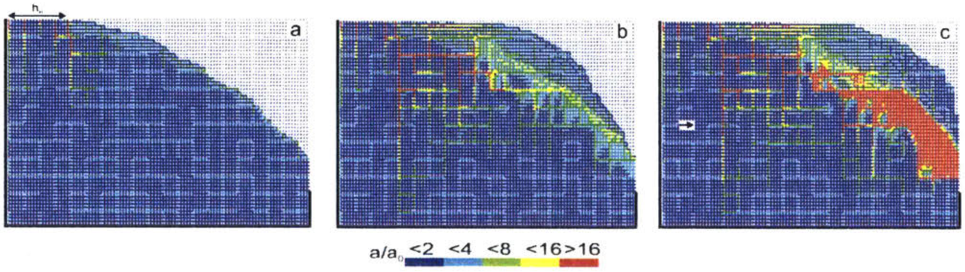

Figure 2-36: Evolution of an aquifer with dense fractures and an additional percolation network of prominent fractures with apertures of 0.02 cm (light blue). The aperture relative to initial aperture a/a_0 is color coded. The simulation shows the aperture field in the aquifer in (a) 200, (b) 1000, (c) 1200 years.

Szymczak and Ladd [2006] used a network model of fracture channel competition to model the dissolution in a single fracture. A single fracture with channels (Figure 2-37(a)) is represented as a resistor network with two types of resistors: low resistance, representing the channels, and high resistance, representing the undissolved medium ((Figure 2-37(b)). The model showed that the flow-capturing mechanism causes a fast growth of longer channels and starvation of the shorter ones, which is indeed one of the main driving factors in channel evolution.

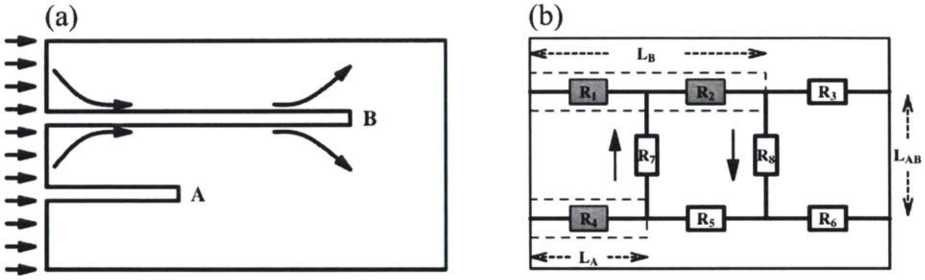

Figure 2-37: (a) Two dissolution channels in the fracture. The flow lines are converging toward a larger channel at the inlet and diverging near the tip of the conduit. (b) Resistor network corresponding to (a). The resistors with low resistance represents the channels, while the resistors with high resistance represents the undissolved fracture.

Wang et al., [2016] used a competing pore network model to simulate the wormhole formation induced by CO_2-brine flow in porous limestone specimen. The major fluid-conducting pores are conceptualized as a grid of tubes, while the diameter of the tubes are stochastically generated. The flow in each tube is calculated explicitly, while the dissolution induced geometry changes in the tube are calculated in each time step. In the next time step, the flow is calculated with the updated the tube geometries. The model qualitatively simulated the wormhole formations in the porous limestone, as shown in Figure 2-38.

The network models are usually simplified representations of the field scale fracture network and laboratory scale major fluid-conducting pore network. The network models are computationally efficient and can capture the processes leading the evolution of the rock-fluid system. However, the network models do not simulate the exact physical processes of flow and reaction. The recent development of computational methods have enabled the explicit simulation of flow and reactions at the microscopic scale, as discussed in the following section.

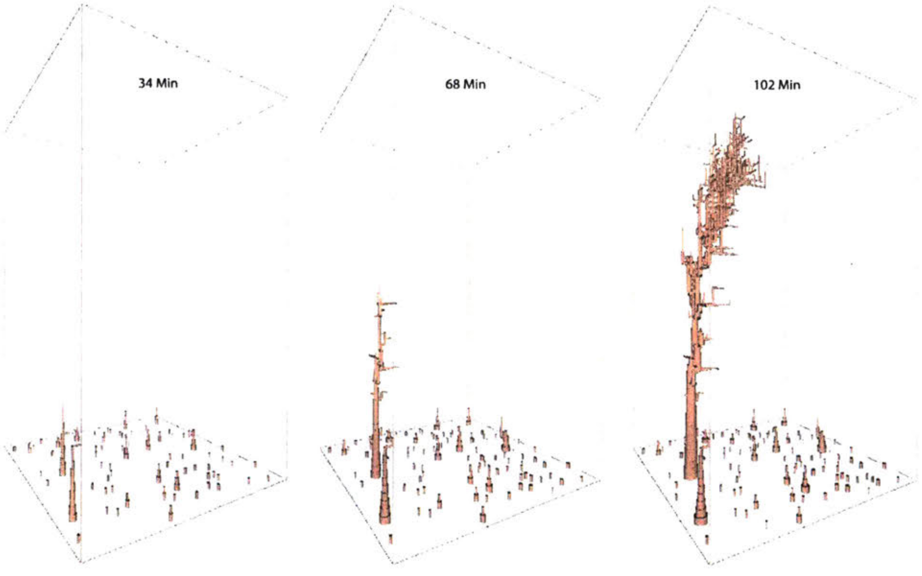

Figure 2-38: Evolution of pore network during the simulation.

2.5.4 Microscopic Models

To explicitly simulate the flow and reactions in the porous media and natural fractures, many researchers tried to resolve the microscopic flow and dissolution processes. As shown in Figure 2-7, the flow in the complex pores are simulated explicitly based on computational fluid dynamics. The advection, diffusion, and reactions are also simulated based on the flow field.

Guo et al., [2016] studied the gypsum cavity evolution by looking into the evolution of a simplified 2D solid-fluid interface at pore-scale (Figure 2-39(a)). Initially, the laminar flow over a recessed gypsum cavity dissolves the gypsum. The steady state velocity profile and concentration profile are calculated as shown in Figure 2-39(b). The dissolution is transport-controlled, as shown with the gypsum-water interface being at thermodynamic equilibrium. The calcium and sulfate ions diffuse from the interface to the stream of flow. The dissolution changed the solid-fluid interface, which in turn changed the flow field (Figure 2-39(c)). Due to the flow and dissolution the gypsum dissolves more near the upstream and less near the downstream. The geometry of the gypsum also changed the flow velocity field and concentration. This microscopic model showed how the coupled flow and reaction at the scale of a single pore drove the evolution of this relatively simple rock-fluid system. This study also provided insights into the larger scale models and experiments where surface roughness affects the results to a significant amount [Raines and Dewers, 1997].

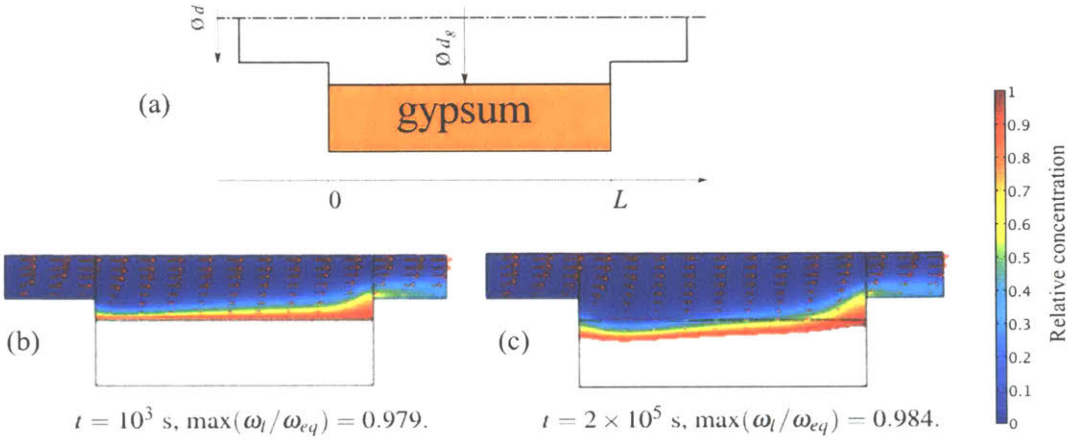

Figure 2-39: Evolution of the gypsum-water interface due to flow and dissolution. (a) A simplified 2D solid-fluid interface at pore scale. (b) The flow velocity field and concentration field near the gypsum-water interface at t=10^3s. (c) The flow velocity field and concentration field near the gypsum-water interface at t=2×10^5s.

Soulaine et al., [2017] used a micro-continuum approach (Darcy-Brinkman-Stokes formulation) to simulate the dissolution of solid minerals at the pore scale under single-phase flow conditions. Their model could explicitly simulate the flow and dissolution near a calcite crystal during acid stimulation. The flow streamline and the concentration of acid were plotted in Figure 2-40. The streamlines around the crystal shows laminar flow feature. The concentration of acid was high when the flow stream encountered the calcite crystal from the left. As acid was being consumed along the crystal surface, the concentration became lower downstream, as shown with blue on the crystal surface in Figure 2-40.

Their model was then used to study the wormhole formation in porous medium. A 2D porous model was used and the flow and reaction were simulated explicitly in this 2D porous model. The concentration and dissolution patterns in the 2D porous model resulting from different flow and reaction conditions are plotted in Figure 2-41. The five types of dissolution are summarized from their simulation. Compact dissolution in the porous medium: the acid concentration front is stable, indicating the dissolution

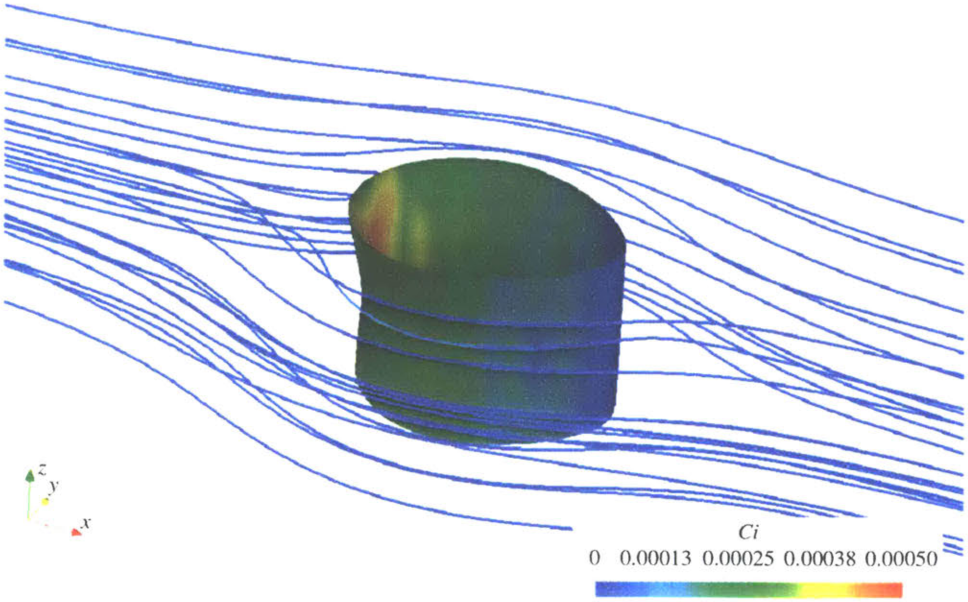

Figure 2-40: Contour of the calcite crystal based on the concentration profile 120 min after acid injection. The blue lines correspond to the streamlines. The color on the crystal surface indicates the concentration of acid. The concentration of acid was high when the flow stream encountered the calcite crystal from the left. As she acid was being consumed along the crystal surface, the concentration became lower downstream.

is more or less uniform in the porous media (Figure 2-41(b)). Conical dissolution in the porous medium: the acid concentration has one sharp front penetrating in to the porous media, resulting in one conical wormhole (Figure 2-41(c)). One dominant wormhole in the porous medium: the dissolution results in one dominant wormhole (Figure 2-41(d)). Ramified wormholes: there are more complex wormholes form due to the combination of high Péclet number and Damköhler number (Figure 2-41(e)). Uniform dissolution: the large number of wormholes in the porous medium makes the dissolution more or less uniform ((Figure 2-41(f))). This result agrees with the generally accepted conclusion that higher flow rates result in more wormholes. Soulaine et al., [2017] used the Damköhler number and the Péclet number to show the conditions under which different types of wormholes emerge (Figure 2-41(a)).

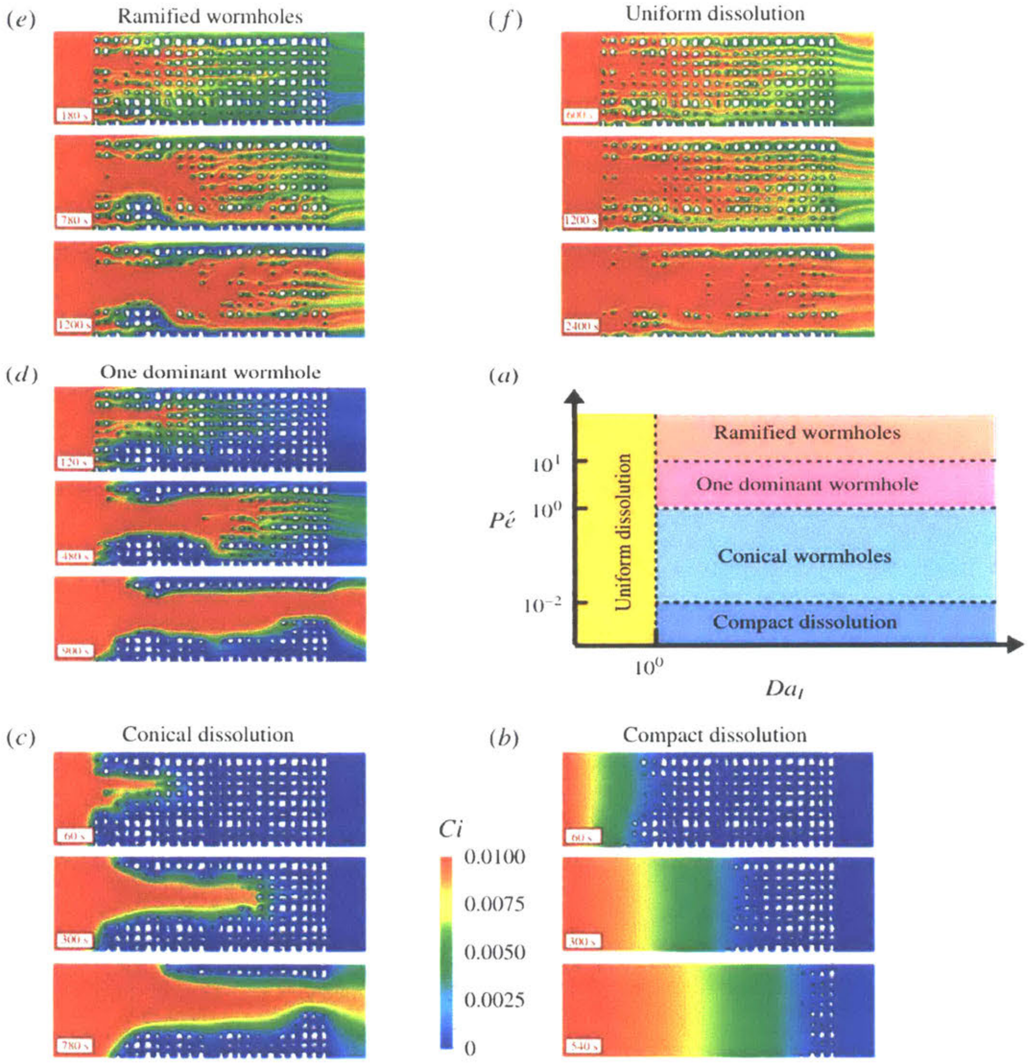

Figure 2-41: Concentration acid in the 2D porous model. (a) a summary of the types of wormholes resulting from different combination of Péclet number and Damköhler number. (b) Compact dissolution in the porous medium. (c) Conical dissolution in the porous medium. (d) One dominant wormhole in the porous medium. (e) Ramified wormholes. (f) Uniform dissolution.

The models discussed above provided a microscopic view of how reactive transport processes drove the evolution of the rock-fluid system. Some of the microscopic behaviors also correspond to laboratory scale observations such as wormhole formation. Since these microscopic models uses very fine meshes to resolve the microscopic processes, relatively high computational power is needed. The whole modeled domain is at the scale of millimeters, so proper upscaling methods are needed for field applications.

2.6 Motivations

2.6.1 Karst Geohazards in Abu Dhabi City, UAE

This research was initially sponsored and motivated by the Cooperative Agreement between the Masdar Institute of Science and Technology (Masdar Institute), Abu Dhabi, UAE and the Massachusetts Institute of Technology (MIT), Cambridge, MA, to study the karst geohazards and their potential effect on the transportation network in Abu Dhabi City.

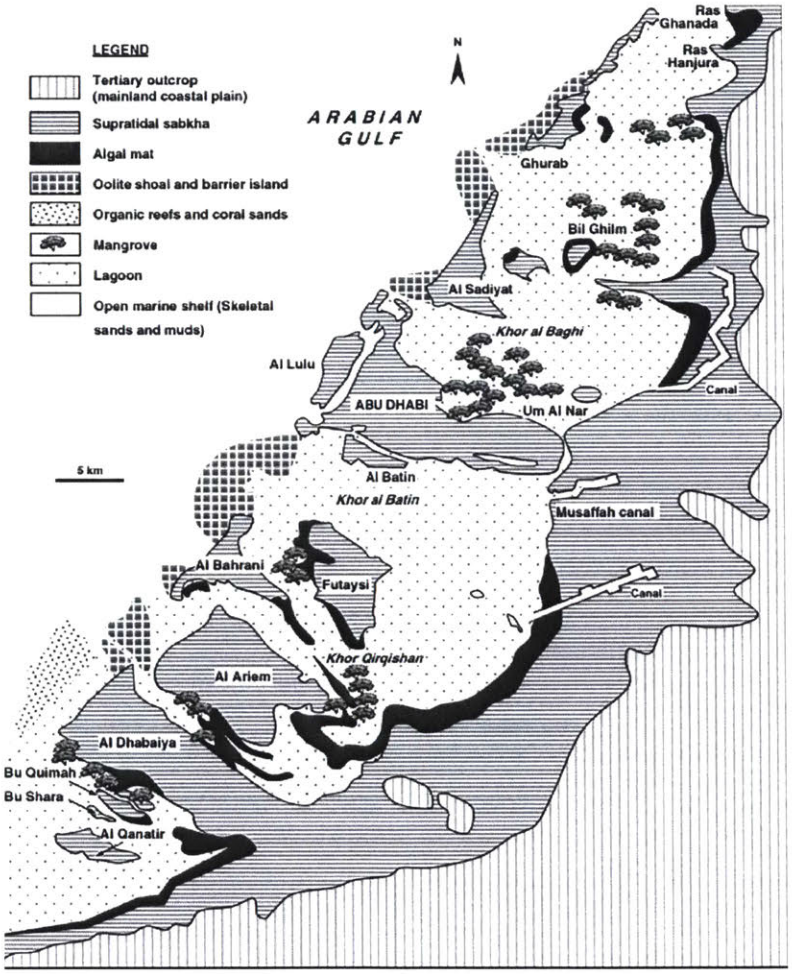

Figure 2-42: Geological map of the Coastal Areas of Abu Dhabi [Alsharhan and Kendall, 2003].

The United Arab Emirates (UAE) is located in the eastern part of the Arabian

Peninsula (Figure 2-42). The geology of the United Arab Emirates is greatly influenced by the deposition of marine sediments associated with numerous sea level changes during relatively recent geological time. With the exception of mountainous areas at the border with Oman, the topography of the country is relatively flat. The geology of Abu Dhabi comprises superficial deposits of marine sands and silts, and Sabkha deposits which overlay alternating beds of claystone and mudstone, calcarenite, sandstone, and gypsum [Alsharhan and Kendall, 2003].

Historical observations identify cavities associated with the presence of evaporate within the Abu Dhabi subsurface. The formation of subsurface cavities is normally induced by groundwater flow. Figure 2-43 shows an example of groundwater flow from cavities within the rock mass in Abu Dhabi [A.C.E.S., 2009]. These cavities are considered to be significant hazards for tunnel construction.

Figure 2-43: Groundwater flow from cavities [A.C.E.S., 2009].

To predict the evolution of the cavities and mitigate their potential impact on the infrastructure, a fundamental understanding of the reactive transport processes driving the evolution of the cavities, and predictive models to simulate the evolution of the cavities are needed.

2.6.2 Motivations for experimental research

Flow tests (Section 2.4.2) have been used to experimentally investigate the evolution of the rock-fluid system [James and Lupton, 1978; Daccord, 1987; Daccord and Lenormand, 1987; Hoefner and Fogler, 1988; Daccord et al., 1993a,b; Wang et al., 1993; Taylor et al., 2002; Noiriel et al., 2009; Gomaa et al., 2010; El-Maghraby and Blunt, 2012; Sayed et al., 2012; Smith et al., 2013; Hao et al., 2013; Mohamed et al., 2013; Smith et al., 2014; Reynolds et al., 2014; Ghommem et al., 2015; Wang et al., 2016; Noiriel and Daval, 2017; Smith et al., 2017; Cai et al., 2018; Menke et al., 2016; Lin et al., 2016; Al-Khulaifi et al., 2018; Menke et al., 2018]. In these experiments, flow tests have been used extensively because of their versatility in controlling and monitoring the confining stress, deviatoric stress, inlet pressure, outlet pressure and deformation during the tests. As discussed in Section 2.4.3, researchers often sample and analyze the effluent of the core flood test to study the reactions in the rock-fluid system. Inductively coupled plasma-mass spectroscopy (ICP-MS), ion chromatograph (IC) analysis, ion-specific electrode analysis, and pH probe were used to measure the concentrations of the chemical species of interest in the effluent samples [Noiriel et al., 2005, 2009; Mohamed et al., 2013; Smith et al., 2013, 2014, 2017; Al-Khulaifi et al., 2018]. The overall reaction rate, the reaction kinetics and the evolution of the rock-fluid system were also estimated from the effluent chemistry analysis. As discussed in Section 2.4.1, X-ray computed tomography (CT) scans were conducted on the specimen before and after the test to study the change of pore space and the formation of the wormholes [Deng et al., 2015, 2017; Gouze et al., 2003; Noiriel et al., 2004; Noiriel, 2015].

However, the flow tests conducted so far have limitations in the effluent concentration measurement and CT analyses. During the core flood tests, only a limited number of effluent samples could be collected for analysis, providing limited discrete data for the effluent concentration. Sudden changes in the effluent concentration [Hoefner and Fogler, 1988] could not be accurately captured. In addition, the effluent samples were analyzed under ambient pressure and temperature conditions instead of the pressure and temperature conditions in the specimen. With the change of pressure and temperature, the effluent was prone to degas and precipitate solutes, which induced errors in the measurements. Also, the CT analyses have mainly focused on the statistical parameters of the pore space such as porosity, and pore size distribution. The descriptions of the wormholes so far were mostly qualitative, making it difficult to compare the the formation of wormholes resulting from different experimental parameters.

The limitations in the effluent concentration measurement and CT analyses need to be addressed for reliable effluent concentration measurements and quantitative wormhole descriptions. An effluent chemistry monitoring system (ECMS) was designed to continuously measure the effluent concentration at the outlet of the specimen (Section 3.2.2). This system eliminates the need to sample the effluent for analysis, which also eliminates the possible errors associated with this processes. 3D topological and morphological algorithms are introduced in Section 4.2.6 to provide a quantitative description on the complex wormhole geometries. The 3D algorithms use parameters such as the number of wormholes and number of branches to quantitatively compare the wormholes resulting from different flow rates in Section 4.2.6.

2.6.3 Motivations for theoretical research

For dissolution in underground cavities such as fractures and wormholes, the analytical solution for transport-controlled dissolution in a cylindrical tube (the Graetz solution by Graetz (1882)) has been used to study the evolution of underground cavities in limestone [Sudicky and Frind, 1982; Groves and Howard, 1994a,b; Howard and Groves, 1995; Palmer, 1991; Dreybrodt, 1996; Rehrl et al., 2008; Kaufmann and Romanov, 2008] and other soluble materials [Raines and Dewers, 1997]. The Graetz solution has been proven to be useful in modeling the transport-controlled dissolution in cylindrical tubes.

However, its validity domain is not necessarily well understood. According to Budek and Szymczak [2012], the non-uniform dissolution along the tube reshapes the cylindrical tube into an enlarged tapered tube. The tapered tube has larger area in contact with the fluid and induces radial flow, which no longer satisfies the assumptions of the Graetz solution. Yet, in some models, the Sherwood number for the cylindrical tube was used for the tapered tube without formal justification. A 2-D analytical model is needed to explicitly study the effect of tube enlargement and induced radial flow in a tapered tube. This analytical model will be an extension of the Graetz solution to model dissolution in more complex tubular geometries, as will be discussed in Section 5.1.2 .

For flow and dissolution in the porous rock matrix, continuum reactive transport models are common models to simulate the processes. One of the key parameters used in the continuum models is the effective surface area [Panga et al., 2005; Noiriel et al., 2009; Carroll et al., 2013; Fu et al., 2015; Cheng et al., 2016; Qiao et al., 2016; Wen and Li, 2017], which is defined as the total surface area in a unit volume of rock matrix that is reactive with the fluid in the pore space. The effective surface area was estimated experimentally using mercury intrusion porosimetry, BET-based surface area measurements, high-resolution X-ray CT scanning, 2D SEM image processing (Section 2.4.1) and numerically by fitting the continuum models to the effluent concentration data [Noiriel et al., 2009, 2016; Smith et al., 2013; Hao et al., 2013]. Models estimating the effective surface area based on the pore size distribution, the thermodynamic state of the system, and the presence of flow have also been proposed [Wen and Li, 2017; Noiriel and Daval, 2017]. These methods have gained partial success in simulating the effluent concentration of the core flood tests with certain flow rates.

However, these past studies have the following limitations: firstly, the dimensional analysis based on the initial geometry might not capture the geometrical evolution of the system due to flow and reaction [Daccord et al., 1993b]. The formation of wormholes induced flow heterogeneity, which needed to be accounted for in the dimensional analysis and continuum models. In addition, the continuum reactive transport models usually assumed a constant effective surface area. The flow conditions, for example flow rate, should be accounted for when estimating effective surface area, since the flow affects the thermodynamic equilibrium between the pore fluid and the soluble minerals. These limitations need to be addressed with careful dimensional analysis for dissolution in the wormholes and the rock matrix (Section 5.2). Also, the effective surface area need to be estimated accounting for the influence of flow conditions (Section 5.3.1).

Chapter 3

Experimental Method

Tube flow tests and core flood tests were designed to study the reactive transport processes in underground rock-fluid systems. This chapter first discusses the choice of material, gypsum. Since the material properties are related to the specimen preparation process, they are presented after specimen preparation. The experimental setup and procedures are discussed in detail for the tube flow tests and core flood test. Since the tube flow tests and core flood tests are similar, the specimen preparation and experimental setup of the two will be discussed together.

3.1 Material

3.1.1 Choice of Material

Gypsum is one of the most soluble common rocks and its dissolution is generally considered to be transport-controlled [Liu and Nancollas, 1971; Raines and Dewers, 1997]. The dissolution of gypsum forms caves, sinkholes, disappearing streams, and other karst features that are also found in limestones and dolomites. Gypsum dissolution is particularly relevant since gypsum also has very low strength and dissolution may eventually lead to failure. In addition, the dissolution kinetics of the gypsum-water system is similar to the limestone-acid system [Daccord, 1987], making it an analogous material for studying acid stimulation.

In this study, laboratory cast Plaster of Paris was used to prepare gypsum specimen because of its consistency and workability, similar to Daccord's experiments. The plaster used was molding Plaster of Paris manufactured by the U.S. Gypsum company. More than 95% of the material is calcium sulfate hemihydrate ($CaSO_4 \cdot \frac{1}{2}H_2O$), the rest are crystalline silica, limestone and dolomite. Since the material properties, such as the porosity, are related to the casting process, the specimen preparation is presented before the specific material properties.

3.1.2 Specimen Preparation

For the core flood test specimen, a PVC tube with 35.56 mm inner diameter and 89 mm length was used as a mold for the plaster cast. A mass ratio of 0.6 water to plaster was used, as used by Einstein et al., [1969], to produce good workability. The plaster and water were mixed in a mixer for two minutes, then poured into the mold and vibrated for another two minutes to achieve uniformity and reduce the air bubbles in the specimen.

After the specimen was cured in a 40°C oven for one day, the gypsum had enough strength to be unmolded. The 40°C temperature was proposed by Einstein et al., [1969], to prevent the gypsum from dehydration. The specimen was further cured at 40°C for seven days to achieve enough strength. The specimen was then cut and polished to 82.55 mm in length for the core flood test.

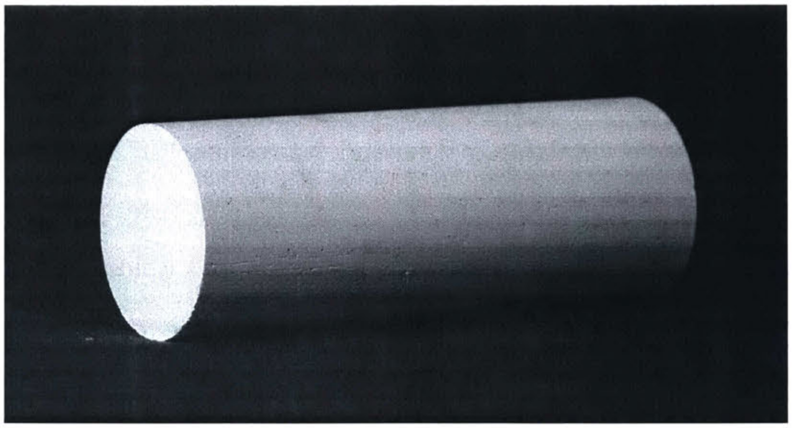

Figure 3-1: Gypsum specimen for core flood tests.

The tube flow test specimen is prepared in a similar way except for the mold. The mold consists of a PVC pipe, a rubber string and two end caps (Figure 3-2). A slot was cut in the pipe so that the gypsum paste could be poured into the mold. The two end caps each have an O-ring seal to prevent the gypsum paste from leaking at the ends of the pipe and have a small hole to hold a rubber string. The rubber string, which is the mold for the tube, has a circular cross-section with a diameter of 0.7mm. After the specimen is cured, the rubber string is removed and a straight cylindrical tube is left in the specimen (Figure 3-3).

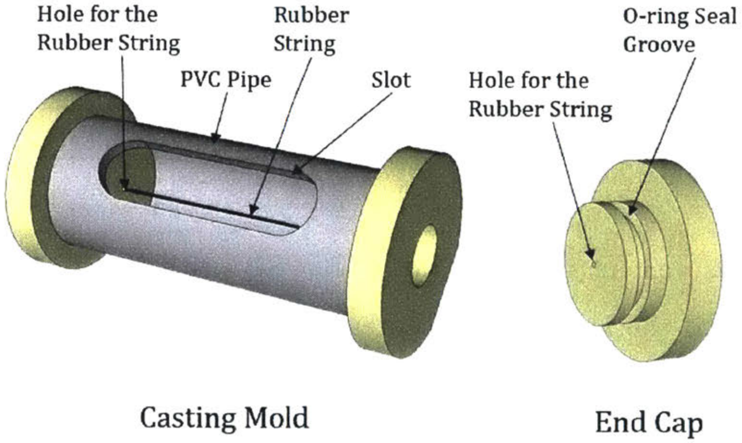

Figure 3-2: Mold for casting the gypsum specimen with a cylindrical tube.

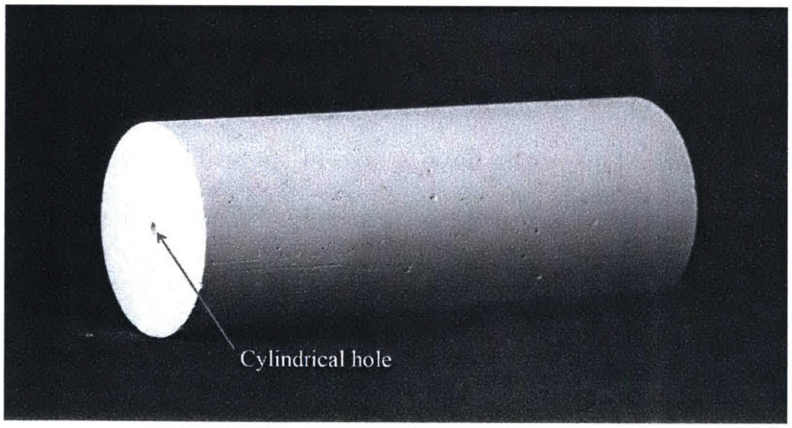

Figure 3-3: Gypsum specimen with a cylindrical tube for tube flow test.

3.1.3 Material Properties

The specimen preparation method produced specimens with consistent key material properties such as porosity and initial hydraulic conductivity. The density of the specimen was around 1.216 g/cm^3, obtained by measuring the dimensions and the mass of the specimen. Assuming a specific gravity of 2.33 for the gypsum crystals [Serafeimidis and Anagnostou,2013], the porosity calculated based on phase relations is in the range of 0.46-0.48.

Mercury intrusion porosimetry (MIP) [Giesche, 2006] and scanning electron microscopy (SEM) were also used to characterize the pore space. Figure 3-4(a) shows the incremental pore size distribution (PSD) measured using MIP. Specifically, the pore volume contributed by the pores with certain pore size (pore throat diameter) is normalized by the total MIP sample volume as the incremental porosity, as shown in Figure 3-4(a).

The MIP measurement shows a two-mode PSD, with the minor mode centered around 100 μm and the major mode centered around 2 μm. The minor mode contributes about 0.014 porosity, while the major mode contributes about 0.455, resulting in a total porosity of 0.469. The porosity measured using MIP is thus consistent with the porosity calculated based on phase relations. The 0.46-0.48 porosity is also in the porosity range of 0.40-0.60 for gypsum according to Daccord [1987]; Einstein et al., [1969].

Figure 3-4 (b) is an SEM image of an unpolished gypsum surface. The gypsum crystals show a columnar or reticulated habit and have lengths around 10 μm and diameters around 1 μm. The pores have a size of several microns, and are the major component of the porosity. The observation using SEM is consistent with the MIP result that the major mode of pore size is around 2 μm. CT scans were also used to study the pore space of the specimen before the core flood test. The CT scanning provided details on the pores larger than 50 μm, which will be discussed in Section 4.2.5.

In the core flood tests, the initial permeability of the material reflects the perme-

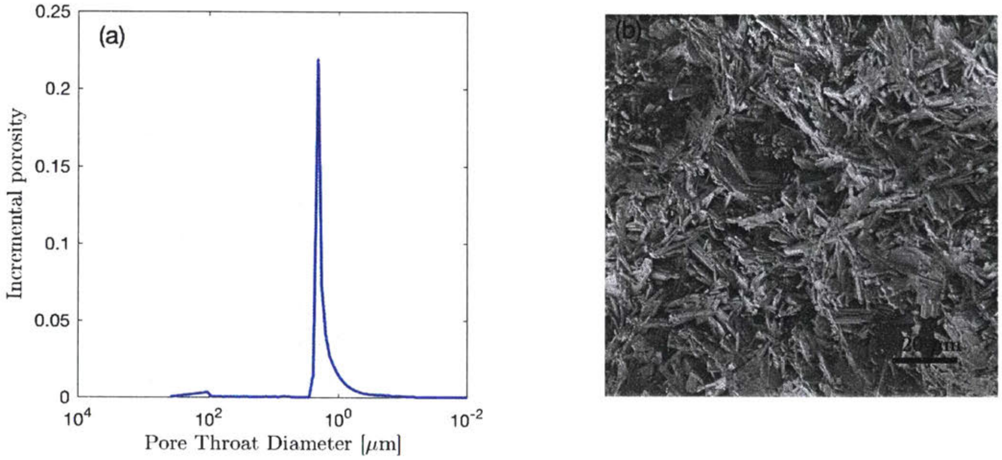

Figure 3-4: (a) Pore size distribution by mercury intrusion porosimetry. The two peaks of the incremental porosity show a two-mode pore size distribution in the specimen with one mode centered around 100 μm and the other mode centered around 2 μm. (b) SEM image of the specimen. The gypsum crystals show a columnar or reticulated habit and have lengths around 10 μm and diameters around 1 μm.

ability of the gypsum matrix that has not been affected by the dissolution. The measured permeability of the material is in the range of 21 to 25 mD, which corresponds to a hydraulic conductivity of $2.06 - 2.45 \times 10^{-7} m/s$. The gypsum-water system has a relatively high dissolution rate with the rate coefficient k_r being $7.1 \times 10^{-5} (m/s)$. The solubility of the gypsum in water C_{eq} is $2.6 g/L$ at $25°C$ temperature [Jeschke, 2001].

The gypsum-water system was often used as an analogous system for the limestone-acid system [Daccord et al., 1989]. To relate the gypsum-water system to the limestone-acid system, the acid capacity number N_{ac} is used, which is defined as the mass of solid soluble by the pore fluid per mass of the porous rock matrix [Daccord et al., 1989; Golfier et al., 2002]. The formulation Daccord et al. [1989] used can be adopted for the gypsum-water system as:

$$N_{ac} = \frac{\phi_0 C_{eq}}{(1 - \phi_0) \rho_s} \tag{3.1}$$

where ϕ_0 is the initial porosity; C_{eq} is the equilibrium concentration of gypsum in water; ρ_s is the density of the mineral (refer to Appendix A for the detailed derivation). Given the initial porosity in the range of 0.46-0.48, the equilibrium concentration $C_{eq} = 2.6g/L = 2.6 \times 10^{-3}g/cm^3$, and the density of gypsum mineral of $2.33g/cm^3$, the acid capacity number is in the order of 10^{-3}. In comparison to the acid capacity number of a limestone-HCl system, which is in the range of 10^{-3} to 10^{-1} according to Daccord et al. [1989], the gypsum-water system is analogous to the limestone-dilute acid or the high porosity limestone-acid system.

3.2 Experimental Setup

3.2.1 Computer-Controlled Triaxial System

A computer-controlled triaxial system was used to apply confining pressure on the specimen and inject distilled water through the specimen. The computer-controlled triaxial system was designed and built in the MIT Geotechnical Engineering Laboratory with progressive updates over the past two decades by Sheahan and Germaine [1992]; Andersen [1991]; Abdulhadi et al. [2011]. This system was originally designed for mechanical tests on soils and was updated for core flood tests by adding an outlet pressure transducer, upgrading the capacity of the water injection pressure-volume actuator (PVA; this is in essence a syringe pump), and integrating the effluent chemistry monitoring system (ECMS). Figure 3-5 is a diagram of this computer-controlled triaxial setup. The details of the original triaxial system were discussed in the paper by Sheahan and Germaine [1992].

As shown in Figure 3-5, the specimen was mounted between the pedestal and ECMS top cap with porous stones to spread the flow. The specimen was sealed with two membrane-sleeves between the pedestal and top cap with three O-rings each. The confining pressure was applied through the cell oil using the cell PVA. The axial stress was applied using a load frame connected to the top cap, which is not shown in Figure 3-5, for simplification.

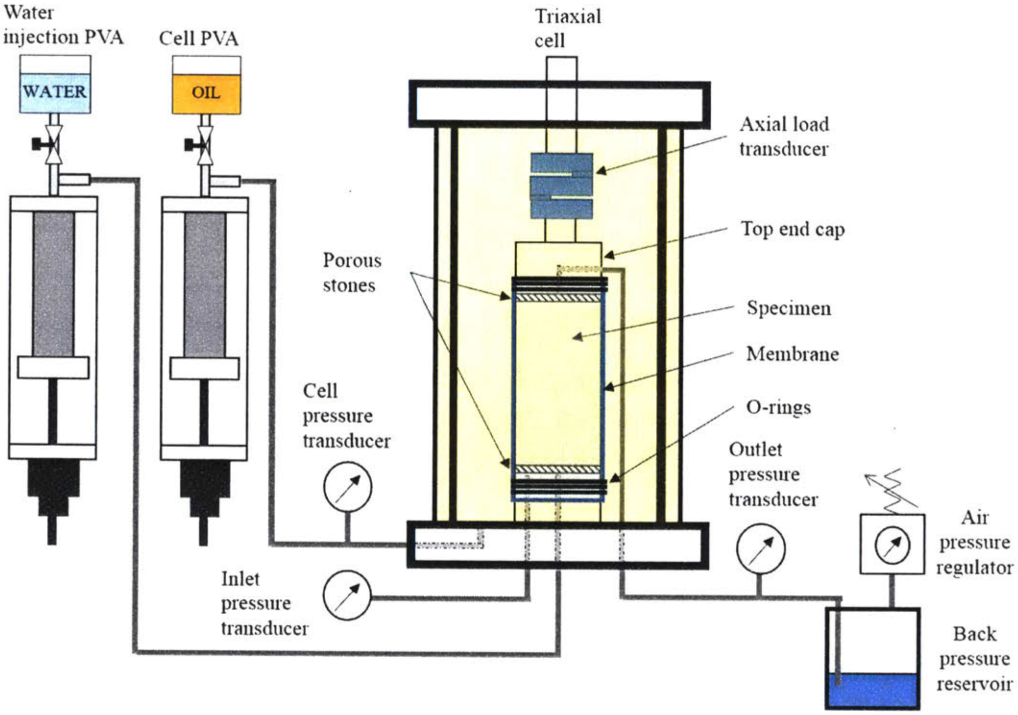

Figure 3-5: Diagram of the triaxial setup adapted for core flood tests. The parts in the setup are not drawn at the same scale.

3.2.2 Effluent Chemistry Monitoring System (ECMS)

The ECMS was designed to overcome the disadvantages of the existing methods discussed in the Introduction. It provides long-term continuous concentration and temperature measurements on the back-pressurized effluent immediately after it exits the specimen. The ECMS consists of a top cap and a circuit board. Figure 3-6(a) shows a simplified circuit diagram of the ECMS. The red rectangle represents the top cap as a part of the circuit, while the rest of the circuit is integrated into the circuit board. Figure 3-6(b) is a cross-section view of the detailed design of the top cap.

The ECMS adopted the electric conductivity measurement design proposed by Ramsay [1996] and Adams et al. [2016]. The Kelvin sensing method (four-terminal sensing method) was used to measure the electric impedance of the effluent (R_{eff}). Immediately after the effluent exits the specimen, it enters the top cap where there are four ring terminals on the drainage path. Alternating current (AC) is applied on the two outer terminals to excite the effluent and avoid ion plating. The AC voltages

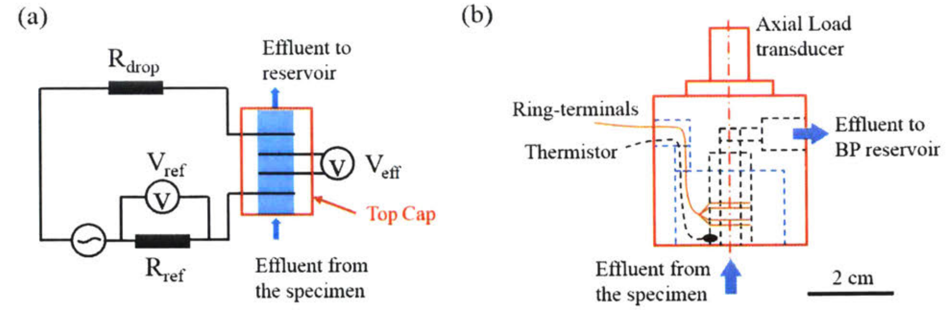

Figure 3-6: (a) Simplified circuit diagram of the effluent chemistry monitoring system (ECMS). (b) Cross-section of the top cap with integrated effluent chemistry and temperature sensor.

between the two middle ring-terminals and on the reference resistor are measured and converted to direct current (DC) voltage signals by the circuit board. These DC signals are recorded by the data acquisition system as V_{eff} and V_{ref}, respectively. The current in the effluent can be calculated as $\frac{V_{eff}}{R_{eff}}$. Therefore, the electric impedance of the effluent R_{eff} can be calculated as:

$$R_{eff} = \frac{V_{eff} \cdot R_{ref}}{V_{ref}}. \tag{3.2}$$

The circuit board is responsible for the AC voltage supply, measurement and AC-DC conversion. It consists of one signal generator circuit and two measurement circuits (Figure 3-7). These circuits are all powered by a 15V power supply. The signal generator circuit generates 7V, 10kHz AC current to excite the solution. The two measurement circuits measure the voltage on the effluent and reference voltage, and convert them to DC voltages, V_{eff} and V_{ref}, respectively.

The calibration equation was obtained for the gypsum solution by measuring the impedance of back pressurized gypsum solutions with known concentrations using the top cap and relating the measured impedance (R_{eff}) to the corresponding concentration (C_{eff}). Multiple calibration tests were conducted to obtain a reliable calibration equation as shown in Figure 3-8. The ECMS is capable of measuring gypsum concentrations from 0.01g/L to 2.6 g/L.

A thermistor was also integrated into the top cap to measure the effluent temper-

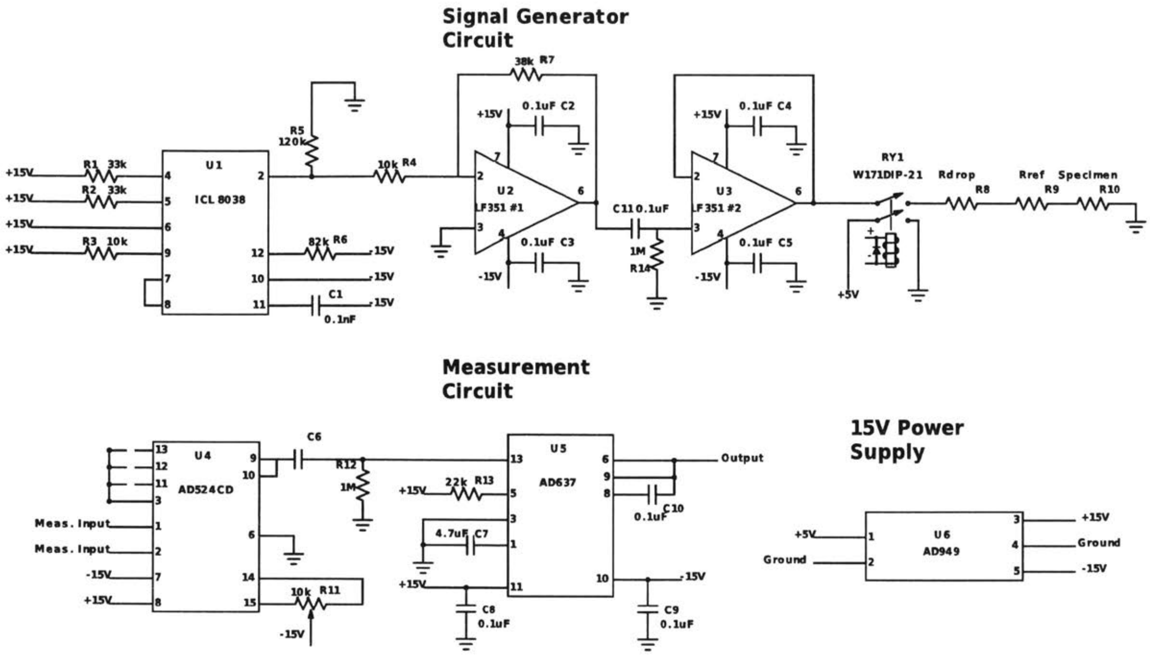

Figure 3-7: Diagram for the circuit board.

ature, as shown in Figure 3-6(b). By integrating the ECMS into the triaxial system, the effluent concentration and temperature measurement are synchronized with the measurements of the other transducers of the triaxial system (pressure transducers, displacement transducers, and load transducers).

During the core flood test, the top cap measures the concentration and temperature of the effluent in the top cap, which has a volume V_m. This volume of the effluent is continuously replaced by the newly generated effluent. The small volume ($V_m < 0.1mL$) in the top cap provides a fast effluent replacement so that the concentration and temperature are updated fast enough for continuous measurements. This design detail makes it possible to continuously measure the concentration and temperature of the back-pressurized effluent immediately after it exits the specimen.

3.2.3 X-ray CT Scan

CT scans of the specimens were taken by the MicroCT system at the Center of Nanoscale Systems at Harvard University. Figure 3-9 shows the process from scanning to obtaining the 3D binary matrix that represents the void space of the gypsum

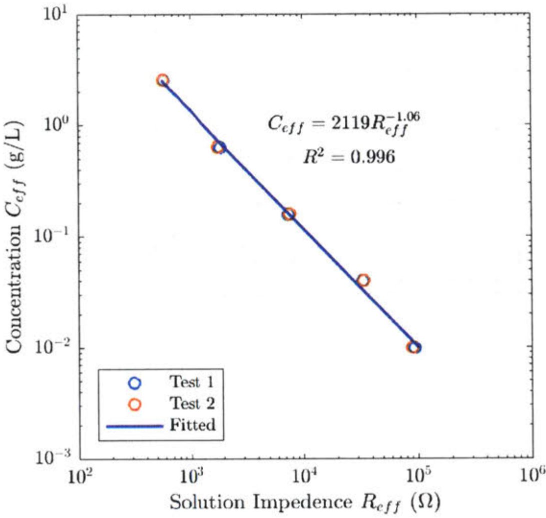

Figure 3-8: ECMS calibration test results. The calibration equation was obtained by relating the measured solution impedance to its concentration.

specimen. The X-rays were generated from a Tungsten target with a voltage of 170 kV and a current of 155 μA and were filtered using a 2.5 mm copper filter. A digital image sensor with 2000 × 2000 pixels of size 200 μm was used to record each radiograph with 16-bit precision. As shown in Figure 3-9(a), to fit the specimen image in the image sensor, 4× magnification was used, which resulted in radiographs of the specimen with a resolution of 50 μm (49.514 μm). This resolution is mainly intended for resolving the geometry of the wormholes. The exposure time for each radiograph was 1 second. The specimen manipulation stage was stopped for each radiograph exposure to reduce ring artifacts [Noiriel, 2015]. 1955 radiographic projections were taken as the specimen rotated 360° to generate enough data for reconstructing the 3D model of the specimen. Figure 3-9(b) is one of the 1955 radiographic projections.

The software Inspect-X 3D was used to reconstruct the 3D model of the specimen based on the 1955 radiographic projections. The 3D model is then exported as image stack of horizontal cross-sections of the specimen. Figure 3-9(c) shows two of the cross-sections of the specimen. Each image in the image stack is the greyscale cross section of the specimen, with higher brightness representing higher density and lower brightness representing lower density. Since the specimen material is almost pure

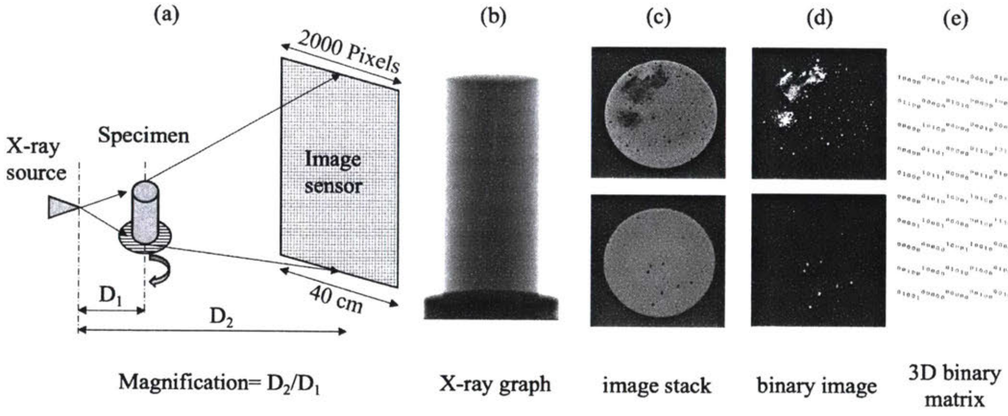

Figure 3-9: CT scan data acquisition and processing. (a) Schematic of the CT scan setup. (b) One of the 1955 radiographic projections. (c) Image stack of horizontal cross-sections of the specimen. (d) Binary image of the cross-sections with 1 (white) to represent the void space. (e) 3D binary matrix representing the specimen (a $5 \times 5 \times 10$ 3D binary matrix is used as an example).

gypsum, image segmentation for the solid phase and air phase is relatively straightforward [Deng et al., 2016]. Image binarization by the global thresholding method is used to provide fast segmentation. On each binary cross-section, 1 (white) represents solid and 0 (black) represents void. Since the void space in the specimen is of main interest for the analysis, the binary cross-sections are inverted, using 1 (white) to represent the void space. The void space outside of the specimen is also set as 0, as shown in Figure 3-9(d). The inverted image stacks were then converted to a 3D binary matrix representing the entire specimen. The location of each matrix element corresponds to the location of the voxel in the 3D model of the specimen. By using a binary matrix to represent the 3D specimen model, the amount of data can be reduced from several gigabytes to several megabytes for faster processing and analysis. The detailed topological and morphological algorithm to process the 3D binary matrix for statistical and geometrical parameters will be presented in Section 4.2.5.

3.3 Experimental Procedures

The tube flow test and core flood test both follow similar experimental processes:

- measure specimen mass and dimensions;

- install the specimen in the triaxial cell;
- apply uniform stress on the specimen;
- vacuum saturate specimen with fully-saturated gypsum solution;
- apply back pressure;
- saturate the specimen over one night for temperature equilibrium;
- flow distilled water;
- take out the specimen and dry in 40 $^{\circ}C$ oven;
- measure specimen mass and dimensions;
- X-ray CT scan.

The specimen was then vacuum saturated to ensure single-phase flow. A fully-saturated gypsum solution was used to saturate the specimen to prevent specimen dissolution during the saturation process. A back pressure of 70 kPa was applied from the back pressure reservoir (Figure 3-5) to the specimen for overnight saturation and for the subsequent core flood tests. The back pressure will force the residual air to solution during the saturation process. This back pressure further ensures single-phase flow. The temperature measured by the top cap was used to check if the system had reached temperature equilibrium before the core flood tests. During the tube flow tests and core flood tests the following parameters were recorded every 10 seconds: inlet pressure, outlet pressure, confining pressure, axial load, axial displacement, injected volume, effluent gypsum concentration and effluent temperature. After the core flood tests, the specimens were dried at 40°C for seven days before taking the mass measurements and CT scan.

3.3.1 Tube Flow Tests

Apart from the above similarities of test setup and procedures (Sections 3.1.2, 3.2), there are differences between the tube flow tests and core flood tests. The choices of uniform confining pressures were different for the tube flow tests and core flood tests. The confining pressure was applied to press the sealing membrane to the specimen to prevent the injected fluid from flowing between the specimen and the membrane. Since the cylindrical tube in the specimen has very high hydraulic conductivity, a very small pressure difference between the inlet and outlet can maintain the constant flow rate. The inlet pressure is not likely to induce flow between the specimen and the membrane. A uniform confining pressure of 200 kPa is enough.

A time-invariant flow rate condition was chosen for the tube flow tests for the following reasons. First, constant flow rate decouples the hydrodynamic processes from the reactive transport processes. The change in tube geometry induces a change in hydraulic conductivity of the tube, which changes the flow rate under constant hydraulic head condition. This would make it difficult to study the effect of tube geometry change on dissolution kinetics. Second, in industrial practice, for example acid stimulation, the injection flow rates are usually kept constant (time-invariant) for easier control. The same goes for many laboratory experimental studies [James, 1978; Smith et al., 2013, 2017; Izgec, 2009; Osselin, 2016]. In addition, in natural conditions shown in Figure 3-10 as an example, the groundwater flows through multiple ground layers, in which the gypsum layer has preexisting tubes. Since the hydraulic conductivity of a tube is much higher than the other permeable layers, the flow rate in the tube is limited by the other less permeable layers and can be assumed as time-invariant even when the tube is enlarging due to dissolution.

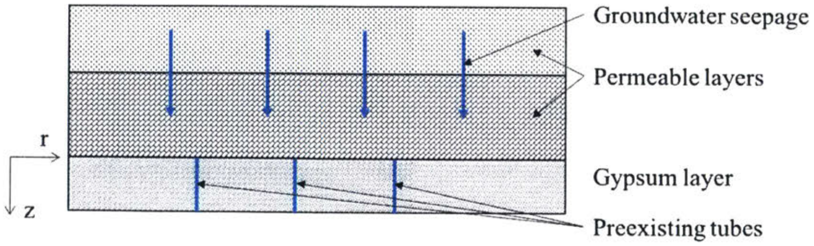

Figure 3-10: Sketch of how groundwater flows into preexisting gypsum tubes.

Four tube flow tests are conducted each with one time-invariant flow rate to study the evolution of the dissolution kinetics in the rock-fluid systems under constant flow rate. Each test used a gypsum specimen that was prepared according to the procedure described in Section 3.1.2. The flow rates used in the tube flow tests are: 2.50, 5.00, 10.00, and 20.00 $\mu L/s$. The effluent concentration was used to calculate the overall dissolution rate to track the evolution. X-ray CT scanning was used to study the geometry of the tubes after the flow tests. A fifth flow tests with 11 flow steps was used to study the relation between the effluent concentration and flow rate. The results of the tube flow tests is presented in Section 4.1.

3.3.2 Core Flood Tests

In the core flood test, the flow through the porous gypsum matrix requires a high pressure difference between the inlet and outlet. Thus a relatively high inlet pressure is required. To prevent flow between the specimen and the sealing membrane, 400 kPa confining pressure was used.

Seven core flood tests were conducted to study the matrix dissolution and wormhole formation as a function of the injection flow rate. Each test used a gypsum specimen that was prepared according to the procedure described in Section 3.1.2. Each core flood test used one constant flow rate throughout the test. The flow rates were picked based on the tests in the literature. Since the sizes of the specimens from the literature were different, the flow rates Q were normalized to the specimen cross section area as injection fluxes q, which range from 0.2 to 50 $\mu m/s$ [Hoefner and Fogler, 1988; Mohamed et al., 2013; Noiriel et al., 2016; Smith et al., 2013, 2014, 2017]. The flow rates used in our tests ranged from 5 to $40 \mu L/s$. For the 35.6 mm diameter specimen used in the core flood tests, the injection fluxes thus ranged from 5.4 to 43 $\mu m/s$, which were in the range of the tests from the literature. The seven flow rates used for the seven tests were logarithmically spaced as: 5.00, 7.07, 10.00, 14.14, 20.00, 28.28 and $40.00 \mu L/s$.

Chapter 4

Experimental Results

This chapter presents the results of the tube flow tests and core flood tests. The tube flow tests are used to study the dissolution in a controlled initial geometry (cylindrical tube) in laboratory cast gypsum. The continuous effluent concentration measurement and X-ray CT scan were used to study the overall dissolution and its effect on the tube geometry. Evolution of the rock-fluid can also be studied using the effluent concentration data. Given the relatively simple geometry, the test results can also be used as basis for the development of theoretical models (Chapter 5). Since the test results are closely related to the theoretical model, the extended Graetz solution, most of the detailed discussion of the results is presented in Chapter 5.

Core flood tests are used to study the dissolution in the rock matrix and formation of wormholes. The flow and dissolution in laboratory cast gypsum specimen was initially relatively uniform. However, minor flow heterogeneities induce dissolution heterogeneity, which in turn enhances the flow heterogeneity. This positive feedback mechanism induces wormholes in the specimen. The pressure and effluent concentration data are used to study the formation of wormholes and their effect on the permeability and dissolution of the specimen. After the wormhole breakthrough, the flow in the specimen is similar to the case of tube flow since almost all the flow is concentrated in the major wormhole. Thus, the results of the tube flow tests are also compared with the core flood tests. More detailed analyses and theoretical studies are presented in Chapter 5.

4.1 Tube Flow Tests

4.1.1 Tube Flow Tests with Time-Invariant Flow Rates

The effluent concentrations monitored by the ECMS for the four tube flow tests with time-invariant flow rates are plotted in Figure 4-1. Because the flow rates were different for the four tests, the injection durations are not comparable. The injected volume is used as the X axis instead of the injection duration so that the lengths of the curves are comparable. As shown in Figure 4-1, the effluent concentrations were initially high, which was caused by the overnight saturation (Section 3.2). The effluent concentration then soon reached steady state for the rest of the test. The tests with higher flow rates resulted in lower effluent concentration, as shown in Figure 4-1. The effluent concentration was less stable for tests with lower injection flow rates. This was caused by the flow rate fluctuations from the water injection PVA, when the flow rate was low.

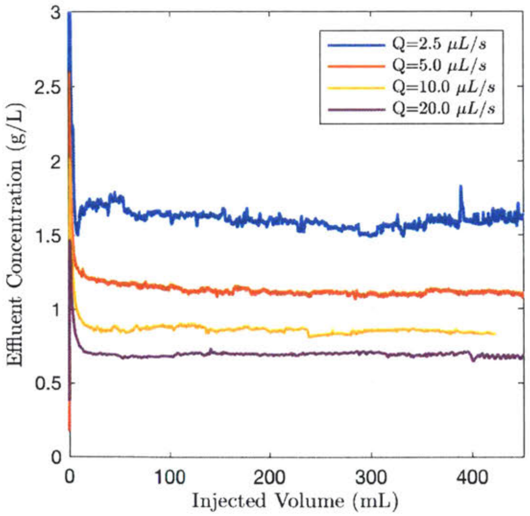

Figure 4-1: Monitored effluent concentration of the tube flow tests. Despite the geometric evolution of the tube during the flow test, the effluent concentration is time-invariant.

During the flow tests, the tubes in the specimens enlarged from 0.67 mm to 2-3 mm in diameter and formed a tapered shape (Section 4.1.3). Figure 4-1 shows that despite this evolution of the tube geometry during the flow test, the effluent concentration is time-invariant. This experimentally observed temporal behavior of the effluent concentration is consistent with the prediction of the extended Graetz solution: with time-invariant flow rate in the tube, the effluent concentration is also time-invariant despite the geometric evolution of the tube due to dissolution (see Section 5.1.5).

As discussed by Noiriel et al., [2009], the effluent concentration can be used to calculate the overall dissolution rate $R_{overall}$:

$$R_{overall} = Q \cdot (C_{eff} - C_{in}), \tag{4.1}$$

where Q is the flow rate; C_{in} is the inlet concentration. For the tube flow tests, the injected fluid is distilled water, so the inlet concentration can be treated as zero ($C_{in} = 0$). Therefore, the overall dissolution rate is $Q \cdot C_{eff}$ for the tube flow tests.

The time-invariant effluent concentration resulting from time-invariant flow rate indicates that the overall dissolution rate is also time-invariant despite the dissolution induced geometry evolution of the tube. This conclusion also sheds light on the evolution of underground cavities. As discussed in Section 3.3.1 with Figure 3-10, when groundwater flows through a soluble formation, the flow rate in the tubes can be assumed to be time-invariant since it is usually controlled by the other less permeable layers. If the dissolution of the minerals in the soluble layer is transport-controlled, the flow and dissolution conditions corresponding to Figure 3-10 are the same as the experiments. Based on the experimental study with tube flow tests, the effluent from this layer is time-invariant, thus the overall dissolution rate is time-invariant. With an constant overall dissolution rate, the mass loss of the soluble layer increases linearly with time.

4.1.2 Tube Flow Tests with Flow Rate Steps

The tube flow tests with time-invariant flow rates showed that the effluent concentration did not evolve with the tube geometry (Figure 4-1). However, there was a relation between flow rate and the effluent concentration since higher flow rates resulted in lower effluent concentrations according to the four tube flow tests discussed in Section 4.1.1. Hence, a fifth tube flow test with flow rate steps was conducted to study this relation. This test used one flow rate at each injection step with the following flow rates: 30.0, 25.0, 20.0, 15.0, 10.0, 7.0, 5.0, 2.5, 6.0, 12.0, and 17.0 L/s.

For each step, 50 mL of distilled water was injected. Given the initial volume of the tube V_{tube}:

$$V_{tube} = \pi R_{tube}^2 \cdot L_{tube} = 3.14 \times 0.067^3 \times 8.2mL = 0.127mL, \tag{4.2}$$

50 mL of distilled water replaces this volume more than 300 times. This is enough for the rock-fluid system to reach steady state, which is verified by the steady state concentrations in Figure 4-2(b). The flow rate monitored during the test is plotted in Figure 4-2(a), while the effluent concentration (C_{eff}) is plotted in in Figure 4-2(b). For each injection step, the flow rate was relatively stable and the effluent concentration reached steady state after around 20 mL of injection. As shown in Figure 4-2, each flow rate has its corresponding effluent concentration.

The flow rates and the corresponding steady state effluent concentrations were summarized for the tube flow tests with time-invariant flow rates and flow rate steps. These data will be presented in Chapter 5 for analytical model validation.

4.1.3 Tube Geometries after Flow Tests

The 3D binary matrices representing the specimens after the tube flow tests were used to study the geometry of the tube (Section 3.2.3). The 3D geometry of the tubes in the gypsum specimens are shown in Figure 4-3. The four tubes resulting from the four time-invariant flow rate tests were reconstructed. As shown in Figure 4-3, the four tubes all have enlarged inlets, forming a tapered geometry. This is caused by the non-uniform dissolution along the tube, as will be discussed in Section 5.1.2. The flow test with Q=20 μL/s also introduced additional dissolution features in the rock matrix near the tube, which resulted in the small branches near the tube, as shown

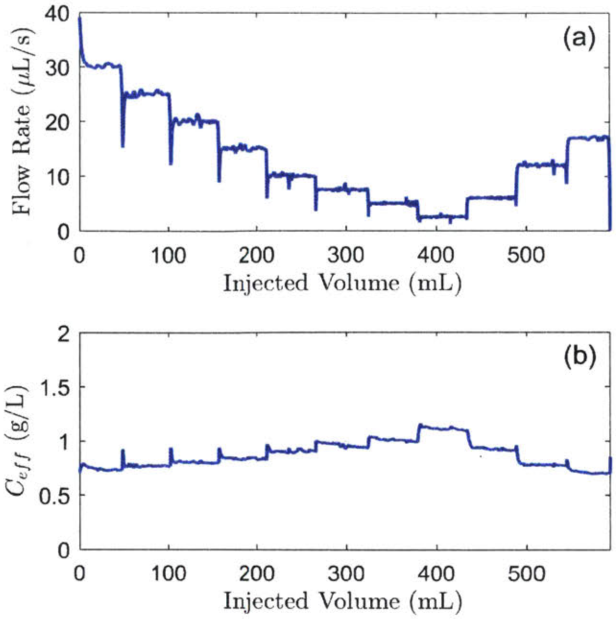

Figure 4-2: Flow rates and corresponding effluent concentrations during the tube flow test with flow rate steps.

in Figure 4-3.

Based on the 3D reconstruction of the enlarged tubes, the radius profile along the tube can be calculated by converting the cross-section area of the tube (A_{ct}) to the equivalent radius R_e:

$$R_e = \sqrt{A_{ct}/\pi}. \tag{4.3}$$

The radius profiles of the four tubes in Figure 4-3 are calculated based on Equation (4.3) and plotted in Figure 4-4. The initial radii of the tubes were in the range of 0.65-0.75 mm, while the radii of the tubes after the flow tests were in the range of 1-2 mm, as shown in Figure 4-4. The radius of the tube near the inlet is much larger than the radius of the rest of the tube due to the entrance effect (Section 5.1.2). Further analyses and comparison with theoretical models for the tube geometries are presented in Section 5.

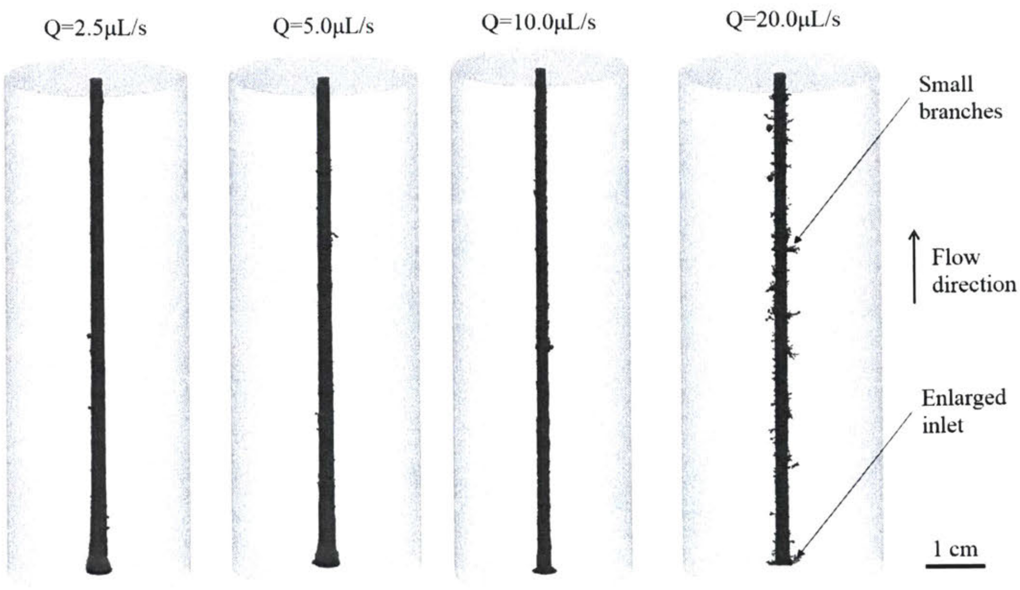

Figure 4-3: 3D reconstruction of the four enlarged tubes after the flow tests with time-invariant flow rates.

4.1.4 Summary of the tube flow tests

The study of dissolution in a cylindrical tube is an initial step towards the better understanding of the dissolution in underground rock-fluid systems. With the controlled material property, initial geometry and flow rates, the effect of dissolution on the evolution of the rock-fluid system can be studied. As shown in Figure 4-1, the effluent concentration is time-invariant after the initial transient state despite the tube enlargement from 0.65-0.75 mm to 1-2 mm. This indicates that the overall dissolution rate in the rock-fluid system is also time-invariant and that the evolution of the tube geometry does not affect the overall dissolution kinetics. The tube flow tests also showed that the dissolution in the tube is not uniform. The tube near the inlet will be enlarged more than the rest of the tube. The theoretical explanation for the evolution of effluent concentration and the tube geometry is provided in Chapter 5.

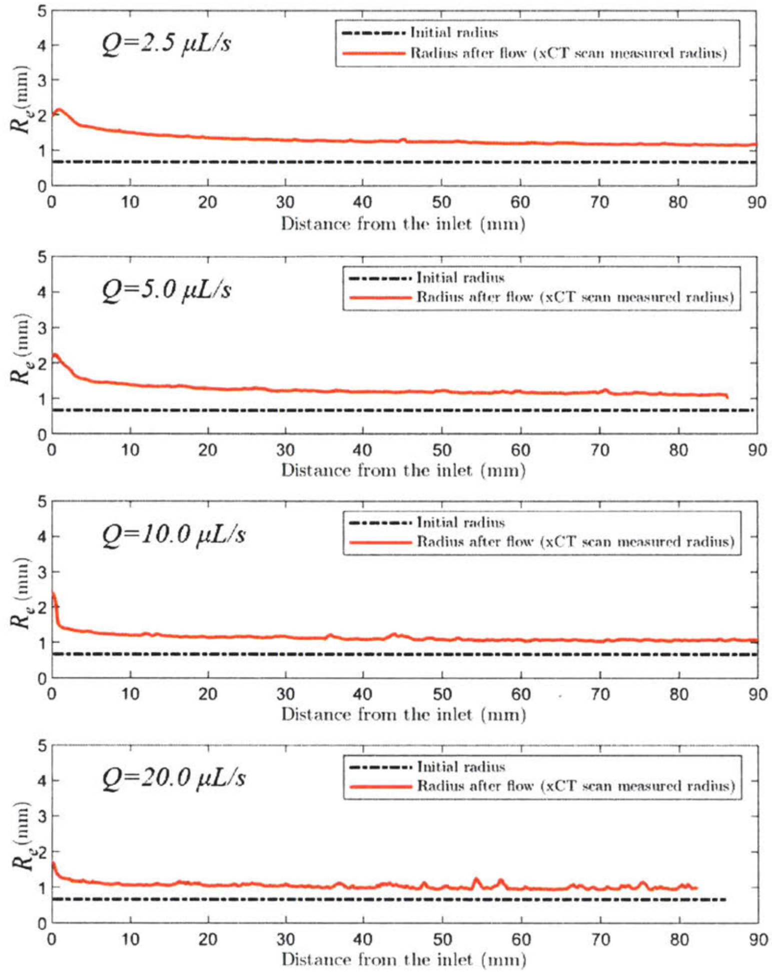

Figure 4-4: Radius profiles of the tube after the flow test. The initial tube radii and the tube radii after the tube flow tests measured using CT scan are compared.

4.2 Core Flood Tests

4.2.1 Examples of test results

As described in Section 3.3, several parameters were monitored during the experiment. The flow rate Q, the pressure difference between the inlet and outlet ΔP, and the effluent concentration C_{eff}, are plotted in Figure 4-5 for the test with a flow rate of $20\mu L/s$. The other tests, which will be summarized in Sections 4.2.2 and 4.2.3, showed similar behavior but with different values.

As shown in Figure 4-5(a), the flow rate was constant throughout the flow test. The pressure difference between the inlet and outlet ΔP is plotted relative to the

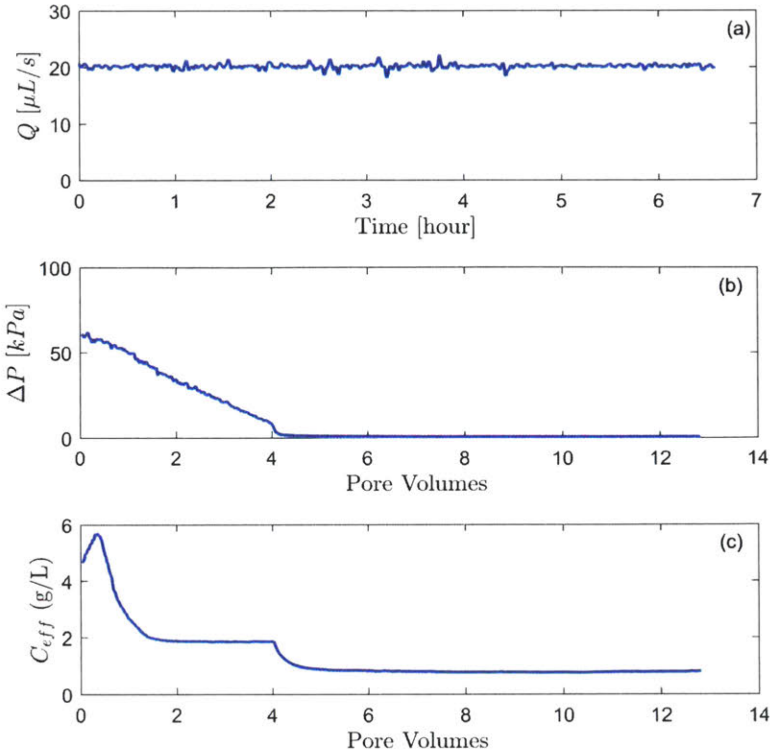

Figure 4-5: Monitored parameters during the core flood test with $Q = 20\mu L/s$. (a) Flow rate during the test; (b) Pressure difference between the inlet and outlet; (c) Effluent concentration measured by the ECMS.

injected pore volume V_p, which is defined as the injected volume V_{inject} normalized by the initial pore volume of the specimen V_{pore}.

$$V_p = \frac{V_{inject}}{V_{pore}} \tag{4.4}$$

In a core flood test where the initial pore volume V_{pore} and flow rate Q were constants, the injected pore volume (V_p) can also be represented as a dimensionless linear time coordinate, given $V_p = Q \times t/V_{pore}$. As shown in Figure 4-5(b), ΔP deceased linearly with V_p before a sudden decrease to zero at around 4 V_p. This linearly decreasing behavior of ΔP was consistent with the observations in the tests by Daccord et al. [1989]. The sudden decrease in ΔP at around 4 V_p was an indication of wormhole breakthrough since the permeability of a wormhole was much higher than that of the porous medium [Daccord et al., 1989]. More detailed analyses of the pressure data for all the tests are presented in Section 4.2.2.

The effluent concentration C_{eff} measured by the ECMS is shown in Figure 4-5(c). C_{eff} had a high value between 0 and 1 V_p, and two quasi-steady-state values between 2 to 4 and 5 to 13 pore volumes. The initial high concentration was a result of the overnight saturation when the back pressure forced the residual air in the pores into solution and increased the fluid electric conductivity. The fluid with high electric conductivity was then pushed out by the newly injected distilled water and measured by the ECMS. The two steady states indicate different dissolution mechanisms during the test, as will be discussed in more details in Section 4.2.3.

The sudden decreases of the pressure difference (ΔP) and effluent concentration C_{eff} occurred at the same time ($V_p \approx 4$), as shown in Figures 4-5(b) and (c). A similar phenomenon was also observed by Hoefner and Fogler (1988) through effluent sampling and pH measurements in their core flood tests with a limestone-acid system. This sudden decrease of the pressure difference (ΔP) corresponds to the change in the hydraulic properties of the rock-fluid system, while the simultaneous sudden decrease of C_{eff} corresponds to the change in the overall dissolution kinetics in the rock-fluid system. Figure 4-5 shows that with the continuous concentration measurements by the ECMS, the sudden changes in the dissolution kinetics of the rock-fluid system induced by wormhole breakthrough can be captured.

4.2.2 Flow and Pressure Analysis

The flow and pressure change during the core flood tests were discussed in many experimental studies [Daccord et al., 1993; Hoefner and Fogler, 1988; Wang et al., 2016]. This section compares our core flood test results with other test results in the literature. More specifically, the dependence of wormhole growth rate and breakthrough pore volume on the injection flow rate in the core flood tests is compared with those from the literature. Due to the difference in experimental setup and specimen sizes, the parameters from the literature are converted to normalized parameters in this thesis to perform proper comparisons.

Wormhole Growth Rate

Daccord et al. [1993a] proposed a conceptual model to describe the specimen with wormholes, as shown in Figure 4-6. The specimen with length L_s can be divided into the wormhole section with length L_w and the matrix section with the length L_m. Similar conceptual models were also proposed by other researchers [Tardy et al., 2007], in which the specimen was subdivided into more sections. These models do not necessarily describe the microscopic process of wormhole growth, however, they provide a reasonable interpretation for the pressure data. According to Daccord et al. [1993a], the lengths of the two sections L_w and L_m sum to the total length L_s:

$$L_s = L_w + L_m. \tag{4.5}$$

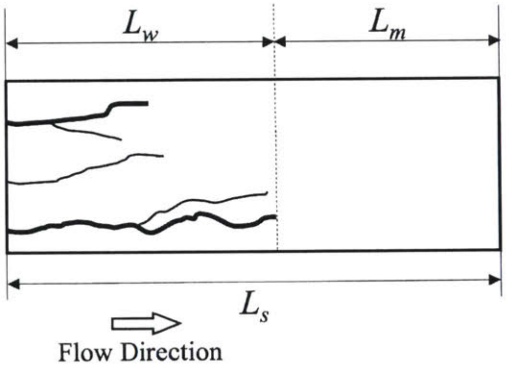

Figure 4-6: Conceptual model of wormholed specimen proposed by Daccord et al. (1993a)

Daccord et al. [1993a] assumed that the permeability of the wormhole section was infinite, and that the permeability of the matrix section was the initial permeability of the intact porous medium. With this assumption, the pressure difference ΔP between the inlet and outlet of the specimen is only associated with the matrix section. A decrease of ΔP indicates the decrease of the matrix section length L_m and the increase of L_w. The initial pressure difference ΔP_0 indicates that the wormhole section length is zero, while the pressure difference $\Delta P = 0$ indicates that the wormhole broke through.

Daccord et al. [1993a] found that the pressure difference ΔP decreased linearly with injection time (consistent with Figure 4-5(a)), which indicated the wormhole growth rate ($\frac{\partial L_w}{\partial t}$) was a constant for each core flood test. They also found that the wormhole growth rate ($v_E = \frac{\partial L_w}{\partial t}$) was proportional to the $\frac{2}{3}$ power of the injection flux $v_e \propto q^{\frac{2}{3}}$.

To compare our test results with Daccord's results, the wormhole growth rates are calculated based on the pressure data. ΔP is normalized to the initial value ΔP_0 as relative pressure difference $\Delta P_r = \Delta P/\Delta P_0$ so that 1 represents the intact specimen while 0 represents the breakthrough of wormholes. Similarly, the wormhole section length L_w and matrix section length L_m can be normalized to the specimen length as relative wormhole section length $L_{wr} = L_w/L_s$ and relative matrix section length $L_{mr} = L_m/L_s$, respectively. Given Daccord's assumption that the pressure difference ΔP is only associated with the matrix section, the relative wormhole length L_{wr} and the relative pressure difference ΔP_r have the relation: $L_{wr} = 1 - L_{mr} = 1 - \Delta P_r$. The pressure data can be used to calculate the wormhole growth rate, given that L_{wr} and ΔP_r satisfy:

$$\frac{\partial L_{wr}}{\partial V_p} = -\frac{\partial \Delta P_r}{\partial V_p}. \tag{4.6}$$

The linear decrease part of the relative pressure difference ΔP_r is fitted with a straight line. The result of the test with $Q = 20\mu L/s$ is used as an example, as shown in Figure 4-7(a). The slope of the straight line is the rate of decrease $\frac{\partial \Delta P_r}{\partial V_p}$. Given the relation in Equation (4.6), $\frac{\partial L_{wr}}{\partial V_p}$ is the positive value of the slope. $\frac{\partial L_{wr}}{\partial V_p}$ for all the tests are summarized in Figure 4-7(b). The injection flux q instead of flow rate Q is used as X coordinate. $\frac{\partial L_{wr}}{\partial V_p}$ is fitted with a power law equation, as shown in Figure 4-7(b). The power law fitting indicates that: $\frac{\partial L_{wr}}{\partial V_p} \propto q^{-0.419}$.

To calculate the wormhole growth rate v_E, the definition of V_p ($V_p = Q \times t/V_{pore}$), and L_{wr} ($L_{wr} = L_w/L_s$) are applied in the derivative $\frac{\partial L_{wr}}{\partial V_p}$:

$$v_E = \frac{\partial L_w}{\partial t} = \frac{Q \cdot L_s}{V_{pore}} \cdot \frac{\partial L_{wr}}{\partial V_p}. \tag{4.7}$$

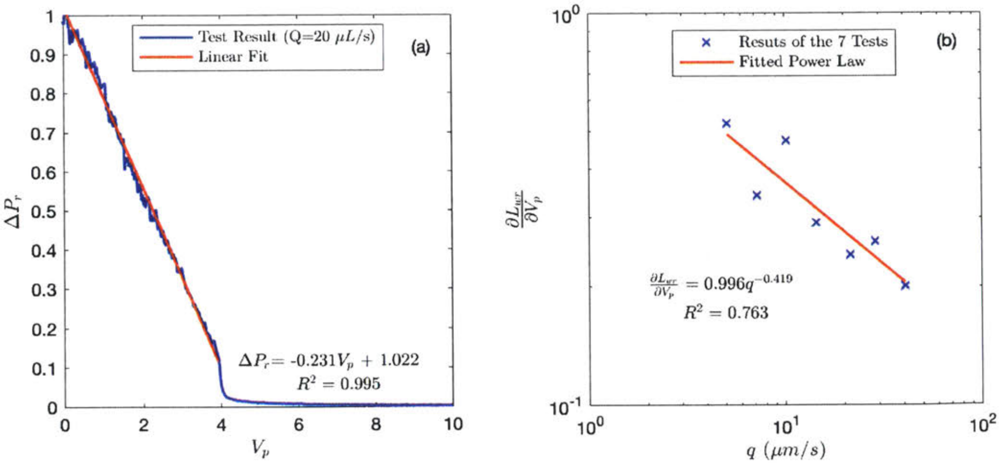

Figure 4-7: (a) Result of the test with $Q = 20\mu L/s$ is used as an example to show the linear fit of the relative pressure difference ($\Delta P_r = -0.231V_P + 1.022$); (b) $\frac{\partial L_{wr}}{\partial V_p}$ of the seven core flood tests is summarized to study the dependence of wormhole growth rate on injection flow rate.

The term $Q \cdot L_s$ in Equation (4.7) can also be expressed as $Q \cdot L_s = q \cdot A_s \cdot L_s = q \cdot V_s$, where V_s is the specimen volume. In addition, V_s/V_{pore} is the inverse of porosity: $V_s/V_{pore} = 1/n$. The wormhole growth rate v_e in Equation 4.7 can then be further simplified to:

$$v_E = \frac{1}{n} \cdot q \cdot \frac{\partial L_{wr}}{\partial V_p} \propto q \cdot q^{-0.419} \propto q^{0.581}. \tag{4.8}$$

The above discussion shows that based on the conceptual model (Figure 4-6) the wormholes grow linearly with time. This behavior is consistent with the behavior reported by Daccord et al. [1989]. In addition, the wormhole growth rates have a power dependence on the injection flux, with the power of 0.581. This is close to the value 2/3 reported by Daccord et al. [1989], despite the differences in experimental setup and methods.

Breakthrough Pore Volume

In the field of petroleum engineering, acid matrix stimulation has been a common method to increase the permeability of reservoirs and enhance oil production. The effectiveness of the acid stimulation often relies on the formation of wormholes that greatly increase the permeability of the matrix without consuming a large quantity of acid. The breakthrough pore volume V_{pbt}, which is the V_p when the wormholes break through, is often used to evaluate the effectiveness of the acid stimulation. Experimental parameters are tested and adjusted to find an optimum condition in which the V_{ptb} reaches its minimum.

Fredd and Fogler [1998] summarized the results of core flood tests with a wide range of rock-fluid systems and fitted an averaging curve to show the relation between the relative breakthrough pore volume V_{pbt}/V_{min} and the inverse Damköhler number $1/D_a$, as shown in Figure 4-8. V_{min} is the minimum breakthrough pore volume observed in the core flood tests. The Damköhler number D_a in Fredd and Fogler [1998] was defined as the ratio of dissolution rate to advection rate for an idealized cylindrical wormhole. When $1/D_a$ of the rock-fluid system is smaller than 3.4, the resulting dissolution pattern is described as "face dissolution" with no apparent wormholes or one single conical wormhole. When $1/D_a$ is larger than 3.4, the resulting dissolution pattern is described as "wormhole dissolution" with one dominant wormhole and several others. When $1/D_a$ is much larger than 3.4, the resulting dissolution pattern is described as "uniform dissolution" with many wormholes distributed uniformly in the specimen. In this section, the breakthrough pore volumes V_{pbt} as a function of the inverse Damköhler number $1/D_a$ in our core flood tests are compared with various rock-fluid system summarized by Fredd and Fogler [1998].

In our gypsum core flood tests, the idealized wormhole had a length of $85mm$. The diameter of wormholes are around $2mm$ based on CT scanning (Section 4.2.5). The diffusivity of the calcium ion, $9 \times 10^{-10} m^2/s$, was used for the diffusivity of the solute. Since the dissolution of gypsum in water is in general transport-controlled [Liu and Nancollas, 1971; Barton and Wilde, 1971; Kemper et al., 1975; Christoffersen et al., 1976; James and Lupton, 1978; Keisling et al., 1978; Navas, 1990; Ohmoto et al., 1991], the formulation for transport-controlled dissolution proposed by Fredd and Fogler [1998] was used to calculate the effective dissolution rate constant. Based on their formulation, the calculated inverse Damköhler numbers $1/D_a$ for our core flood test were in the range from 15 to 70.

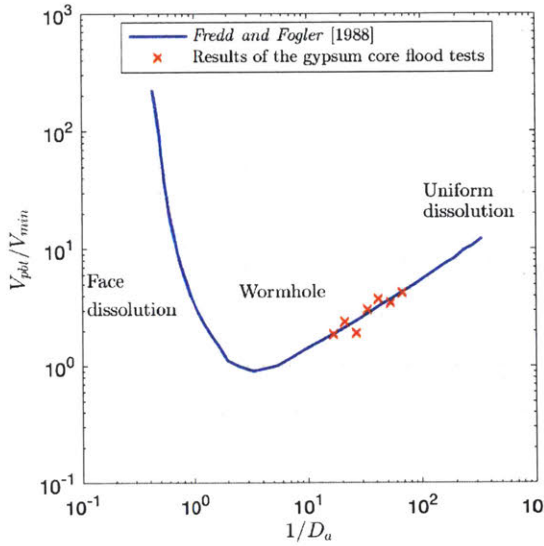

Figure 4-8: Breakthrough pore volumes as a function of inverse Damköhler number. The gypsum core flood tests show consistent behavior with the various rock-fluid systems summarized by Fredd and Fogler [1998]

Either the pressure difference data (Figure 4-5(b)) or the effluent concentration data (Figure 4-5(c)) can be used to find the breakthrough pore volume V_{pbt} in our gypsum core flood tests. Since the minimum breakthrough pore volume V_{min} was not observed in the seven tests, an assumption has to be made for V_{min} to calculate the relative breakthrough pore volume V_{pbt}/V_{min}. With the assumption $V_{min} = 1.2$, the results of the gypsum core flood tests match the summary of Fredd and Fogler [1998] very well, as shown in Figure 4-8. It should be noted that the assumption of $V_{min} = 1.2$ only affects the vertical position of the data points for the gypsum core flood tests. Even without the assumption of V_{min}, the slope of the data points would still match the slope in Fredd and Fogler [1998].

Summary of Flow and Pressure Analyses

The flow and pressure analyses above show that our core flood tests are consistent with the core flood tests in a wide range of rock-fluid systems reported in the literature [Daccord et al., 1989; Fredd and Fogler, 1998]. The wormhole growth rate of our core flood test is proportional to the 0.581 power of the injection flux (see Equation (4.8)). This is close to the 2/3 power reported by Daccord et al. [1989]. In addition, the breakthrough pore volumes of our core flood tests have a dependence on the inverse Damköhler number, which is consistent with the result summarized by Fredd and Fogler [1998] for various rock-fluid systems.

4.2.3 Effluent Concentration Analysis

The effluent concentrations monitored by the ECMS in the seven core flood tests are plotted in Figure 4-9. The X axis is the injected pore volume (V_p), which is the volume of injected distilled water normalized by the initial pore volume. Since the ECMS was only calibrated for the concentrations ranging from 0.01g/L to 2.6 g/L, the beginning part of the curve greater than 3 g/L is plotted as 3 g/L. The effluent concentration in the beginning part of the curve is high due to the dissolution of residual air in the specimen during the overnight saturation, as explained in Section 4.2.1. For the seven tests with different flow rates, the effluent concentrations have similar behavior. For each of the core flood tests, the measured effluent concentration is relatively high at the beginning of the test, it then approaches the first steady-state value. The effluent concentration has a sudden drop at the wormhole breakthrough, it then reaches the second steady-state value for the rest of the test, as shown in Figure 4-9.

As discussed in Section 4.1.1, the effluent concentration can be used to interpret the overall dissolution rate and the evolution of the rock-fluid system. The steady-state value of the effluent concentration indicates that the overall dissolution in the rock-fluid system is in a "quasi-steady state". This quasi-steady state is used to describe the slowly evolving state of the dissolution [Hanna and Rajaram, 1998; Detwiler and Rajaram, 2007], where the geometric evolution of the pore space or the wormholes is much slower than the evolution of the flow and mass transport.

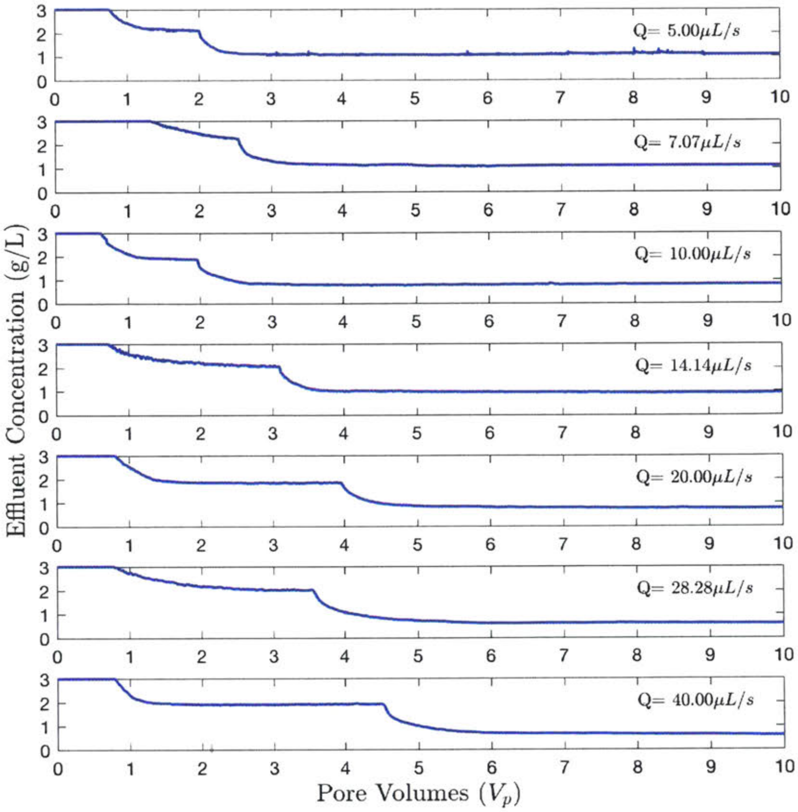

Figure 4-9: Effluent concentration data measured by the ECMS in the seven core flood tests.

Four States during a Core Flood Test

The core flood tests can be divided in two transient states and two quasi-steady states, based on the effluent concentration. Using the effluent concentration data of the test with a flow rate of $Q = 20\ \mu L/s$ as an example, the four states are divided in Figure 4-10.

- A: 0.0-1.5 V_P, initial transient state;
- B: 1.5-4.0 V_P, mixed dissolution quasi-steady state (MDSS);
- C: 4.0-4.5 V_P, breakthrough transient state;
- D: 4.5-end V_P, wormhole dissolution quasi-steady state (WDSS).

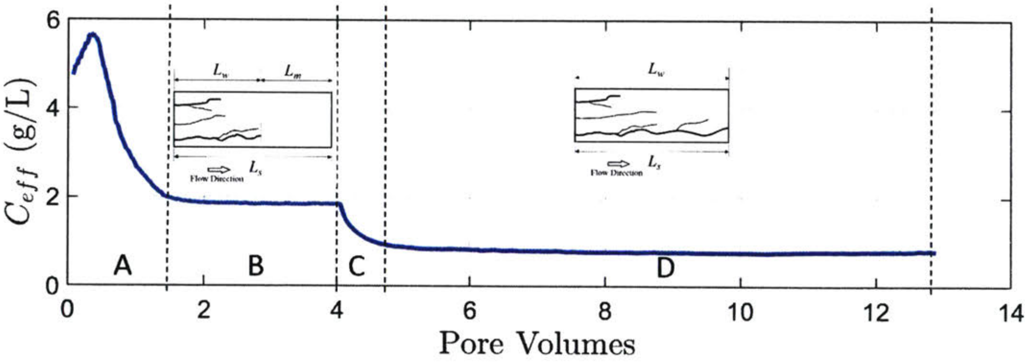

Figure 4-10: Four states during a core flood test based on the effluent concentration data. The core flood test with flow rate $Q = 20\ \mu L/s$ is used as an example.

In the initial transient state, the newly injected distilled water pushed out the initial pore fluid, which had a relatively high concentration (higher than 2.6 g/L) due to the overnight saturation. Both dissolved gypsum and dissolved air contributed to the concentration, making it higher than the equilibrium concentration of the gypsum (2.6 g/L). As the newly injected distilled water replaced the initial pore fluid, the rock-fluid reached the mixed dissolution quasi-steady state. In this state, the wormholes had already developed from the inlet, but not yet reached the outlet as shown in Figure 4-10. Flow and dissolution occur both in the wormholes and in the porous rock matrix, which result in a quasi-steady state value for the effluent concentration (2 g/L).

In the breakthrough transient state, the wormhole breakthrough transformed the flow state from mixed pore flow and wormhole flow to wormhole flow only. In the wormhole dissolution quasi-steady state, since the flow was localized in the wormholes, the gypsum dissolution mostly occurs in the wormholes. The effluent concentration in this state was lower than the effluent concentration in the mixed dissolution quasi-steady state because of the smaller contact area.

The four states discussed above were based on the test with $Q = 20\ \mu L/s$ as an example. The other tests all had these four states, except that the range of pore volume V_p for each state differed with the flow rates. The four states showed the evolution of dissolution kinetics in the rock-fluid system during the core flood tests.

The evolution of dissolution kinetics corresponds to the formation of wormholes as shown with the sketches in Figure 4-10.

Summary of the Quasi-Steady State Effluent Concentrations

The effluent concentrations of the two quasi-steady states are normalized to the equilibrium concentration (solubility $C_{eq} = 2.6g/L$, according to Jeschke et al. [2001]) and are plotted against the injection flux q in Figure 4-11. The normalized effluent concentrations $\frac{C_{eff}}{C_{eq}}$ for the two states are each fitted with a power law curve.

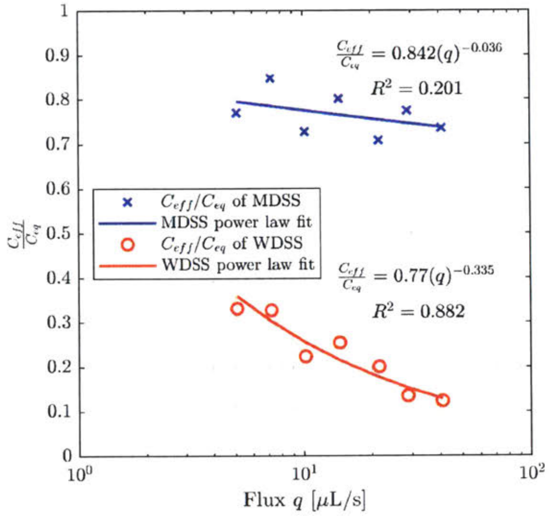

Figure 4-11: Normalized effluent concentrations for mixed dissolution quasi-steady state and wormhole dissolution quasi-steady state.

As shown in Figure 4-11, the effluent concentrations in the mixed dissolution quasi-steady state (MDSS-C_{eff}) are higher than in the wormhole dissolution quasi-steady state (WDSS-C_{eff}). Both quasi-steady state effluent concentrations decrease with the increasing injection flux. In comparison with WDSS-C_{eff}, MDSS-C_{eff} has a smaller power dependence on the flux with the power being -0.036.

The overall dissolution rate's dependence on the flow rate Q can also be estimated. Given that $Q = q \cdot A_s$ (A_s is the specimen cross-section area), injection flux q is proportional to flow rate Q: $q \propto Q$. Based on Equation (4.1) and the power law fit in Figure 4-11, the relation between the injection flow rate and overall dissolution rate can be rewritten as:

$$R_{overall} = Q \cdot C_{eff} \propto Q \cdot q^{n_p} \propto Q \cdot Q^{n_p}, \tag{4.9}$$

where n_p is the power dependence of C_{eff} on q. For the mixed dissolution quasi-steady state, $R_{overall} \propto Q^{0.964}$, while for the wormhole dissolution quasi-steady state, $R_{overall} \propto Q^{0.665}$. The difference in the two quasi-steady states are likely to be the result of different dissolution mechanisms as will be confirmed with the dimensional analysis in Chapter 5.

4.2.4 Initial CT scan

Since the specimens prepared according to Section 3.1.2 had consistent material properties, only one CT scan was conducted on a specimen before the core flood test to represent the initial state of all the other specimens. Since the CT scan had a resolution of 50 μm, it could only resolve pores larger than 50 μm. Therefore the initial pore space analysis based on the CT data covers part of the minor mode in the pore size distribution measured using MIP (Section 3.1.3), which is centered around 100 μm (Figure 3-4). Although the pore space analysis based on the CT data is limited by its resolution, it provides quantitative information about the pores in addition to the MIP data. It is also useful in the wormhole geometry analysis in which the pores and wormholes need to be differentiated.

In the 3D binary matrix, a pore is represented by a cluster of connected elements with value 1. These connected elements can be identified by the MATLAB algorithm as "connected components". Therefore, each connected component is an individual pore, which consists of a certain number N_{vi} of voxels. Since each voxel has the volume: $50 \times 50 \times 50$ μm^3, the volume of the pore is:

$$V_i = N_{vi} \times 50 \times 50 \times 50 \ \mu m^3. \tag{4.10}$$

The equivalent diameter D_i of each pore can be calculated using Equation (4.11):

$$D_i = \sqrt[3]{\frac{6}{\pi} V_i}. \tag{4.11}$$

To eliminate the noise induced by the CT image sensor for a reliable analysis, the 3D binary matrix representing the specimen before the test was filtered by an 8-voxel 3D filter. This initial filter also deleted the pores that were represented by less than eight voxels in the CT scan, which had equivalent diameters less than 124.07 μm based on Equations (4.10) and (4.11).

After applying the initial 3D filter, there were 97,330 pores left in the specimen that were larger than 124 μm. The total volume of these pores normalized by the volume of the specimen is the porosity 0.0092. This indicated that the porosity contributed by pores larger than 124 μm was 0.0092. The specimen and the pores are reconstructed in Figure 4-12(a). The reconstructed pores are isolated from each other and distributed uniformly in the specimen, which does not provide a preferred flow path.

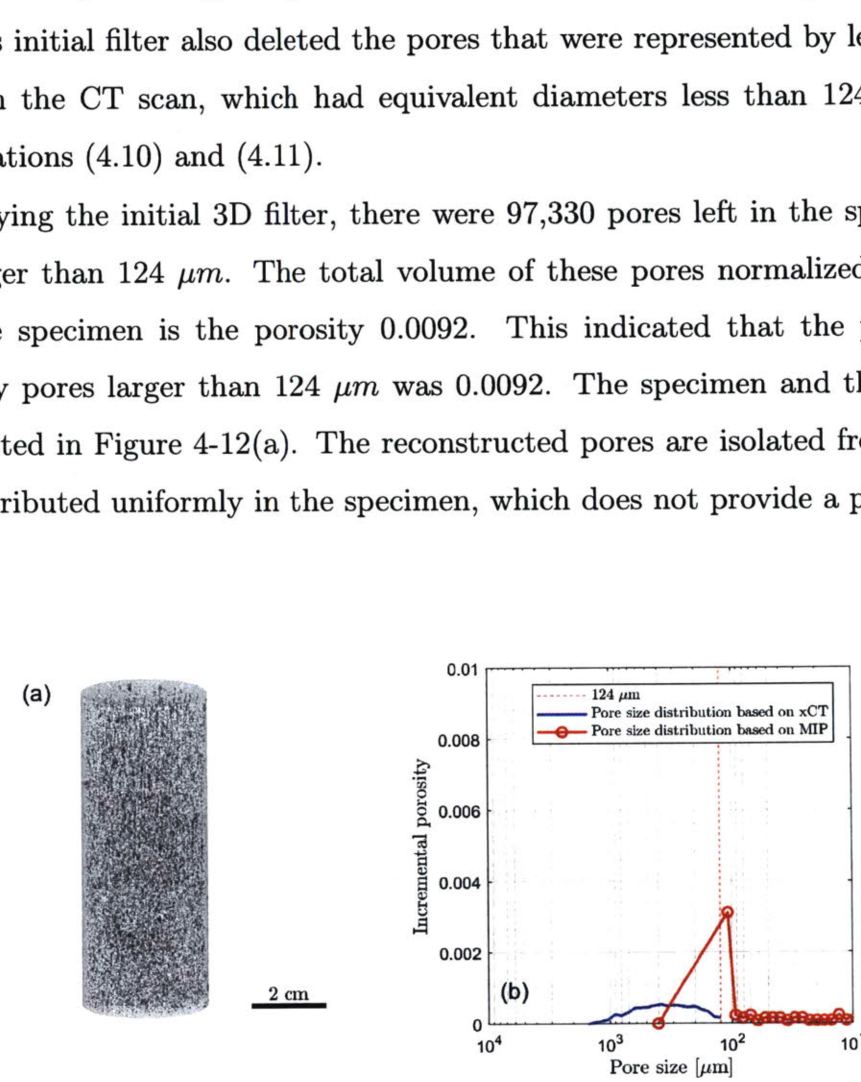

Figure 4-12: Initial pore space analysis. (a) 3D reconstruction of initial pores larger than 124.07 μm. (b) Pore size distribution based on CT data.

Since the pore size and volume are known for each pore, the pore size distribution for pores larger than 124.07 μm can be studied based on the CT data. First, the pores are grouped according to their sizes. Then, the total volume of the pores in each group is calculated and normalized to the specimen volume as the incremental porosity, the porosity contributed by each group of pores. The pores based on the CT scan show a pore size distribution centered around 300 μm and contribute to a porosity of 0.0092 in total, as plotted in Figure 4-12(b).

The pore size distribution measured by MIP is also plotted in Figure 4-12(b) for comparison. The two pore size distributions are different since MIP measures the pore throat diameter while the CT analysis provides the equivalent pore diameter. However, the pore throat diameter and equivalent pore size are roughly in the same order of magnitude. As shown in Figure 4-12(b), MIP has limited resolution for large pores, the incremental porosity of pores larger than 100 μm is around 0.0035. This result is in line with the result of the CT analysis, which is 0.0092.

As discussed in Section 3.2.3, the CT scan resolution (50 μm) is mainly intended to observe the wormholes, so the pores smaller than 50 μm before and after the core flood test were not resolved or compared. The change of the porosity in the gypsum matrix is studied using mass conservation in Section 4.2.7. The initial pore space analysis discussed above can be used to provide a reference for the scale of the pore sizes so that in the wormhole geometry analysis these pores can be eliminated.

4.2.5 3D Wormhole Reconstruction

Similar to the CT scan data processing algorithms in Section 4.2.4, the 3D binary matrices representing the specimens after the core flood tests are used for the wormhole geometry analysis. Given the initial pore space analysis (Section 4.2.4), a 1000-voxel 3D filter was used to eliminate the isolated pores and reveal the wormholes developed in the specimen. The 1000-voxel 3D filter, which has an equivalent diameter of 600 μm, eliminates pores smaller than 600 μm. As shown in Figure 4-12(b), most of the pores have equivalent diameters smaller than 600 μm and are eliminated by this filter.

Another length filter was applied to eliminate pores that are shorter than 5 mm in the axial direction of the specimen. This filter eliminates isolated pores that were not eliminated by the 1000-voxel 3D filter. This filter also eliminates the wormholes that are shorter than 5 mm in the axial direction of the specimen. The 1000-voxel 3D filter and 5 mm length filter were chosen so that the isolated pores can be effectively eliminated and the wormholes can be preserved. The 5 mm length filter also acts as a criterion for the wormhole geometry analysis so that only wormholes longer than 5 mm were accounted for.

After the filtering process discussed above, the 3D binary matrix is used to reconstruct the wormholes. The area that each wormhole projected on each horizontal cross-section A_{ct} is used to calculate the equivalent diameter of the wormhole D_e on each plane:

$$D_e = \sqrt{4A_{ct}/\pi} \tag{4.12}$$

In the 3D binary matrix, the binary elements on each $X - Y$ plane represent a horizontal cross-section of the specimen. The "1" elements on this plane represents the projections of the wormhole on this plane. Each connected component on this plane with N_{ai} "1" elements is a projection with area $A_{ct} = N_{vi} * 50 * 50\ \mu m^2$. Since the wormholes are mostly vertical, their projections on the horizontal cross-section are approximately their cross-sections. Thus, D_e is the a good estimation of the diameter of each wormhole. The 3D rendering of the wormholes and their equivalent diameters are indicated in color in Figure 4-13.

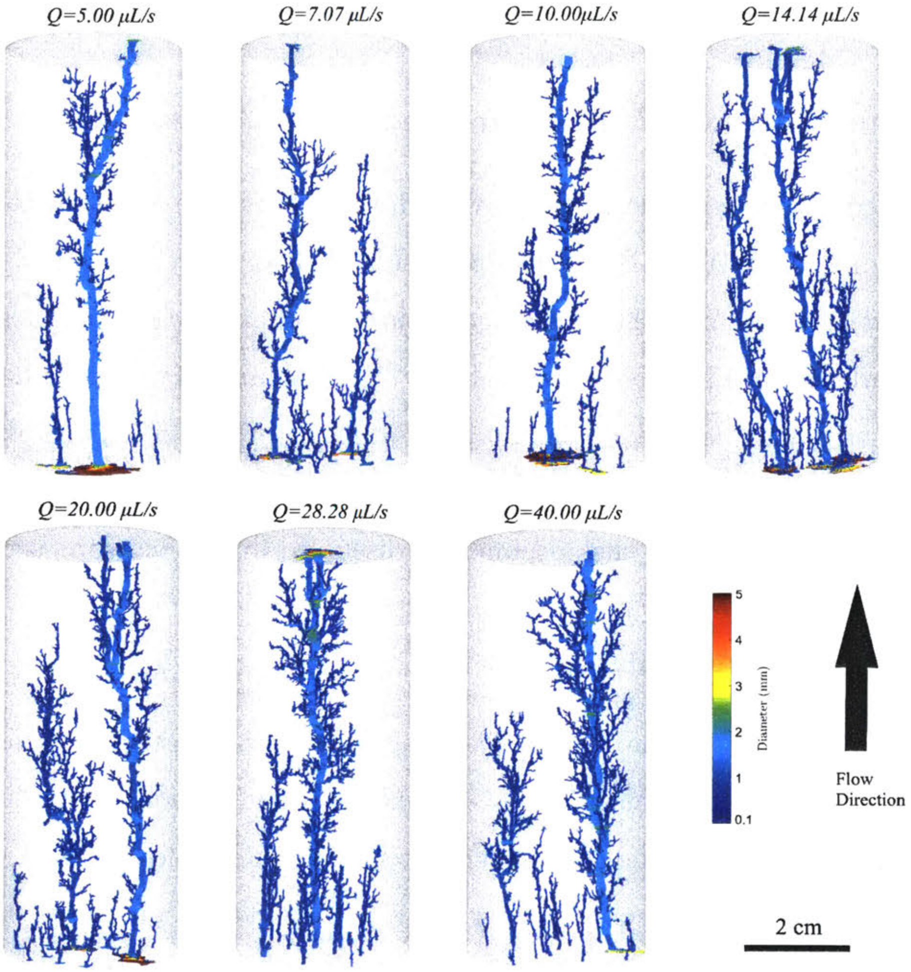

Figure 4-13: 3D reconstructions of the wormholes in each specimen. The wormhole geometries showed that higher flow rates resulted in more complicated wormholes.

The specimens were reconstructed in the same position as they were housed in the triaxial system, i.e., flow entered the specimen from the bottom and exited from the top. Each specimen has one major wormhole, which has the largest diameter and connects the inlet and outlet. There are several secondary wormholes in each specimen, which developed at the inlet of the specimen near the major wormhole. Along the major and secondary wormholes, branches also developed presenting a root-like geometry [Daccord et al., 1993a]. Figure 4-13 shows a generally accepted trend that as the flow rate increases, there are more secondary wormholes, and more branches on the wormholes [Daccord et al., 1993a; Fredd and Fogler, 1998; Budek and Szymczak, 2012].

4.2.6 Quantitative Wormhole Geometry Analyses

To quantitatively analyze the complex wormhole geometry in the specimens, algorithms utilizing the MATLAB Image Processing Toolbox were developed to obtain the parameters of interest. The parameters used to quantify the complexity of the wormholes are: surface area of the wormholes (S_{wh}), volume of the wormholes (V_{wh}), the number of wormholes (N_{wh}), the major wormhole tortuosity (τ_{ac}), and the number of branches on the major wormhole (N_{br}). These parameters are normalized to the associated dimensions of the specimen as discussed in the following sections.

Surface area of the wormholes

The total surface area of the wormholes (S_{wh} $[m^2]$) is calculated based on the 3D binary matrix of the wormholes. The MATLAB built-in function "bwperim" is used on the 3D binary matrix to find the 3D perimeter of the wormholes. This 3D perimeter represents the surface of the wormholes using just the voxels on the surface of the wormholes. Each voxel represents the area: 50×50 μm^2. Thus the surface area of the wormholes (S_{wh}) is the number of surface voxels times $50 \times 50 \mu m^2$.

S_{wh} is then normalized to the volume of the specimen as the wormhole area per specimen volume S_{whN} $[m^{-1}]$. In Figure 4-14(a) the normalized wormhole surface area S_{whN} is plotted as a function of the injection flux. Figure 4-14(a) shows that higher flow rates result in larger S_{whN}. A power law equation is used to fit S_{whN} as a function of the injection flux q. The power law fit shows that the normalized wormhole area (S_{whN}) is proportional to the 0.31 power of the injection flux q.

Volume of the wormholes

The total volume of the wormholes (V_{wh} $[m^3]$) is also calculated based on the 3D binary matrix of the wormholes. The voxels representing the wormholes each has a volume: $50^3 \mu m^3$. Thus the total volume of the wormholes is the number of wormhole voxels times $50^3 \mu m^3$. V_{wh} is then normalized to the volume of the specimen as the wormhole volume per specimen volume V_{whN}[1].

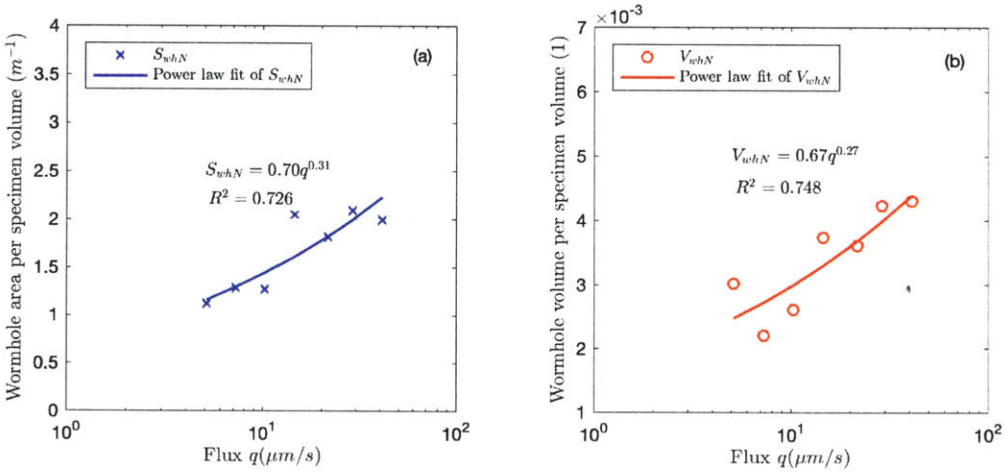

Figure 4-14: (a) Wormhole surface area per specimen volume (S_{whN} $[m^{-1}]$). (b) Wormhole volume per specimen volume (V_{whN} $[1]$)

In Figure 4-14(b) the normalized wormhole volume S_{whN} is plotted as a function of the injection flux. Figure 4-14(b) shows that higher flow rates result in larger V_{whN}. A power law equation is used to fit V_{whN} as a function of the injection flux q. The power law fit shows that the normalized wormhole volume (V_{whN}) is proportional to the 0.27 power of the injection flux q.

Number of wormholes

The number of wormholes (N_{wh}) can be calculated by totaling the number of connected components in the 3D binary matrix that represents the wormholes. Each connected component represent a wormhole that developed from the inlet of the specimen, which may or may not reach the outlet of the specimen. For example, in Figure 4-13 the specimen flooded with $Q = 5.00$ muL/s has seven wormholes, while the specimen flooded with $Q = 40.00$ muL/s has eighteen wormholes. Since all the wormholes initiated from the inlet of the specimen, the number of wormholes for each specimen is normalized by the specimen cross-section area as the number of wormholes per area (N_{whN} $[cm^{-2}]$). The specimen preparation process produced specimens with 35.56mm diameter, so the numbers of wormholes are normalized to the same specimen cross-section area: $1/4\pi \cdot 3.556^2\ cm^2 = 9.93\ cm^2$.

In Figure 4-16(a), N_{whN} is plotted as a function of the injection flux q. A power law equation is used to fit N_{whN} as a functions of the injection flux q. The power law fit shows that the number of wormholes per inlet area (N_{whN}) is proportional to the 0.42 power of the injection flux q, as shown in Figure 4-16(a).

Number of branches on the major wormhole

To calculate the number of branches and the tortuosity of the major wormhole, the major wormhole, secondary wormholes and branches need to be differentiated. Figure 4-15 shows how the morphological algorithms calculate the number of branches step by step. First, the major wormhole with its branches is recognized as the connected component with the largest number of voxels(Figure 4-15(b)). The major wormhole connecting the inlet and outlet can be obtained by tracing the largest continuous wormhole from the outlet to the inlet(Figure 4-15(c)). After eliminating the major wormhole from the 3D binary matrix representing the major wormhole and its branches, the branches on the major wormhole then become isolated components (Figure 4-15(d)). Therefore, the number of branches is the number of isolated components in this matrix.

Given the fractal nature of the wormholes [Daccord, 1987], there are secondary branches developing on the branches from the major wormhole. These secondary branches are counted with the one developing from the major wormhole as one branch, when calculating the number of branches. The number of branches on the major wormhole is used to represent the level of branching of the wormholes. Since the wormhole branches on the major wormhole were developed along the flow direction, the number of branches is normalized by the length of the specimen as the number of branches per specimen length ($N_{brN}\ [cm^{-1}]$).

In Figures 4-16(b) N_{brN} is plotted as a function of the injection flux q. A power law equation is used to fit N_{brN} as a function of the injection flux q. The power law shows that the number of branches per specimen length (N_{whN}) is proportional to

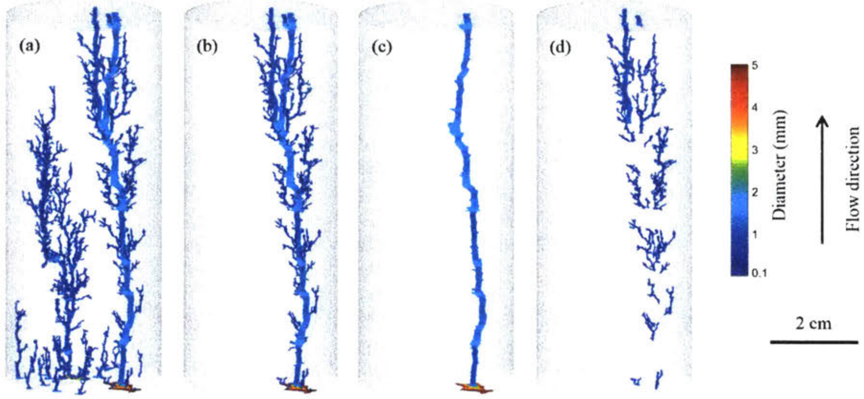

Figure 4-15: Algorithms to calculate number of branches. (a). The major and secondary wormholes resulting from the core flood test with $20\mu L/s$ injection flow rate. (b). The major wormhole with its branches. (c) Isolated major wormhole. (d) Isolated branches of the major wormhole.

the 0.27 power of the injection flux q.

The parameters N_{whN} and N_{brN} are defined and normalized so that wormhole geometry can be compared with other tests with different sizes of specimens. For example, the number of wormholes are normalized to the inlet area because all the wormholes initiated from the inlet. If there are other tests using bigger or smaller specimen diameter, the same normalization methods can be applied so that the results can be compared with the results of the core flood tests. By using N_{whN} and N_{brN} to describe the complexity of the wormhole geometry, the analysis shows the trend that higher flow rates indeed result in higher number of wormholes and branches.

Geometry of the major wormhole

The geometry of the major wormhole is studied based on the isolated major wormhole using the morphological algorithm described in Figure 4-15. The major wormholes are reconstructed in Figure 4-17 with colors representing the diameters. Similar to the 3D rendering of all the wormholes, Equation (4.12) is used to calculate the equivalent radius of the major wormhole. As shown in Figure 4-17, the diameters of the major wormholes is in the range of 1 mm to 2 mm, except the inlet The inlets of the wormholes are larger than the rest of the wormholes. This is caused by the

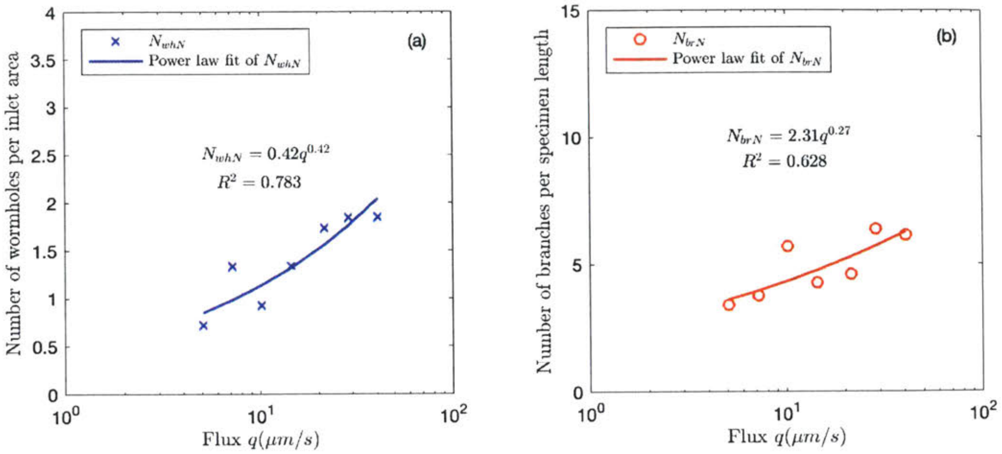

Figure 4-16: (a) The number of wormholes per inlet area (N_{whN}). (b) The number of branches per specimen length (N_{brN}).

non-uniform dissolution along the wormholes, as discussed in studies by Wang et al. (2016) and Smith et al. (2013, 2017).

With the major wormholes reconstructed as shown in Figure 4-17, the length L_t of the major wormhole can be calculated as follows. The coordinates of the center of the major wormhole on each horizontal cross section is calculated by averaging the coordinates of all the voxels that represents the major wormhole on this cross section. This averaging algorithm obtains the coordinates of the geometric center of the major wormhole on each cross section (x_i, y_i, z_i). The distance between the centers of the adjacent two cross sections can be summed to obtain the total length of the major wormhole.

$$L_t = \Sigma_{i=2}^{N} \sqrt{(x_i - x_{i-1})^2 + (y_i - y_{i-1})^2 + (z_i - z_{i-1})^2} \tag{4.13}$$

The tortuosity τ of the major wormhole can also be calculated:

$$\tau = \frac{L_t}{L_s}, \tag{4.14}$$

where L_t is the length of the major wormhole, and L_s is the length of the specimen. This definition tortuosity (Equation 4.14) accounts not only for the local tortuosity

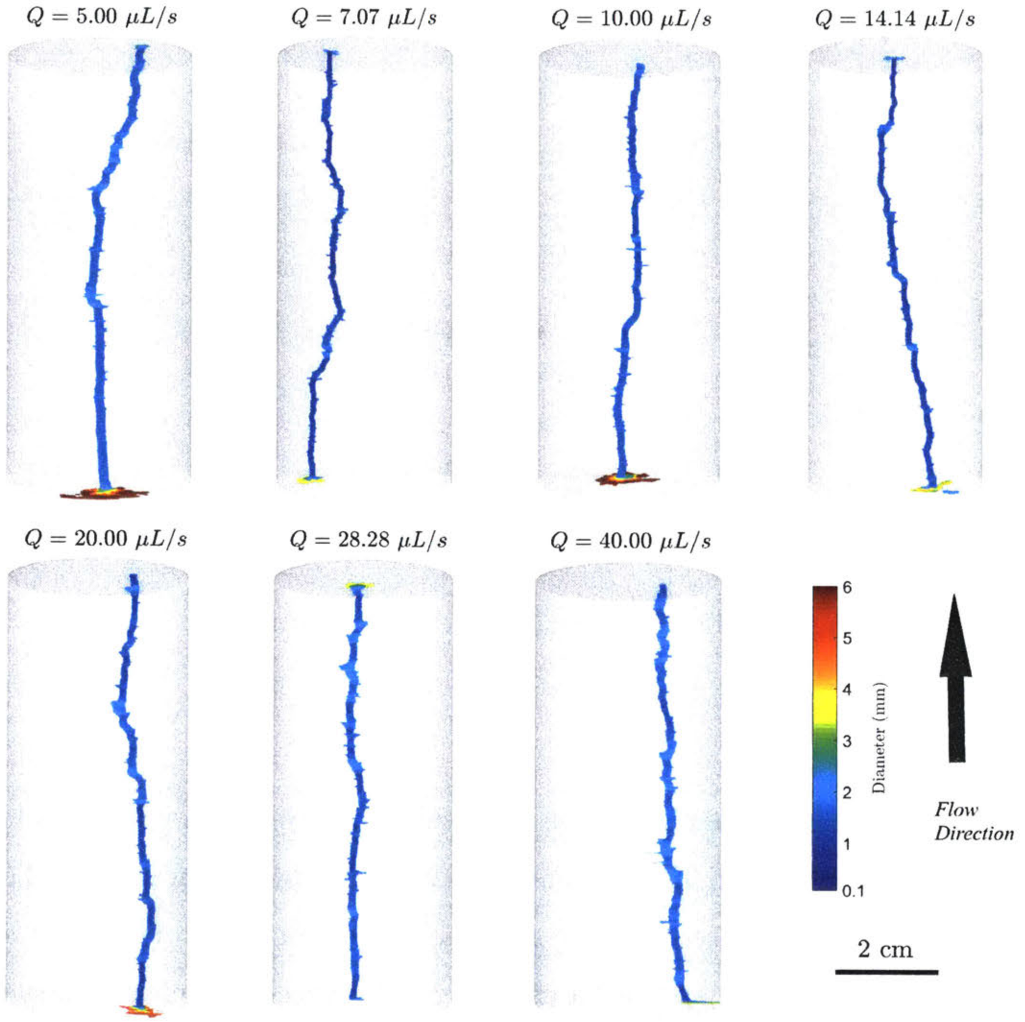

Figure 4-17: 3D reconstruction of the major wormhole.

of the major wormhole but also the overall inclination from the flow direction. As shown in Figure 4-18, the tortuosity (τ) has a small dependence on the flow rate: the higher flow rates result in higher tortuosity τ of the major wormhole.

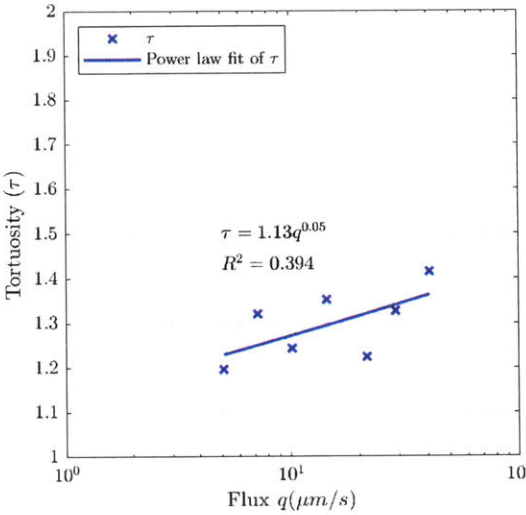

Figure 4-18: Tortuosity of the major wormholes.

Skeleton analysis

The complexity of the wormholes can be studied by analyzing their topological skeletons. The MATLAB built-in 3D skeletonization function "bwskel" was applied on the 3D binary matrices that represent the wormholes in each specimen. The skeletons extracted from the wormholes are shown in Figure 4-19. The skeletonization algorithm reduced the wormholes with tens of voxels in diameter to lines with a single voxel in diameter.

The total length of all the wormholes in each specimen can be calculated based on the skeletons of the wormholes. The skeletonization reduces the diameter of the wormholes to a single voxel, but preserves the lengths of the wormholes. Therefore, the lengths of the skeletons are the same as those of the wormholes. Since the skeleton only has a diameter of one voxel, the voxel length of the skeleton is the number of voxels representing the skeleton. The voxel length of the skeleton can be converted to meters using the scale factor of 50 μm/voxel. Thus, the lengths of the skeletons, which are also the lengths of the wormholes can be calculated. The lengths of the wormholes for each specimen are summarized in Figure 4-20.

As shown in Figure 4-20, the total lengths of the wormholes resulting from the dif-

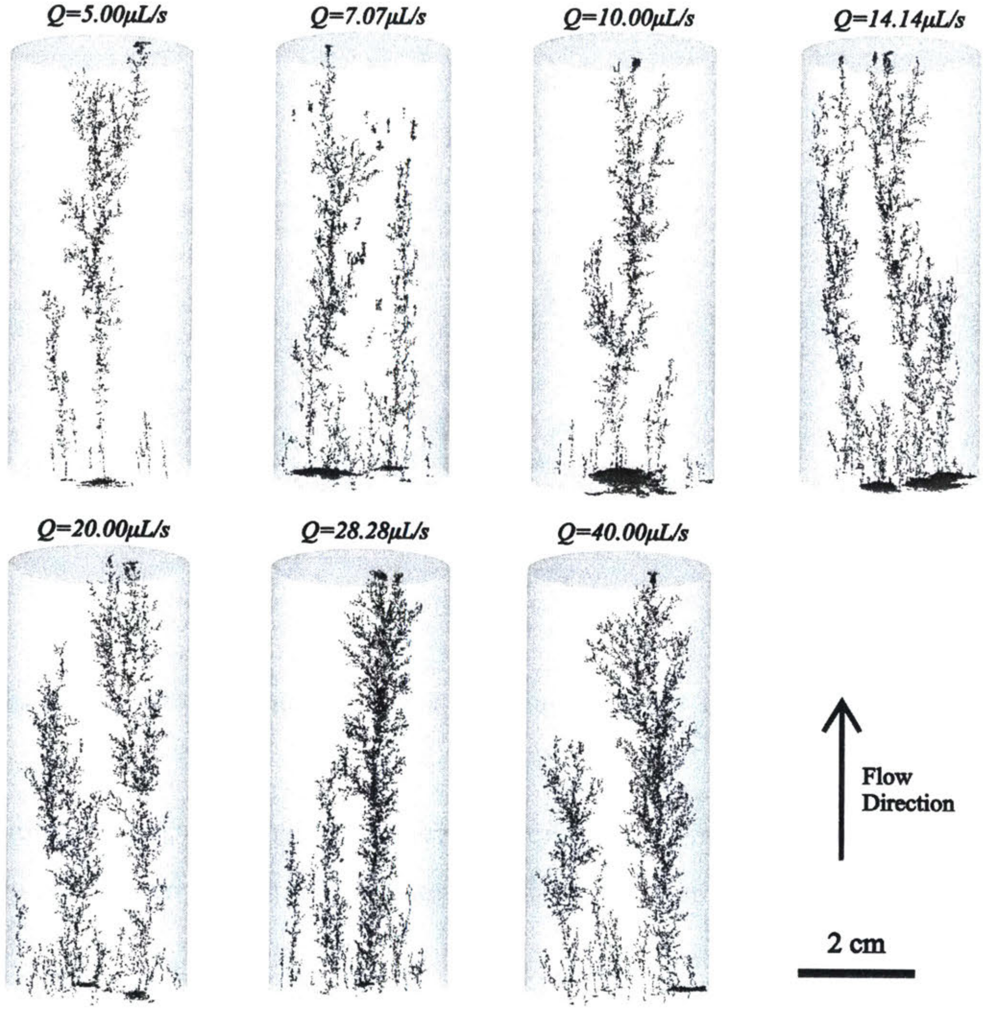

Figure 4-19: Wormhole skeletonization.

ferent flow rates are at the scale of several meters, which are two orders of magnitude longer than the specimens (82.55 mm). Although the length of the major wormhole in each specimen is comparable to the specimen length, the complex branching and meandering of the wormholes result in much longer lengths, collectively. The wormholes resulting from higher flow rates tend to have longer length, except for the wormholes resulting from Q=14.14 $\mu L/s$, as shown with a red circle in Figure 4-20. In the case of Q=14.14 $\mu L/s$, the total length of the wormholes are longer than that of the wormholes resulting from higher flow rates because there are two wormholes connecting the inlet and outlet. This is not a common case for wormhole formation.

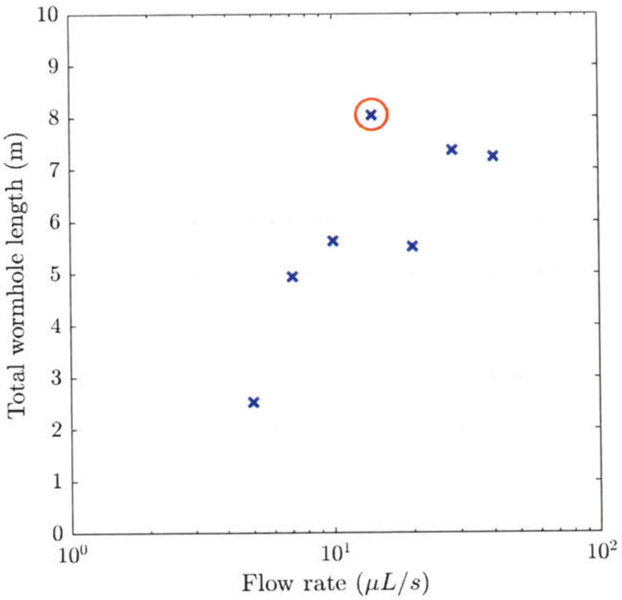

Figure 4-20: Total length of the wormholes in each specimen resulting from different flow rates.

Clearly, if there are two or more wormholes developed independently and connect the inlet and outlet of the specimen, with their branches, the total length is expected to be longer.

Fractal analysis

The wormholes shown in Figure 4-13 exhibit a complex fractal pattern. To quantify the complex geometry of the wormholes and compare the wormholes resulting from different flow rates, the fractal dimension (D_f) is used. The fractal dimension is defined as the ratio providing a statistical index of complexity comparing how details in a pattern (strictly speaking, a fractal pattern) change with the scale at which they are measured. It has also been characterized as a measure of the space-filling capacity of a pattern that indicates how a fractal scales differently in the space it is embedded in [Mandelbrot, 1982; Viscek, 1992; Sagan, 1994; Falconer, 2003]. Higher fractal dimensions indicate more complex geometry. For a fractal geometric pattern in a 3D volume, D_f ranges from 1 to 3.

Since the wormholes are represented by a 3D binary matrix, the box counting method is used to characterize the fractal dimension of these wormholes. The box counting method uses boxes to characterize the details of a fractal pattern. The size of the box represents the scale of observation, while the number of boxes used to cover the fractal pattern represents the level of details. This method finds the relation between the size of the boxes (R_b) and the number of boxes of this size needed to cover the wormholes (N_b). The box scans through the 3D binary matrix with a fixed grid scan strategy, which moves the box the same distance as the size of the box. The results of the box counting of the seven specimens are shown in Figure 4-21.

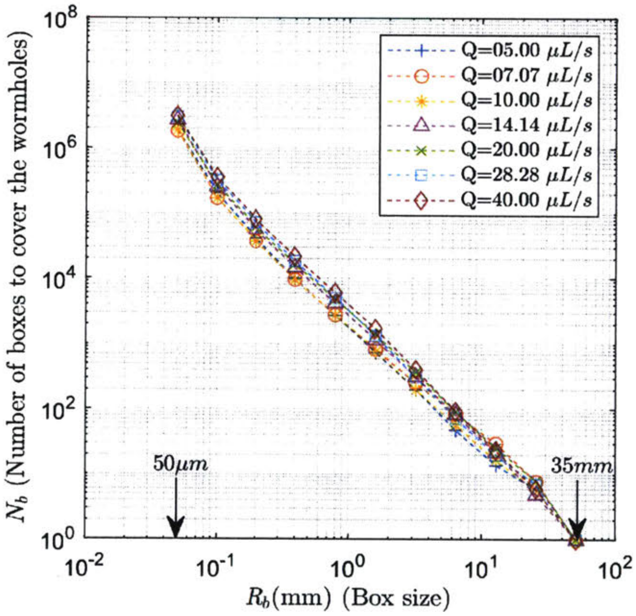

Figure 4-21: Relation between N_b and R_b using box counting method.

Figure 4-21 shows that the number of boxes needed to cover all the wormholes in a specimen decreases with the box size. The relatively similar positioning of the seven curves also indicates that the wormholes in the seven specimens have similar fractal features. When the box size is 50 μm, which is the voxel size of the CT scan, N_b is the number of voxels representing the wormholes. When the box size is around 35mm, which is the diameter of the specimen, only one box is needed, as shown in Figure 4-21.

A linear fit was used to find the relation between $log(N_b)$ and $log(R_b)$, as shown in Figure 4-22. The wormholes resulting from the flow rate Q=5.00 $\mu L/s$ is used as an example. A reasonably good fit was obtained using the linear fit (Figure 4-22). According to the definition of fractal dimension, the slope of this fit is then the fractal dimension D_f,

$$D_f = -\frac{\Delta log N_b}{\Delta log R_b}. \tag{4.15}$$

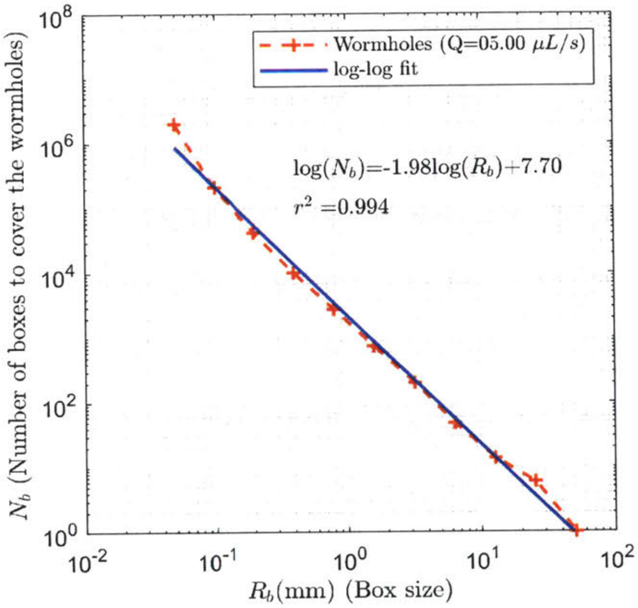

Figure 4-22: Linear fit between $log(N_b)$ and $log(R_b)$, The wormholes resulting from Q=5.00 $\mu L/s$ is used as an example.

As shown in Figure 4-22, the fractal dimension of the wormholes resulting from the flow rate Q=05.00 $\mu L/s$ is 1.98. The fractal dimension (D_f) and the y-intercepts (D_0) of the wormholes in the seven specimens are summarized and plotted in Figures 4-23(a) and (b). The wormholes of the seven specimens have a fractal dimension around 2. This is a relatively high fractal dimension given the wormholes have a tubular geometry and only occupy 0.4% of the total specimen volume, as discussed in Section 4.2.6. Although the wormholes have a small volume, they exhibit topological complexity similar to a two dimensional object. Figure 4-23(a) also shows that the fractal dimensions are higher for wormholes resulting from higher flow rates. The wormhole complexity characterized by fractal dimensions matches the generally accepted conclusion that higher flow rate results in more complex wormholes [Daccord et al., 1993a; Fredd and Fogler, 1998; Budek and Szymczak, 2012].

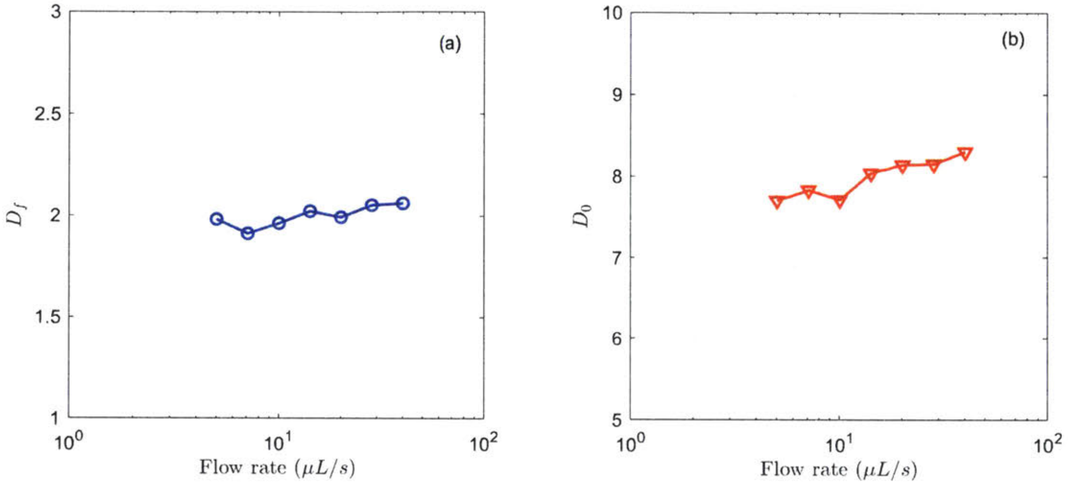

Figure 4-23: Fractal dimension (D_f) and y-intercepts (D_0) of the wormholes resulting from different flow rates. (a) Fractal dimension. (b) y-intercept.

Some researchers used numerical models to simulate the wormhole formation and study the fractal dimensions of the wormholes [Liu and Zhao, 2005; Kalia and Balakotaiah, 2007; Ming et al., 2012]. However, these studies were limited to two-dimensional models and the fractal dimension calculated based on these simulations are in the range of 1.4-1.7. This study showed that the 3D wormholes resulting from the core flood tests have fractal dimensions higher than those resulting from numerical solutions. This analysis can be used as a reference for the numerical studies in the future.

The y-intercept in Figure 4-22 is a factor that depends not only on the wormhole geometry but also on the units used during the analysis. Since the units and analysis methods are consistent across the wormholes of the seven specimens, the relative value can thus be used to evaluate the complexity of the wormholes. In this case, a higher y-intercept indicates more boxes are needed to cover the wormholes, which again indicates higher complexity. As shown in Figure 4-23(b), the y-intercepts also show that higher flow rates indeed result in more complex wormholes.

In sum, with the 3D algorithms discussed above, the complexity of the wormholes is quantified with parameters such as the normalized surface area of the wormholes (S_{whN}), the number of the wormholes per inlet area (N_{whN}), the number of branches per specimen length (N_{brN}), tortuosity (τ) and fractal dimension. These quantitative descriptions of the wormhole geometries show that higher flow rates indeed result in more complex wormhole geometry regarding the surface area of wormholes, the number of wormholes and wormhole branches.

4.2.7 Conservation of Mass and Volume

The conservation of mass and volume during dissolution were studied by (a), measuring the mass of the specimen before and after the test; (b), integrating the effluent concentration with the volume to calculate the dissolved mass; and (c) measuring the wormhole volume using CT scan. The dissolved mass measured using the three methods is much smaller than the mass of the specimen, which results in a limited accuracy of the measurements. In addition, the effluent concentration in the initial transient state is affected by dissolved air, therefore, the study of mass and volume conservation is only qualitative.

The dissolved mass measured using method (a) is around 1 g, which has a total volume of around 0.8 cm^3. The dissolved mass calculated using method (b), by integrating the effluent concentration over the injected volume, is also around 1 g. The wormhole volume measured using the CT scan (method (c)) is around 0.3 cm^3, which excludes the pores smaller than 100 μm. The difference of 0.5 cm^3 dissolved mass should come from the dissolution in the matrix or wormholes smaller than 50 μm in diameter, which were not accounted for by the CT scan. The specimen has a total volume of $85 cm^3$, so the dissolved material from the matrix is only a small part of the specimen contributing less than 1% to the overall porosity. This again shows the effectiveness of wormhole formation in increasing the permeability of the material without dissolving a large amount of material.

4.2.8 Summary of the Core Flood Tests

The continuous effluent concentration data from the ECMS provided useful information on the overall dissolution rate and the evolution of the rock-fluid system during the core flood test. Based on the effluent concentration data, the overall dissolution rate is higher before the wormhole breakthrough than after the wormhole breakthrough. The gypsum-water system in the core flood tests went through four states: initial transient state, mixed dissolution quasi-steady state, breakthrough transient state and wormhole dissolution quasi-steady state. A sudden effluent concentration drop was observed at wormhole breakthrough, which indicated that the wormhole breakthrough concentrates almost all of the flow in the major wormhole and in turn changed the dissolution kinetics. This also inspired the study of dissolution kinetics in the porous matrix and the wormholes using dimensional analysis in Section 5.2.

To study the rate of wormhole growth and breakthrough pore volume of the gypsum-water system, the flow and pressure data were analyzed and compared with the results from the literature. During the core flood tests, the wormholes developed with a constant rate of growth. This behavior is consistent with the observation by Daccord et al. [1993a]. The wormhole growth rates of our core flood tests have a power dependence on the injection flux, with a power of 0.581. This result is close to the power 2/3 reported by Daccord et al. [1993a]. The analyses also showed that with higher injection flow rates, it requires more pore volumes of fluid to be injected to breakthrough the specimen. The dependence of breakthrough pore volume on the inverse Damköhler number is consistent with the results summarized by Fredd and Fogler [1998] for various rock-fluid systems.

The CT scan was used to observe the pore space and wormholes before and after the core flood tests. The CT scan had limited resolution for all the pores, but was able to resolve the minor mode of the pore size distribution measured by MIP. 3D topological and morphological algorithms were developed to provide quantitative descriptions of the wormholes, such as the wormhole surface area, the wormhole volume, the number of wormholes, the number of branches and, fractal dimensions. These parameters were used to quantitatively study the effect of flow rate on the wormhole geometries. The wormhole geometry analyses showed that higher flow rates result in larger wormhole surface area and volume, a higher number of wormholes, more branches and higher fractal dimensions.

The ECMS and quantitative wormhole geometry analyses provided new perspectives for the current studies regarding the dissolution kinetics and wormhole geometries. The ECMS showed the evolution of dissolution kinetics in the rock-fluid system caused by the formation of wormholes. The CT analyses quantified the complex geometries of the wormholes, and compared the wormholes resulting from different flow rates using the quantitative parameters such as the number of wormholes and branches. The use of laboratory cast gypsum specimens facilitated the systematic study of the effect of flow rate on the dissolution of the gypsum rock matrix and the formation of wormholes. Given the consistent properties of the gypsum specimen and its relatively simple reaction with water, this experimental study can be used as an analog and a reference for more complex rock-water systems, for example, a calcite-HCl system. The innovations of the experimental methods, especially the ECMS, can also be calibrated to study other rock-fluid systems and the dissolution in rock fractures.

Chapter 5

Theoretical Models

This chapter presents the theoretical models that were developed in parallel with the experimental studies. The experimental studies presented in Chapter 4 inspired the development of these theoretical models and provided validation for these models. The theoretical models, in turn, provided more insight into the experimental observations. The models can also be used to predict the evolution of the rock-fluid systems under different flow conditions.

This chapter first presents the development of the extended Graetz solution, which is a 2-D analytical solution for transport-controlled dissolution in an enlarging tapered tube. The classic Graetz solution for transport-controlled dissolution in a cylindrical tube is revisited first. Then, the governing equation for the transport-controlled dissolution in an enlarging tapered tube is formulated and solved, which is referred to as the extended Graetz solution. To demonstrate its application, the extended Graetz solution is used to predict the dissolution in a gypsum cavity in an example. A 2D numerical model is also used to predict the dissolution and provide numerical validation for the extended Graetz solution. Reaction-controlled dissolution in a similar case is also used to provide a comparison with the extended Graetz solution. The results of the tube flow tests presented in Section 4.1 are then used as experimental validation for the extended Graetz solution.

For flow and dissolution in a porous rock matrix, a continuum approach is used to model the physical processes. The development of the continuum model is based on the experimental observation of the effluent concentration and wormhole formations. To account for the flow condition when estimating the effective surface area, this study proposes a relation between the effective surface area and flow rate (injection flux) based on the wormhole geometry. Parallel tube modeling is used to validate this proposed relation.

The continuum model is used to simulate the flow and dissolution in the porous rock matrix, while the extended Graetz solution is used to simulate the flow and dissolution in the wormholes. The lengths of the rock matrix section and the wormhole section can be predicted using the pressure data based on Daccord's conceptual model for wormholed porous rock. Combining these three models, a model for core flood test (MCFT) is developed to simulate the flow and dissolution in the specimens during core flood tests. MCFT simulates the wormhole formation, wormhole breakthrough, and the evolution of the dissolution kinetics in the rock-fluid system, which match the core flood test result reasonably well.

5.1 The Extended Graetz Solution

5.1.1 Dissolution in a Cylindrical Tube

When fluid flows through a cylindrical tube in a soluble material, the soluble material will dissolve into the flowing fluid. This is a simplified model for dissolution in underground cavities (caves, wormholes and fractures) in general. The dissolution in a cylindrical tube model has been widely used for theoretical studies on the evolution of a single cavity [Tang et al., 1981; Berkowitz and Zhou, 1996; Bekri et al., 1997; Dijk and Berkowitz, 1998; Hanna and Rajaram, 1998; Detwiler et al., 2001; Szymczak and Ladd, 2004, 2006, 2012; Yang, 2012; Elkhoury et al., 2013; Ameli et al., 2014] and flow networks [Sudicky and Frind, 1982; Hoefner and Fogler, 1988; Bryant et al., 1993; Groves and Howard, 1994a, b; Howard and Groves, 1995; Li et al., 2006; Bernabé, 1995, 1996; Buijse et al., 1997; Fredd and Fogler, 1998; Szymczak and Ladd, 2006; Cohen et al., 2008].

As discussed in Chapter 2, the dissolution process can be transport-controlled, reaction-controlled or a mixture of the two, depending on the reaction rate relative to transport rate. The underground gypsum dissolution kinetics are generally considered to be transport-controlled [Liu and Nancollas, 1971; Barton and Wilde, 1971; Kemper et al., 1975; Christoffersen et al., 1976; James and Lupton, 1978; Keisling et al., 1978; Navas, 1990; Ohmoto et al., 1991]. For transport-controlled dissolution in a cylindrical tube, the dissolution mass flux q_w at the solid-liquid interface can be formulated as:

$$q_w = k_t(C_{eq} - C_b) \tag{5.1}$$

where k_t is the transport-controlled dissolution rate coefficient; C_{eq} is the equilibrium concentration of the solute; C_b is the bulk concentration of the fluid. The bulk concentration is defined as:

$$C_b(z) = \frac{\int_0^R 2\pi r v_z(r) C(r,z) dr}{\int_0^R 2\pi r v_z(r) dr} = \frac{\int_0^R 2\pi r v_z(r) C(r,z) dr}{Q}. \tag{5.2}$$

where R is the radius of the tube; r is the radial coordinate; z is the axial coordinate along the tube; $v_z(r)$ is the axial velocity; $C(r,z)$ is the concentration in the tube; Q is the flow rate in the tube. The bulk concentration is the amount of solute carried by the flow. In a flow experiment, the measured effluent concentration is the bulk concentration.

The transport-controlled dissolution rate coefficient k_t is often determined by the hydrodynamic conditions. Analytical models have been developed to calculate k_t for corresponding hydrodynamic conditions, such as dissolution on a rotating disk [Levich, 1962] and dissolution in a cylindrical tube [Graetz, 1882].

The Graetz solution

The transport-controlled dissolution rate coefficient k_t for dissolution in a cylindrical tube can be calculated based on the Graetz solution [1882]. For transport-controlled dissolution, the solid-fluid interface is in thermodynamic equilibrium condition, of which the concentration is the equilibrium concentration C_{eq} (Figure 5-1(b)). This is analogous to the heat transfer problem in which a fluid with its initial temperature enters a cylindrical tube with constant wall temperature. Graetz [1882] derived the analytical solution to solve this heat transfer problem. The governing equations are solved in dimensionless form using the infinite series (the detailed solution is presented in the Appendix B, Equation (B.6)). The concentration profile in the tube and the bulk concentration along the tube are shown in Figure 5-1(b) and (a), respectively.

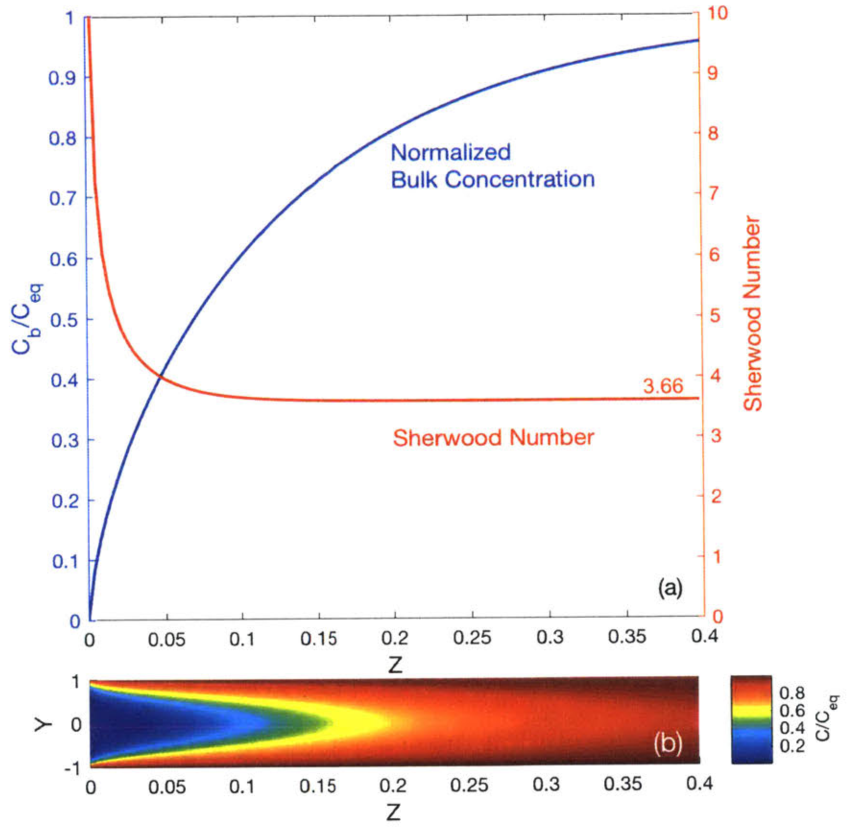

Figure 5-1: The Graetz solution. (a). The Sherwood Number (red) and normalized bulk concentration (blue). The Sherwood number is high in the entrance region of the tube, then asymptotically approaches 3.66. The normalized bulk concentration increases very fast in the entrance region, then slowly approaches 1. (b). The normalized concentration profile in the tube. Y is the dimensionless radial coordinate, where ±1 indicate the solid-liquid interface. The thickness of the diffusion boundary layers increase along the tube, which coalesce at around $Z = 0.1$.

The Sherwood number is introduced as a dimensionless quantity representing the ratio of mass transfer rate to the diffusion rate, which is the dimensionless form of the transport-controlled dissolution rate coefficient (k_t). The transport-controlled dissolution rate coefficient k_t in Equation (5.1) can thus be calculated as:

$$k_t = \frac{D \cdot S_h}{2R}, \tag{5.3}$$

where R is the radius of the cylindrical tube; D is the diffusion coefficient; S_h is the Sherwood number. According to Graetz [1882], the Sherwood number is higher near the entrance and asymptotically approaches 3.66 (Figure 5-1(a)). The higher Sherwood number indicates a higher mass transport rate, as a result of which more solid dissolves near the entrance.

Problem description

The Graetz solution has been proven to be useful in modeling the transport-controlled dissolution in cylindrical tubes. However, its validity domain is not necessarily well understood. For instance, a dissolution rate coefficient calculated from the asymptotic value (3.66) of the Sherwood number is often used, ignoring the higher rate in the entrance region, which induces error in the mass conservation calculation. According to Budek and Szymczak [2012], the non-uniform dissolution along the tube reshapes the cylindrical tube into a enlarged tapered tube. The tapered tube has larger area in contact with the fluid and induces radial flow, which no longer satisfies the assumptions of the Graetz solution. Yet, in some models, the Sherwood number for the cylindrical tube was used for the tapered tube without formal justification.

A 2-D analytical model is developed to explicitly study the effect of tube enlargement and induced radial flow in a tapered tube. By adopting the coordinate transform introduced by Zerkle and Sunderland, [1968], the 2-D mass conservation equation is solved with the same dimensionless form as the Graetz solution. Thus the Graetz solution can be extended to model the dissolution in an enlarged tapered tube. This also provides a formal justification that the Sherwood number for a cylindrical tube can be used for the entrance region and the following region of the tapered tube. With the help of a quasi-steady state approximation, the extended Graetz solution can be used to model the geometric evolution of the tube. In addition, a 2-D finite volume model is developed to validate the extended Graetz solution. Finally, a comparison is made between the transport-controlled dissolution- and reaction-controlled dissolution models with regard to their behavior during the dissolution process.

5.1.2 Dissolution in an Enlarging Tapered Tube

As the geometry of the tube evolves due to dissolution, the flow and transport problems become hard to model due to the moving boundary. However, in an underground reactive transport system, the timescale required for the pressure and concentration fields to reach equilibrium is much shorter than the timescale required for significant alteration of the tube geometry. This allows one to use quasi-steady state concentration to calculate the rate of change in the radius and update the geometry for the next step of the transport calculation. This simulation method is referred as the quasi-steady state approximation [Hanna and Rajaram, 1998; Detwiler et al., 2001; Detwiler and Rajaram, 2007; Szymczak and Ladd, 2009, 2011, 2013], and is used in the following derivations for flow and mass transfer.

The higher dissolution rates near the inlet cause non-uniform dissolution along the tube. More solid dissolves near the inlet, transforming an initially cylindrical tube (Figure 5-2(a)) into a enlarged tapered tube (Figure 5-2(b)), as discussed by Budek and Szymczak [2012]. A cylindrical coordinate system (r, z) is used in the following discussion as shown in Figure 5-2(b). Assume the profile of the tube is a function of the axial coordinate: $R = R(z)$, with the inlet radius being R_1. The exact profile $R = R(z)$ is not prescribed for now, since it does not affect the derivation, as will be discussed in Section 5.1.3.

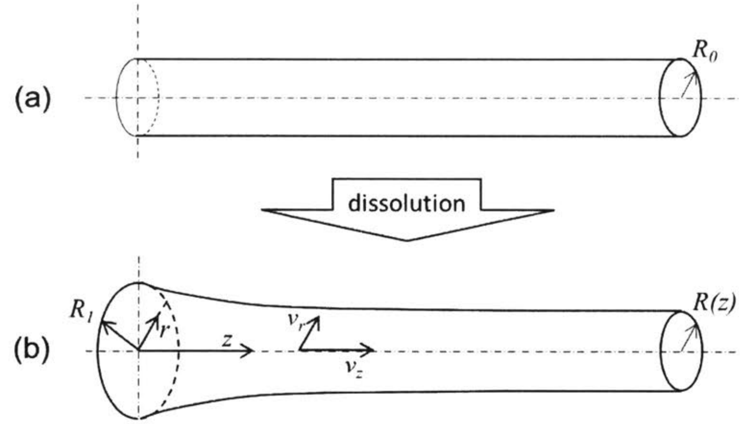

Figure 5-2: Tapered tube and velocities (v_z and v_r) in the cylindrical coordinates $r-z$

5.1.3 Analytical Solution for Transport-Controlled Dissolution in a Tapered Tube

Flow velocity field

Laminar flow in a tapered tube with gradually varying radii has been studied by Oka and Takami [1967] and Zerkle and Sunderland [1968]. The fully developed velocity profile (v_z, v_r) in the tapered tube can be expressed in cylindrical coordinates (r-z):

$$v_z(r,z) = 2\bar{v}_{z1} \cdot \left(\frac{R_1}{R}\right)^2 \cdot \left(1 - \frac{r^2}{R^2}\right) \tag{5.4a}$$

$$v_r(r,z) = 2\bar{v}_{z1} \cdot \left(\frac{R_1}{R}\right)^2 \frac{\partial R}{\partial z} \cdot \left(1 - \frac{r^2}{R^2}\right) \cdot \frac{r}{R}, \tag{5.4b}$$

where $\bar{v}_{z1}$ is the average velocity at the inlet, $\bar{v}_{z1} = \frac{Q}{\pi R_1^2}$, and $\frac{\partial R}{\partial z}$ is the gradient of the radius in the z direction. Since the radius profile $R = R(z)$ is prescribed, $\frac{\partial R}{\partial z}$ can be treated as a known parameter. Equations (5.4) show that the axial flow velocity v_z has the parabolic profile in each cross section and that the radial flow velocity v_r is proportional to the local gradient of radius $\frac{\partial R}{\partial z}$.

The length of the hydrodynamic entrance region is: $0.2 R_e R$, while the length of the mass transfer entrance region is $0.2 P_e R$ [Bird et al., 2007], with R_e and P_e being the Reynolds number ($R_e = 2R_0 v_z \rho/\mu$) and the Péclet number ($P_e = 2R_0 v_z/D$), respectively. The relation between the two dimensionless quantities is: $P_e = S_c \times R_e$, where S_c is the Schmidt number. The Schmidt number is the ratio of momentum diffusion coefficient (kinematic viscosity, ν) to mass diffusion coefficient (D).

$$S_c = \frac{\nu}{D} \tag{5.5}$$

For the underground gypsum dissolution problem, ν and D are in the order of $10^{-6}\ m^2/s$ and $10^{-9}\ m^2/s$ (Jeschke et al., 2001), so the Schmidt number is in the order of 10^3. The hydrodynamic entrance region is much shorter than the mass transfer entrance region and can be neglected. It is thus reasonable to use the fully developed velocity profile (Equations (5.4, b)) in the mass transport models.

Mass conservation of the solute in a tapered tube

Using the quasi-steady state approximation, the mass conservation equation for the solute ($C = C(r,\ z)$) in a tapered tube can be expressed as:

$$0 = -v_z \cdot \frac{\partial C}{\partial z} - v_r \frac{\partial C}{\partial r} + D\frac{\partial^2 C}{\partial z^2} + D\frac{1}{r}\frac{\partial}{\partial r}\left(r\frac{\partial C}{\partial r}\right); \tag{5.6}$$

with the boundary conditions being:

$$\frac{\partial C}{\partial r}|_{r=0} = 0 \quad \text{(axisymmetric boundary condition)} \tag{5.7a}$$

$$C|_{r=R} = C_{eq} \quad \text{(thermodynamic equilibrium boundary condition)} \tag{5.7b}$$

$$C|_{z=0} = 0 \quad \text{(distilled water inflow).} \tag{5.7c}$$

Similar to the simplification made in the Graetz solution [Graetz, 1882], this solution considers the case when the Péclet number $P_e \geq 100$ and the axial diffusion term $D\frac{\partial^2 C}{\partial z^2}$ can be neglected. Upon defining the dimensionless quantities:

$$Z = \frac{z}{R_1 P_{e1}} = \frac{Dz}{2R_1^2 \bar{v}_{z1}}, \quad P_{e1} = \frac{\bar{v}_{z1} \cdot 2R_1}{D} \text{ and } \theta = \frac{C_{eq} - C}{C_{eq}}, \tag{5.8}$$

and the transformed dimensionless radius:

$$Y_s = \frac{r}{R}. \tag{5.9}$$

The coordinates transform from $z - r$ to $Z - Y_s$ transforms the solution domain from a irregular shape bounded by $(0 < z < L, 0 < r < R(Z))$ to a rectangle bounded by $(0 < Z < L/(R_1 P_{e1}), 0 < Y_s < 1)$. This makes the solution easier, as shown in the following derivation. This coordinate transform is adopted from the article by Zerkle and Sunderland, [1968], in which the heat transfer in a tapered tube was modeled.

The derivatives with regard to $z - r$ can be expressed in the transformed $Z - Y_s$ coordinates as:

$$\frac{\partial}{\partial r} = \frac{\partial Y_s}{\partial r}\frac{\partial}{\partial Y_s} + \frac{\partial Z}{\partial r}\frac{\partial}{\partial Z} = \frac{1}{R}\frac{\partial}{\partial Y_s} \tag{5.10a}$$

$$\frac{\partial}{\partial z} = \frac{\partial Y_s}{\partial z}\frac{\partial}{\partial Y_s} + \frac{\partial Z}{\partial z}\frac{\partial}{\partial Z} = \frac{1}{R}\frac{\partial R}{\partial z} \cdot Y_s \frac{\partial}{\partial Y_s} + \frac{1}{R_1 P_{e1}}\frac{\partial}{\partial Z}. \tag{5.10b}$$

The mass conservation equation (Equations (5.6)) can be rewritten in the transformed dimensionless coordinates $Z - Y_s$:

$$v_z \cdot \left(\frac{1}{R}\frac{\partial R}{\partial z} \cdot Y_s \frac{\partial \theta}{\partial Y_s} + \frac{1}{R_1 P_{e1}}\frac{\partial \theta}{\partial Z}\right) + v_r \cdot \frac{1}{R}\frac{\partial \theta}{\partial Y_s} = \frac{D}{R^2}\frac{1}{Y_s}\frac{\partial}{\partial Y_s}\left(Y_s \frac{\partial \theta}{\partial Y_s}\right). \tag{5.11}$$

The two terms on the left side of the equation represent the axial advection and radial advection respectively. The term on the right side of the equation represents radial diffusion. Since $R = R(z)$ and $\frac{\partial R}{\partial z}$ are prescribed as a known parameter, Equation (5.11) is a partial differential equation of $\theta(Y_s,\ Z)$. With the velocity profile Equations (5.4), the transport equation can be rewritten as:

$$\begin{aligned}&2\bar{v}_{z1}\left(\frac{R_1}{R}\right)^2(1-Y_s^2)\cdot\left(\frac{1}{R}\frac{\partial R}{\partial z}\cdot Y_s\frac{\partial\theta}{\partial Y_s}\right)+2\bar{v}_{z1}\left(\frac{R_1}{R}\right)^2(1-Y_s^2)\cdot\left(\frac{1}{R_1P_{e1}}\frac{\partial\theta}{\partial Z}\right)\\&\underline{-2\bar{v}_{z1}\cdot\left(\frac{R_1}{R}\right)^2\frac{\partial R}{\partial z}\cdot Y_s\left(1-Y_s^2\right)\cdot\frac{1}{R}\frac{\partial\theta}{\partial Y_s}}=\frac{D}{R^2}\frac{1}{Y_s}\frac{\partial}{\partial Y_s}\left(Y_s\frac{\partial\theta}{\partial Y_s}\right)\end{aligned} \tag{5.12}$$

The underlined radial advection term in Equation (5.12) is canceled by the first term. Then Equation (5.12) can be simplified into the form (Equation 5.13a) with its boundary conditions (Equations 5.13b, c, d):

$$(1-Y_s^2)\frac{\partial\theta}{\partial Z}=\frac{1}{Y_s}\frac{\partial}{\partial Y_s}\left(Y_s\frac{\partial\theta}{\partial Y_s}\right)\quad(0<Z<\infty,\ \ 0<Y_s<1) \tag{5.13a}$$

$$\theta|_{Y_s=1}=0 \tag{5.13b}$$

$$\frac{\partial\theta}{\partial Y_s}|_{Y_s=0}=0 \tag{5.13c}$$

$$\theta|_{Z=0}=1. \tag{5.13d}$$

Equation (5.13) is the same as the dimensionless governing equation of the Graetz solution (Equation (B.5)). The dimensionless solution developed by Graetz, [1882] can be applied to solve Equation (5.13). According to the definition of the dimensionless quantities (Equations 5.8), the transformed $Z-Y_s$ coordinates will not affect the calculation of the bulk concentration (C_b) and Sherwood number. With the infinite series solution in the transformed $Z-Y_s$ coordinates, the bulk concentration C_b and Sherwood number S_h can be expressed as:

$$C_b(Z)=C_{eq}+C_{eq}\cdot 4\sum_{n=1}^{\infty}A_n\frac{exp\left(-\lambda_n^2Z\right)}{\lambda_n^2}\frac{\partial\phi_n}{\partial Y_s}|_{Y_s=1}, \tag{5.14}$$

$$S_h(Z)=\frac{\sum\limits_{n=1}^{\infty}A_ne^{-\lambda_n^2Z}\frac{\partial\phi_n}{\partial Y_s}|_{Y_s=1}}{2\sum\limits_{n=1}^{\infty}A_n\frac{e^{-\lambda_n^2Z}}{\lambda_n^2}\frac{\partial\phi_n}{\partial Y_s}|_{Y_s=1}}. \tag{5.15}$$

The dimensionless axial coordinate Z (Equation (5.8)) has the denominator $2R_1^2\bar{v}_{z1}$, which is a function of flow rate instead of tube geometry given that $2R_1^2\bar{v}_{z1} = 2Q/\pi$. The tapered geometry does not affect the application of Graetz solution to solve for bulk concentration ($C_b(Z)$) and Sherwood number (S_h). The above derivation shows that the Graetz solution can be extended to solve the governing equation of the transport-controlled dissolution in a tapered tube. It is referred as extended Graetz solution in the later discussion.

The above analysis also produces an unexpected conclusion: the Sherwood number for a tapered tube is the same as that for a cylindrical tube. Intuitively, the tapered tube geometry induces radial flow and has larger contact area with the flowing fluid, which should enhance dissolution. The Sherwood number is the dimensionless transport-controlled dissolution rate, which in this case should be higher. However, the above analysis shows that the tapered tube does not affect the dissolution rate, and that Sherwood number $S_h(Z)$ and bulk concentration $C_b(Z)$ for a tapered tube are the same as those for a cylindrical tube. An explanation for this conclusion is provided in Section 5.1.5.

5.1.4 The Formulation of the Extended Graetz Solution

Since the extended Graetz solution can be used to model transport-controlled dissolution in a tapered tube, it is useful for modeling gypsum dissolution especially in the later stage when the enlarged tapered tube has been formed. Since the geometry of the tube and the velocity of the fluid are both evolving, the formulation using radius and velocity needs to be updated for every time step, as discussed by Budek and Szymczak [2012]. To take advantage of the invariant quantities (such as length of the tube L and flow rate along the tube Q) in the system, the following governing equations are proposed.

Bulk concentration

Based on the mass conservation of the solute, the governing equation for the bulk concentration is:

$$Q \cdot \Delta C_b = 2\pi R \Delta z \cdot q_w = 2\pi R \Delta z \cdot k_t(C_{eq} - C_b), \tag{5.16}$$

Equation 5.16 describes the change of C_b in distance Δz along the tube which is contributed by the transport-controlled dissolution flux q_w. By taking the limit $\Delta z \to 0$ and applying $k_t = \frac{S_h \cdot D}{2R}$, Equation (5.16) can be rewritten as:

$$\frac{dC_b}{dz} = \frac{\pi S_h \cdot D}{Q}(C_{eq} - C_b). \tag{5.17}$$

The Sherwood number S_h in Equation (5.17) is a function of the dimensionless axial coordinate Z. As discussed in Section 5.1.3, the dimensionless axial coordinate Z can be expressed as:

$$Z = \frac{\pi D}{2Q} \cdot z. \tag{5.18}$$

Where D is the mass diffusion coefficient and Q is the volumetric flow rate in the tube. Given the conservation of the fluid in the tube, Q is a constant along the tube, which simplifies the calculation of the dimensionless axial coordinate Z. Equation (5.15) or a fitted approximation [Lienhard, 2013] can be used to obtain the Sherwood number. For example:

$$S_h(Z) = 3.657 + \frac{0.0018(\frac{Z}{2})^{-1/3}}{\left(0.04 + (\frac{Z}{2})^{2/3}\right)^2} \tag{5.19}$$

Equation (5.17) explicitly uses the Sherwood number S_h instead of the dissolution rate coefficient k_t, because k_t is a function of the evolving radius $R(z)$. This form of the extended Graetz solution is easier to be applied for the dissolution in an enlarged tapered tube than using k_t and updating k_t for the evolving geometry. Equation (5.17) also shows that for transport-controlled dissolution in a tube, the bulk concentration is not a function of the geometry but a function of flow rate. Moreover, for a enlarging tube with time-invariant flow rate, the bulk concentration $C_b(z)$ will also be time-invariant despite the evolving geometry.

Rate of tube enlargement

With the Sherwood number and bulk concentration calculated, the rate of tube enlargement can be calculated based on the volume conservation of solid mass:

$$\Delta V = 2\pi R \cdot \Delta R \cdot \Delta Z = \frac{\Delta m}{\rho_r} = \frac{2\pi R \Delta Z \cdot q_w \cdot \Delta t}{\rho_r}, \tag{5.20}$$

where ρ_r is the density of the solid. Equation (5.20) shows the change of solid volume is caused by the dissolved mass. The dissolved mass can be calculated using the dissolution mass flux q_w. By taking the limit $\Delta t \to 0$, and replacing the dissolution mass flux q_w with $\frac{S_h \cdot D}{2R}(C_{eq} - C_b)$, Equation (5.20) can be simplified as:

$$\frac{\partial R}{\partial t} = \frac{1}{\rho_r} \cdot \frac{S_h \cdot D}{2R}(C_{eq} - C_b). \tag{5.21}$$

Equation (5.21) shows that the rate of tube enlargement at time t is dependent on the tube profile $R = R(z,t)$. The integration of tube enlargement rate with time produces a the tube radius profile:

$$R(z,t) = \sqrt{\int_0^t \frac{S_h \cdot D}{2\rho_r}(C_{eq} - C_b)dt + R_0^2}, \tag{5.22}$$

where R_0 is the initial tube radius. For time invariant-flow rate Q, as discussed in Section 5.1.4, the bulk concentration C_b is also time-invariant despite the evolution of the tube geometry. By integrating Equation (5.21) with the initial condition $R|_{t=0} = R_0$, the tube radius profile at time t can be expressed as:

$$R(z,t) = \sqrt{\frac{S_h \cdot D(C_{eq} - C_b)}{\rho_r} \cdot t + R_0^2}. \tag{5.23}$$

As shown in Equation (5.23), when the flow rate is a time-invariant, the tube does not enlarge linearly with time. Budek and Szymczak [2012] proposed a similar equation for the radius profile by assuming the Sherwood number $S_h = 4$ for the initially cylindrical and later tapered tube. However, their prediction neglected the high dissolution rate in the entrance region, and uses the same Sherwood number for cylindrical and tapered tubes without formal justification. Equation (5.23) advances their model in two aspects. Firstly, the Sherwood number accounting for the entrance region is used for more accurate bulk concentration calculation and radius prediction. Secondly, the Sherwood number has been proven to be applicable for the tapered tube.

5.1.5 Discussion on the Extended Graetz Solution

Application of the extended Graetz solution

The extended Graetz solution provides an analytical approach to model the transport-controlled dissolution in a tapered tube. With the help of the quasi-steady state approximation, the evolution of the tube can be modeled using the extended Graetz solution as shown with an application to model gypsum dissolution in a preexisting tube.

In the example in Figure 3-10, groundwater flows through multiple ground layers, of which the gypsum layer has preexisting tubes. Since the hydraulic conductivity of a tube is much higher than the other permeable layers, the flow rate in the tube is limited by the other less permeable layers and can be assumed as time-invariant even when the tube is enlarging due to dissolution. The assumption of time-invariant flow rate is simplified compared with what actually happens in the field, but it decouples the effect of the hydrodynamic conditions. In addition, in laboratory conditions, time-invariant flow rate is often used to study the dissolution of rocks [James and Lupton, 1978; Smith et al., 2013].

Assume that groundwater with zero gypsum concentration flows in a preexisting cylindrical tube in gypsum rock, with 0.5m length and 2mm radius. The gypsum has a dry density of $2.0 \times 10^3 [kg/m^2]$ [Einstein et al., 1969] and solubility of 2.6 $[g/L]$ [Raines and Dewers, 1997]. The diffusion coefficient $D = 9.0 \times 10^{-10} [m^2/s]$ is used as the coefficient of the solute [Raines and Dewers, 1997]. The reaction-controlled dissolution rate coefficient $k_r = 8.96 \times 10^{-5} m/s$ [Jeschke et al., 2001] is used to calculate the Damköhler number and to justify that the gypsum dissolution in the example is indeed transport-controlled. The parameters are summarized in Table 5.1.

Table 5.1: Parameters used in the example

Symbol	Value	Unit	Variable
L	0.5	m	Length of the tube
R_0	2.0	mm	Initial tube radius
Q	3.141×10^{-3}	cm^3/s	Flow rate
C_{eq}	2.6	g/L	Solubility (equilibrium concentration)
D	9.0×10^{-10}	m^2/s	Solute diffusion coefficient
k_r	8.96×10^{-5}	m/s	Reaction-controlled dissolution rate coefficient
ρ_r	2.0×10^3	kg/m^3	Density of dry gypsum
ν	1.0×10^{-6}	m^2/s	Kinematic viscosity of water

The dimensionless quantities are calculated to determine the controlling mechanisms in the dissolution process. The Reynolds number ($R_e = 2R_0 v_z \rho/\mu$) for the flow in the tube is 1, indicating that the flow is laminar. The Péclet number ($P_e = 2R_0 v_z/D$) is 1000, indicating that the mass transport is controlled by the diffusion in the radial direction. The Damköhler number ($D_a = R_0 k_r/D$) is 179.2, which indicates that the reaction rate is much higher than the radial diffusion rate and that the dissolution is controlled by diffusion in the radial direction (transport) instead of surface reaction. These dimensionless quantities verify that the extended Graetz solution can be applied to model the dissolution in the gypsum tube.

The timescale for the concentration in the tube to reach steady state can be estimated as: $10\pi R_0^2 L/Q \approx 10^4 s$ or $R^2/D \approx 4 \times 10^5 s$. The timescale for the tube diameter to enlarge 10% can be estimated as: $10\% R/(\frac{\partial R}{\partial t}) \approx 10^8 s$. Hence, the timescale required for the concentration field to reach equilibrium is much shorter than the timescale required for significant alteration of the tube geometry. This comparison shows that the quasi-steady approximation can be used in this example to model the cavity evolution in gypsum.

By applying the quasi-steady state approximation, the bulk concentration $C_b(z)$ can be calculated for the tube using Equation (5.17). The normalized bulk concentration C_b/C_{eq} is plotted against the distance from the inlet z and dimensionless axial coordinate Z. With the assumption of time-invariant flow rate, the radius profiles for $t = 100, 200, 500, 1000 (days)$ can be calculated using Equation (5.23) and are plotted in Figure 5-3(b).

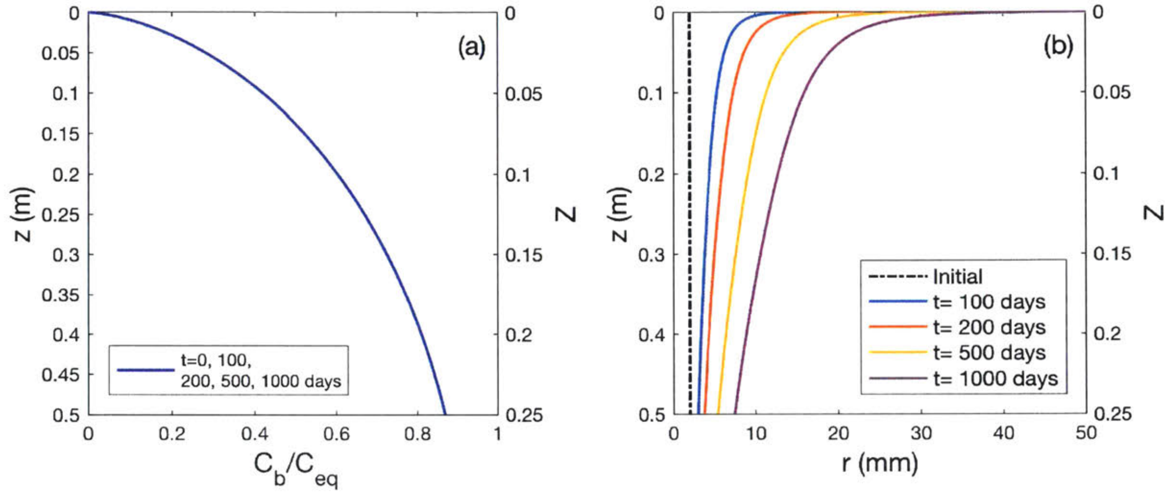

Figure 5-3: Application of the extended Graetz solution to model gypsum dissolution in a preexisting tube. (a) Normalized bulk concentration C_b/C_{eq} along the tube. The quasi-steady state concentration profiles for the initial tube and tapered tubes at $t = 100, 200, 500, 1000 (days)$ are the same. (b) Radius profiles along the tube. The non-uniform dissolution along the tube causes more material to dissolve near the inlet, forming a tapered tube.

Since the flow rate is time-invariant, the dimensionless axial coordinate Z and the concentration profile along the tube are also time-invariant despite the evolving geometry. The calculated concentration profile in Figure 5-3(a) is applicable for $t = 100, 200, 500, 1000 (days)$. The non-uniform dissolution in the tube transforms the initially cylindrical tube into a tapered tube, as shown in Figure 5-3(b). The non-uniform dissolution is caused not only by the concentration difference $(C_{eq} - C_b)$, but also by the higher mass transport rate in the entrance region. This example shows that the extended Graetz solution can be applied to model the dissolution of gypsum in a tube, especially for later stages when the tube is no longer cylindrical.

Numerical validation

The example in discussed above shows how the extended Graetz solution models the evolution of a preexisting tube in gypsum. The example concludes that the quasi-steady state bulk concentration and Sherwood number along the tube are not functions of the tube geometry, but functions of flow rate. A 2-D axisymmetric finite volume model was developed to validate the extended Graetz solution. The model solves the following transient mass conservation equation:

$$\frac{\partial C}{\partial t} = -v_z \cdot \frac{\partial C}{\partial z} - v_r \frac{\partial C}{\partial r} + D \frac{1}{r} \frac{\partial}{\partial r} \left(r \frac{\partial C}{\partial r} \right); \tag{5.24}$$

with the boundary conditions being the same as Equations (5.7) and the initial condition being: $C(z,r)|_{t=0} = C_{eq}$.

The tapered tube with radius profile $R = R(z)$ for $t = 200$ days in Figure 5-3(b) was used as the geometry of the modeled tube. All the other parameters are the same as listed in Table 5.1, except for the radius profile. A structured non-orthogonal finite volume grid was used to discretize the domain as shown in Figure 5-4(a). The fully developed laminar flow described by Equation (5.4) was used in the 2-D model, as shown by the streamlines in Figure 5-4(b). Since the finite volume model uses a non-orthogonal grid, the minimum correction approach was used for non-orthogonal flux correction [Moukalled et al., 2016].

A steady state concentration field was obtained by the model as shown in Figure 5-5(b). The concentration profile is normalized and plotted in $r - z$ coordinates. The solute diffuses from solid-liquid interface to the center of the flow, as the diffusion boundary layer thickens along the tube. The normalized bulk concentration (C_b/C_{eq}) and Sherwood number (S_h) along the tube can be calculated from the concentration profile produced by the 2-D numerical model according to their definitions (Equations (5.2), (5.3)). C_b/C_{eq} and S_h are plotted against the dimensionless axial coordinate Z as defined in Equation (5.18) and can be compared to the extended Graetz solution as shown in Figure 5-5(a).

As discussed in Section 5.1.3, the dimensionless axial coordinate Z is not a function

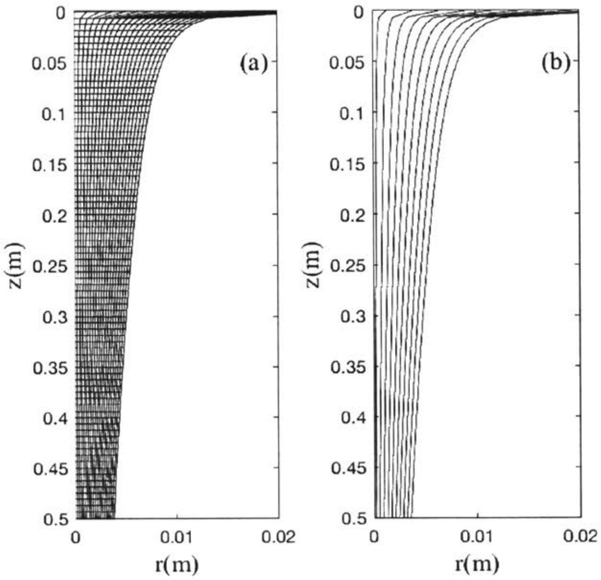

Figure 5-4: 2-D numerical model, (a) The structured non-orthogonal finite volume grid. (b) Streamlines of the flow described in Equation (5.4).

of the tube geometry, but a function of flow rate. Hence, the numerical results have the same dimensionless axial coordinate as in the example in Section 5.1.5. As shown in Figure 5-5, the extended Graetz solution produces the normalized bulk concentration and Sherwood number profile for a tapered tube, which match the numerical simulation. This comparison validates the extended Graetz solution for modeling the transport-controlled dissolution in a tapered tube.

An explanation for the bulk concentration and Sherwood number of a tapered tube being the same as those of a cylindrical tube is proposed as follows: since the flow is laminar, the radial flow near the wall of the tapered tube follows streamlines that are parallel to the tube wall, as shown in Figure 5-6. The diffusion flux is perpendicular to the direction of velocity, which is the same as for a cylindrical tube. The larger tube radius has larger contact-area, however; it has longer diffusion length as counterpart for the dissolution. The overall result is that for the same flow rate, the tapered geometry does not enhance dissolution for the transport-controlled dissolution, so the Sherwood number and bulk concentration do not change with the tube geometry.

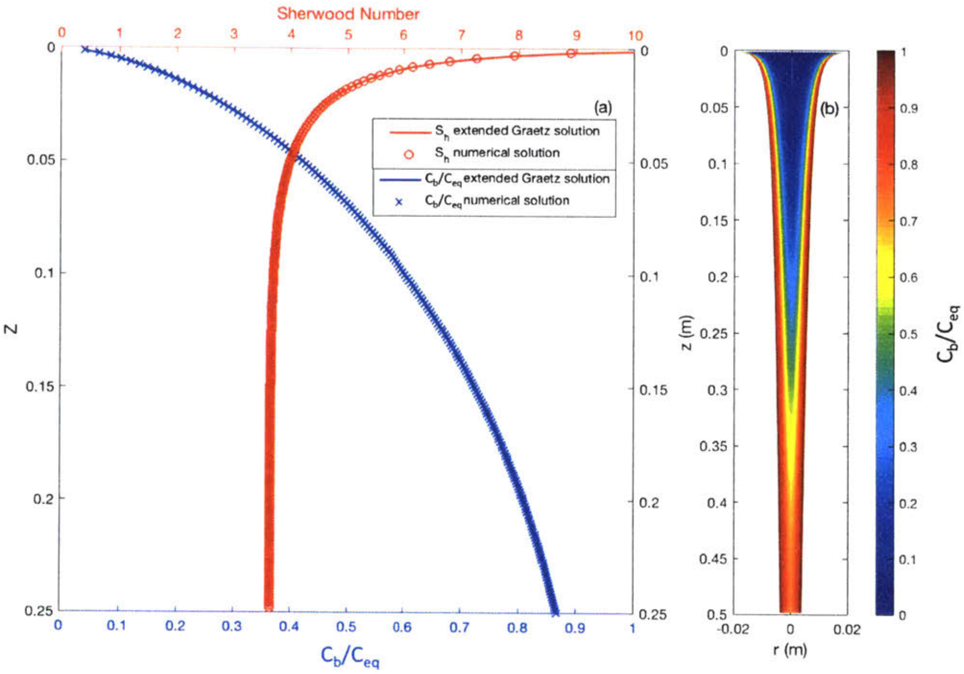

Figure 5-5: Numerical simulation of dissolution in a tapered tube. (a) The normalized bulk concentration C_b/C_{eq} and Sherwood number (S_h) along the tube. C_b and S_h calculated from the numerical simulation matches those produced by the extended Graetz solution; thus the extended Graetz solution is validated. (b) Normalized concentration profile in the tube. Flow with zero concentration (blue) enters the tube from the top, while the solute diffuses from the solid-liquid interface to the center of the flow, similar to the case of a cylindrical tube.

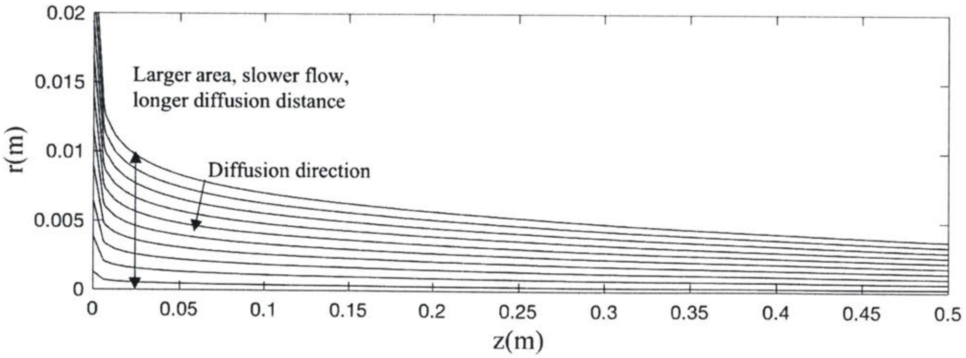

Figure 5-6: A schematic of the flow streamline and diffusion direction.

Comparison to reaction-controlled dissolution in a tube

The above example shows how a preexisting tube evolves due to transport-controlled dissolution: for a time-invariant flow rate, the concentration profile is also time-invariant, while the radius increases non-linearly with time. This behavior is different from the case of reaction-controlled dissolution. It is necessary to make a comparison to differentiate the two with regard to time evolution.

When the reaction rate is much lower than the radial diffusion rate, the dissolution in the tube is reaction-controlled. The Damköhler number of a reaction-controlled dissolution is much smaller than 1, $D_a \ll 1$. Take the example of the dissolution of limestone in carbon dioxide (CO_2) rich water. The reaction-controlled dissolution rate coefficient (k_r) of limestone in CO_2 rich water is: $2 \times 10^{-8} m/s$ [Pokrovsky et al., 2009]. The Damköhler number in this case is 0.04, so the dissolution is reaction-controlled. Assuming the dissolution is a first-order reaction, the dissolution flux can be expressed as:

$$q_w = k_r(C_{eq} - C_b). \tag{5.25}$$

Similar to the formulation of the transport-controlled dissolution, the mass conservation of the solute can be expressed as:

$$Q \cdot \Delta C_b = 2\pi R \Delta z \cdot q_w = 2\pi R \Delta z \cdot k_t(C_{eq} - C_b). \tag{5.26}$$

This equation describes the change of C_b in distance Δz along the tube which is contributed by the reaction-controlled dissolution flux q_w. By taking the limit $\Delta Z \to 0$ and applying $Q = \pi R^2 \bar{v}_z$, the equation can be simplified as:

$$\frac{\partial C}{\partial z} = \frac{2k_r}{\bar{v}_z R}(C_{eq} - C_b). \tag{5.27}$$

The dissolution induced tube enlargement rate can be expressed similar to Equation (5.21):

$$\frac{\partial R}{\partial t} = \frac{k_r}{\rho_r}(C_{eq} - C_b). \tag{5.28}$$

With the help of quasi-steady state approximation, the reaction-controlled dissolution model can be applied with the flow parameters listed in Table 5.1. The normalized bulk concentration profile and radius profile along the tube can be plotted, as shown in Figure 5-7(a) and (b).

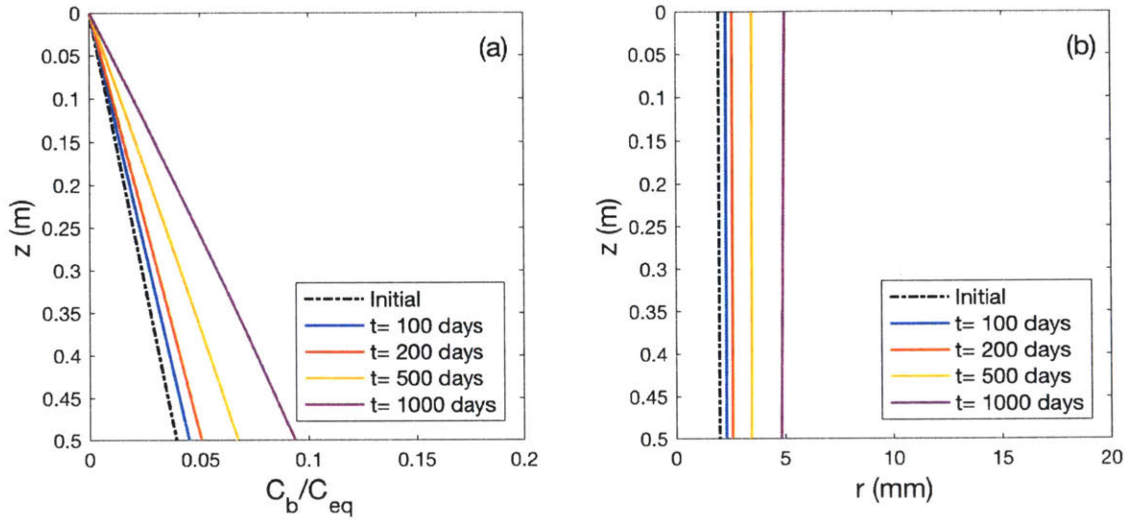

Figure 5-7: Example of reaction-controlled dissolution in a preexisting tube. (a) Normalized bulk concentration C_b/C_{eq} along the tube. Because of the increasing tube radius, the flow velocity decreases for a time-invariant flow rate and the solid-liquid interface area increases. As a result, the concentration profile increases with time. (b) Radius profiles along the tube. With the dissolution rate coefficient k_r being the same along the tube, the non-uniform dissolution is mainly caused by the concentration difference $(C_{eq} - C_b)$, so it is less pronounced than for the case of transport-controlled dissolution.

As shown in Figure 5-7(a), the normalized bulk concentrations along the tube are in the range of 0.03 to 0.1, which are much much lower than the case of transport controlled dissolution shown in Figure 5-3(a). The radius increase in Figure 5-7(b) is also smaller compared with the case of transport-controlled dissolution shown in Figure 5-3(b). This is reasonable given that the reaction-controlled dissolution rate is lower than that of the transport-controlled dissolution rate. The non-uniform dissolution along the tube is less pronounced in Figure 5-7(b) than in Figure 5-3(b). For the reaction-controlled dissolution, the non-uniform dissolution is caused by the concentration difference along the tube only, while for transport-controlled dissolution, the higher dissolution rate in the entrance region also contributes to the non-uniform dissolution.

Apart from the differences regarding the bulk concentrations and radius profiles, the two dissolution models for preexisting tubes differ in the time evolution. The effluent concentrations (bulk concentration at the outlet of the tube $C_b|_{z=0.5}$) are compared for the two cases, as shown in Figure 5-8. For time-invariant flow rate, the transport-controlled dissolution model produces a time-invariant effluent concentration as shown in blue, while the reaction-controlled dissolution model produces an effluent concentration that increases with time, as shown in red.

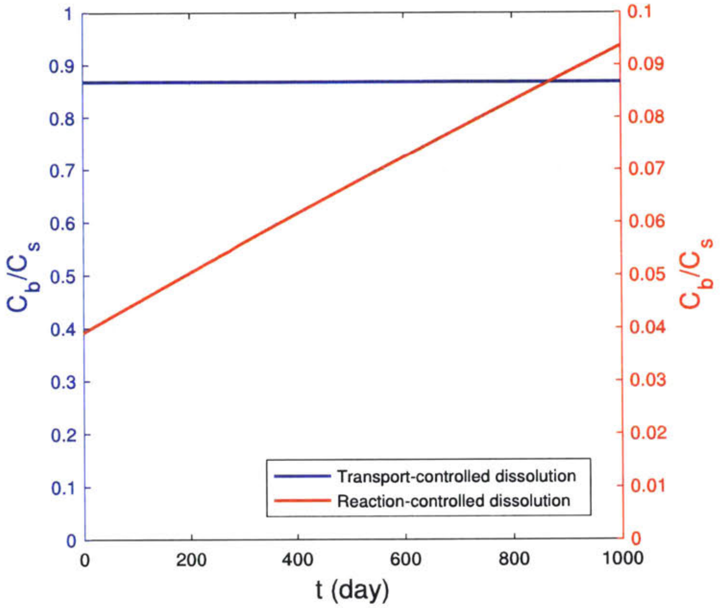

Figure 5-8: Effluent concentrations predicted by the transport-controlled (blue) and reaction-controlled (red) dissolution models. For the time-invariant flow rate condition, the transport-controlled dissolution model produces a time-invariant effluent concentration, while the reaction-controlled dissolution model produces an effluent concentration that increases with time.

The effluent concentration can be used to quantify the overall dissolution rate for the rock-fluid system as discussed in Section 4.1.1, Equation (4.1). The overall dissolution rate for the tube is the total mass dissolved from the tube for a unit time. It indicates how quickly the mass has been removed due to dissolution. For a single tube with time-invariant flow rate, the overall dissolution rate for the transport-controlled dissolution case is time-invariant despite the tube enlargement. However, the tube enlargement enhances the overall dissolution rate for the reaction-controlled dissolution case, as indicated by the red curve in Figure 5-7. The increasing overall dissolution rate for the reaction-controlled dissolution indicates a positive feedback between the tube enlargement and dissolution even when the flow rate is time-invariant.

5.1.6 Experimental Validation of the Extended Graetz Solution

The tube flow tests discussed in Section 4.1 provided good insights into the evolution of the rock-fluid system induced by flow and dissolution in a controlled initial geometry. These tests can also be used as experimental validation of the extended Graetz solution since the hydrodynamic condition and the dissolution kinetics match the assumptions of the extended Graetz solution. More specifically, the extended Graetz solution assumes laminar flow in a tube with gradually changing geometry and transport-controlled dissolution, which matches the experimental conditions. This experimental validation compares the experimental results with the predictions of the extended Graetz solution regarding three aspects: the evolution of the effluent concentration for tube flow tests with time-invariant flow rates, the relation between the effluent concentration and injection flow rate and the geometry of the tubes after the flow tests.

The evolution of the effluent concentration for tube flow tests with time-invariant flow rates

As discussed in Section 5.1.5, when the flow in the tube is time-invariant, the effluent concentration will also be time-invariant despite the evolution of the tube geometry due to dissolution. The four tube flow tests with time-invariant flow rates (Figure 4-1) showed this behavior. During the flow tests, the tubes in the specimens enlarged from 0.7mm to 2-3 mm in diameter and formed a tapered shape (Figure 4-3), as discussed in detail in Section 4.3. Figure 4-1 shows that despite this evolution of the tube geometry during the flow test, the effluent concentration is time-invariant with some noise in each test. This temporal behavior of the effluent concentration is consistent with the prediction of the extended Graetz solution with time-invariant flow rate in the tube, the effluent concentration is also time-invariant despite the geometric evolution of the tube due to dissolution.

Relation between the effluent concentration and the injection flow rate

The effluent concentration C_{eff} as a function of the injection flow rate Q is studied experimentally in Section 4.1. This function is predicted by the extended Graetz solution as:

$$\frac{C_{eff}}{C_{eq}} = f(Z), \tag{5.29}$$

where C_{eq} is the equilibrium concentration of gypsum in water, Z is the dimensionless tube length. Z is defined as:

$$Z = \frac{\pi D}{2Q} L, \tag{5.30}$$

where D is the diffusion coefficient, L is the length of the tube. Equations (5.29) and (5.30) are the dimensionless forms of the effluent concentration and tube length defined in the extendeg Graetz solution. The dimensionless effluent concentration C_{eff}/C_{eq} is a function of the dimensionless tube length Z, which is a function of flow rate Q. Hence the relation between the effluent concentration and flow rate is predicted by the extended Graetz solution. In addition, Equations (5.29) and (5.30) show that the effluent concentration is not a function of the tube radius profile.

The steady state effluent concentrations and the corresponding flow rates in the tube flow tests with flow rate steps (Figure 4-2) are converted to dimensionless form according to Equations (5.29) and (5.30). The data are summarized and plotted in Figure 5-9. The effluent concentration and flow rate of the time-invariant flow rate tests described in Section 4.1.1 were also converted to dimensionless form and plotted in Figure 5-9.

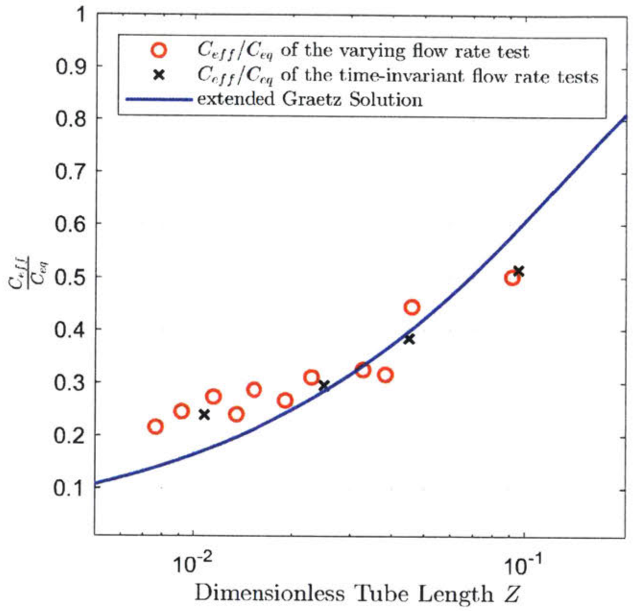

Figure 5-9: Relation between the dimensionless effluent concentration and dimensionless tube length. The prediction made by the extended Graetz solution matches the experimental results reasonably well.

The relation between the dimensionless concentration and dimensionless tube length predicted by the extended Graetz solution is plotted in Figure 5-9 to compare with the experimental results. The experimentally measured results for the tests with varying flow rates and time-invariant flow rates all fall on the prediction of the extended Graetz solution with a small amount of discrepancy.

Geometry of the tubes after the tube flow tests

The extended Graetz solution was used to simulate the radius profiles for each tube after the flow test. Since the specimen length and tube diameter vary from specimen to specimen, a range is provided in the Table 5.2. The material properties used in the simulations are listed in Table 5.2. The durations of tests were also used as input for the model, which were: 52.2, 32.0, 17.3 and 7.6 hours for the four tests with flow rates of 2.5, 5.0, 10.0 and 20.0 L/s, respectively.

As shown in Figure 5-10, the predicted radius profiles match the experimental

Table 5.2: Parameters used to simulate tube geometry

Symbol	Value	Unit	Variable
L	$85 - 99$	mm,	Length of the tube
D_0	$0.65 - 0.75$	mm,	Initial tube diameter
Q	$2.5 - 20$	$\mu L/s$	Flow rate
C_{eq}	2.6	g/L	Solubility (equilibrium concentration)
D	9.0×10^{-10}	m^2/s	Solute diffusion coefficient
ρ_r	1.216	g/cm^3	Density of dry gypsum

results reasonably well regarding the overall tapered shape and the radius away from the inlet. The extended Graetz solution overestimated the radius near the inlet. Here is an explanation for this overestimation: the extended Graetz solution is based on the assumption that the rock-fluid interface is in thermodynamic equilibrium and the dissolution is transport-controlled. This requires the reaction on the rock-fluid interface to have a high rate to keep the interface in thermodynamic equilibrium. The extended Graetz solution predicts a high transport rate coefficient in the entrance region, which might not be realistic since the reaction on the rock-fluid interface has a finite rate and may not be able to keep the interface in thermodynamic equilibrium.

The extended Graetz solution's overestimation of radius near the inlet is less when the flow rate is higher, as shown in Figure 5-10. This is related to the length of the entrance region as a function of the flow rate. As discussed in Section 5.1.1, the entrance region has a dimensionless length of $Z = \frac{\pi D}{2Q} z = 0.1$, which indicates that the physical length of the entrance region is shorter for lower flow rate. The overestimated dissolution is then intensified in the shorter entrance region for the lower flow rate, as shown in Figure 5-10.

As discussed above, the extended Graetz solution was validated from the following three perspectives. Firstly, the evolution of the effluent concentration for tube flow tests with time-invariant flow rates was studied. The effluent concentration being time-invariant despite the evolution of the tube geometry was consistent with the prediction of the extended Graetz solution. Secondly, the relation between the injection flow rate and the effluent concentration was studied. The injection flow rate and effluent concentration were converted into dimensionless form and compared with the

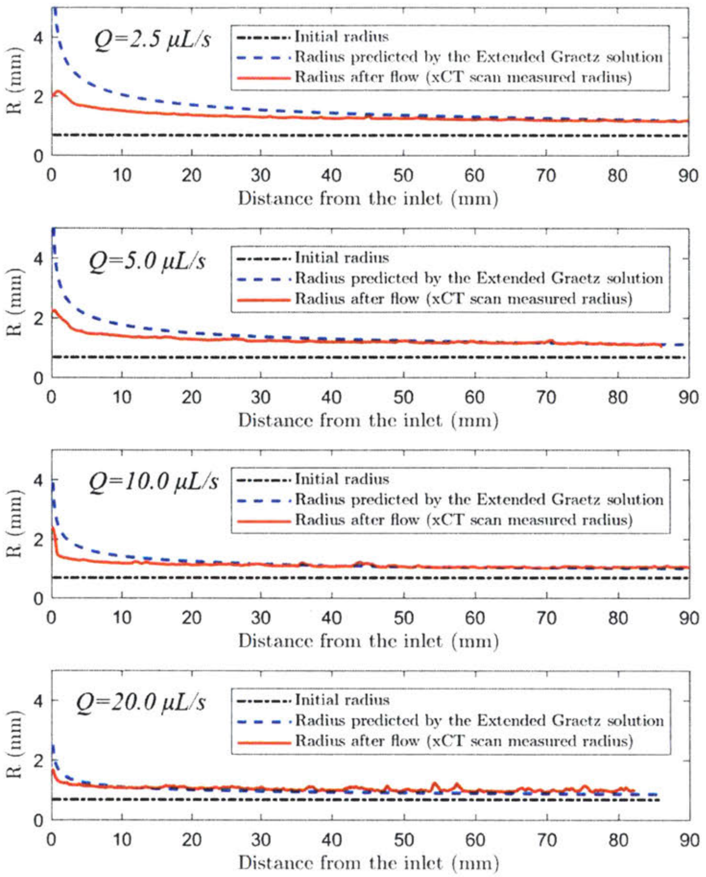

Figure 5-10: Radius profiles of the tube after the flow test. The initial tube radius, the tube radius measured using CT scan and the tube radius predicted using the extended Graetz solution are compared.

relation predicted by the extended Graetz solution. The results matched reasonably well. Lastly, the geometries of the tubes after the flow tests were measured using CT scan and compared with the extended Graetz solution. The radius profile predicted by the extended Graetz solution matched the measured radius profile with good accuracy.

5.1.7 Summary on the Extended Graetz Solution

The extended Graetz solution is a 2-D axisymmetric analytical model developed to study the transport-controlled dissolution in an enlarged tapered tube. The tapered geometry and induced radial velocity were explicitly considered in the governing equations. By adopting the coordinate transform used by Zerkle and Sunderland (1968), the mass conservation equation can be transformed to the same form as the Graetz problem. Thus the Graetz solution can then be extended to simulate the dissolution in a tapered tube. The Sherwood number for a tapered tube is shown to be the same as that of a cylindrical tube. This provides a formal justification for the transport-controlled dissolution model developed by Budek and Szymczak [2012]. An alternative form of the extended Graetz solution (Equations (5.17) and (5.21)) is proposed to take advantage of the invariant variables. This form also recommends to use the Sherwood number as a function of dimensionless axial coordinate Z instead of the asymptotic value, so that the high mass transport rate in the entrance region is considered.

An example is used to show the application of the extended Graetz solution in modeling the geometrical evolution of a preexisting tube in gypsum. With the help of quasi-steady state approximation, the Graetz solution can calculate the concentration and radius profiles for different stages of dissolution. A numerical model is developed to validate the extended Graetz solution by simulating the dissolution in a tapered tube. The extended Graetz solution matches the numerical results very well. An explanation is proposed to rationalize the conclusion that the Sherwood numbers for the cylindrical tube and the tapered tube are the same.

A comparison is made between the transport-controlled and the reaction-controlled dissolution models to show their behavioral difference in time evolution during dissolution: for time-invariant flow rate, the transport-controlled dissolution model produces time-invariant concentration profile, despite the evolving geometry, while the reaction-controlled dissolution model produces increasing concentration profile. Although the discussion and examples are mainly about dissolution of gypsum, the extended Graetz solution is applicable to other materials if the dissolution process is transport-controlled.

The extended Graetz solution was validated experimentally using the results of the tube flow tests. The predictions using the extended Graetz solution, such as the evolution of the effluent concentration for tube flow tests with time-invariant flow rates, the relation between the effluent concentration and injection flow rate and the geometry of the tubes after the flow tests, were compared with the experimental results. Good match were found between the predictions and the experimental results, which validates the extended Graetz solution.

The tube flow tests not only validated the extended Graetz solution, but also provided insights into the evolution of the rock-fluid system with transport-controlled dissolution. When the flow rate is time-invariant in the tube shaped rock cavities, the overall dissolution rate is also time-invariant, which indicates that the mass loss of the soluble layer increases linearly with time, despite the evolution of the tube geometry. This phenomenon can be used to estimate the mass loss over time for the rocks. In addition, the entrance effect causes the non-uniform dissolution in the tube and results in the enlarged tapered inlet geometry. The tapered geometry can be used in the field to interpret the flow direction.

5.2 Dimensional Analysis on Dissolution in Porous Rock Matrix and Wormholes

Section 4.2.3 presented the effluent concentrations measured during the core flood tests, which are useful for studying the overall dissolution rate and the evolution in the rock-fluid system. The overall dissolution rates in the mixed dissolution quasi-steady state and wormhole dissolution quasi-steady state have different power dependence on the flow rates, which reflects the different dissolution kinetics during these two states. This section uses dimensional analysis to study the dissolution kinetics during these two states.

5.2.1 Definition of G and D_{ae}

Dimensional analysis is often used to identify the controlling process during dissolution. As discussed in Section 2.1.2, for laminar flow in tubular geometries, the sequence of the three processes for the solid to dissolve in the flowing fluid is: reaction, diffusion, and advection. The slowest process controls the overall dissolution of the solid. Dimensionless quantities, which are the fraction of one rate to the other rate, can be used to describe the relative magnitude of two rates. A group of two dimensionless quantities is enough to provide a complete description of the dissolution phenomenon [Daccord et al., 1993; Fredd and Fogler, 1998; Detwiler and Rajaram, 2007; Budek and Szymczak, 2012]. Similar to the definitions by Budek and Szymczak [2012], the kinetic parameter G and the effective Damköhler number D_{ae} are defined as:

$$G = \frac{\text{Reaction rate}}{\text{Diffusion rate}}, \tag{5.31a}$$

$$D_{ae} = \frac{\text{Effective dissolution rate}}{\text{Advection rate}}. \tag{5.31b}$$

G measures the extent to which the dissolution rate is hindered by diffusive transport of ions. $G \gg 1$ indicates that the dissolution is diffusion-controlled and that the solid-liquid interface is in equilibrium. $G \ll 1$ indicates that the reaction rate is lower than the diffusion rate and that the dissolution is reaction-controlled. Combining the rates of the first two processes, the reaction and diffusion, the effective dissolution rate coefficient k_{eff} is introduced [Fredd and Fogler, 1998; Detwiler and Rajaram, 2007; Budek and Szymczak, 2012]. The effective dissolution rate coefficient equals the reaction rate coefficient when the dissolution is reaction-controlled, while the effective dissolution rate coefficient equals the transport rate coefficient when the dissolution is transport-controlled. The detailed derivation for the effective dissolution rate is presented in Appendix C.

D_{ae} is the effective Damköhler number relating the effective dissolution rate to the advection rate. $D_{ae} \gg 1$ indicates that the effective dissolution rate is higher than the advection rate, while $D_{ae} \ll 1$ indicates that the effective dissolution rate is lower than the advection rate.

Since the pore space can be represented by connected tubes [Fredd and Fogler, 1998; Budek and Szymczak, 2012; Wang et al., 2016], G and D_{aw} can be defined based on tubular geometries for both the pore space and the tubular shaped wormholes. The detailed derivation for the two dimensionless quantities are presented in Appendix C. The two dimensionless quantities can be expressed as:

$$G = \frac{2Rk_r}{DS_h}, \tag{5.32}$$

$$D_{ae} = \frac{k_{eff}}{\bar{U}}, \tag{5.33}$$

where R is the tube radius; k_r is the reaction-controlled dissolution rate coefficient; D is the diffusion coefficient; S_h is the Sherwood number; k_{eff} is the effective dissolution rate coefficient and $\bar{U}$ is the average flow velocity. From the definition (Equation (5.32)), the kinetic parameter G does not seem to have a direct relation to the flow rate. However, the flow condition affects the value of the Sherwood number, which in turn affects G.

5.2.2 G and D_{ae} for Dissolution in the Pore Space

In order to calculate the kinetic parameter (G_M) and the effective Damköhler number (D_{aeM}) for the matrix flow (subscription "M" indicates the porous matrix), the pore radius and pore flow velocity need to be calculated. The pore radius R_p according to the MIP and CT scan result in Section 3.1.3 is in the order of 1 μm. The average pore flow velocity can be estimated as $\bar{U} = q/n$, where q is the injection flux and n is the porosity. In the core flood test, the injection flux $q = 5.4 \sim 43\ mum/s$ (Section 3.3.2 and the porosity $n = 0.45$ (Section 3.1.3) lead to the average velocity of $1.2 \sim 9.6 \times 10^{-5}\ m/s$. The According to Jeschke et al. [2001], the reaction-controlled dissolution rate coefficient k_r is $7.1 \times 10^{-5} (m/s)$; and the diffusion coefficient D is $9.0 \times 10^{-10} (m^2/s)$ for calcium ions in water. As discussed by Budek and Szymczak [2012] the Sherwood number for a porous medium is relatively high, so the value $S_h = 4$ is used. Thus the transport-controlled dissolution rate coefficient k_t can be calculated as: $k_t = \frac{S_h \cdot D}{2R} = \frac{4 \times 9.0 \times 10^{-10}}{2 \times 10^{-6}}\ m/s = 1.8 \times 10^{-3}\ m/s$. The effective dissolution rate coefficient (k_{eff}) is then calculated based on Equation (C.5). This results in the dimensionless quantities for the matrix flow:

$$G_M = \frac{2Rk_r}{DS_h} = \frac{2 \times 10^{-6} \times 7.1 \times 10^{-5}}{9 \times 10^{-10} \times 4} = 0.04, \tag{5.34}$$

$$D_{aeM} = \frac{k_{eff}}{\bar{U}} = \frac{7.1 \times 10^{-5}}{1.2 \sim 9.6 \times 10^{-5}} = 0.74 \sim 5.92. \tag{5.35}$$

In the pore space, the diffusion distance is short across the pore diameter, so the diffusion process is relatively fast, as indicated by G_M being less than one. Therefore, dissolution in the porous medium is reaction-controlled. The effective Damköhler number is related to the flow rate and ranges from 0.74 to 5.92 in the core flood tests. Since the flow is not uniformly distributed due to the initial heterogeneity of the matrix, the average flow velocity usually underestimates the velocity of the major pore flow. With higher velocity in the major pore flow, the effective Damköhler number should be less than one according to the definition (Equation (5.33)). Therefore, the effective dissolution rate is lower than the advection rate. Given that the reaction in the pores is slower than both diffusion and advection, the dissolution in the pore space is reaction-controlled.

5.2.3 G and D_{ae} for Dissolution in the Wormholes

The kinetic parameter (G_T) and the effective Damköhler number (D_{aeT}) for the tube flow in the wormholes (subscription "T" indicates the wormholes) can be calculated with the data from the CT scan. According to the CT reconstruction in Section 4.2.5, the radius of the major wormhole R_t is in the order of 0.5mm. Thus the transport-controlled dissolution rate coefficient k_t can be calculated as: $k_t = \frac{S_h \cdot D}{2R} = \frac{4 \times 9.0 \times 10^{-10}}{5 \times 10^{-4}}\ m/s = 7.2 \times 10^{-6}\ m/s$. The effective dissolution rate coefficient (k_{eff}) is then close to the transport-controlled dissolution rate coefficient (k_t) since it is much less. Since the injected flow is localized in the one wormhole connecting the inlet and outlet, the average flow velocity can be estimated as $\bar{U} = Q/(\pi R_t^2) =$

$6.4 \sim 50.9 \times 10^{-3}$ m/s, where Q is the injection flow rate. The estimated Similar to the calculation of dimensionless quantities for the dissolution in the pore space, the dimensionless quantities for the dissolution in the wormholes can be calculated:

$$
\begin{aligned}
G_T &= \frac{2Rk_r}{DS_h} = \frac{2 \times 0.5 \times 10^{-3} \times 7.1 \times 10^{-5}}{9 \times 10^{-10} \times 4} = 19.72, && (5.36)\\
D_{aeT} &= \frac{k_{eff}}{\bar{U}} = \frac{7.2 \times 10^{-6}}{6.3 \sim 50.9 \times 10^{-3}} = 1.4 \times 10^{-4} \sim 11.4 \times 10^{-4}. && (5.37)
\end{aligned}
$$

The wormhole diameter is two to three orders of magnitude larger than the pores, which results in a longer diffusion distance and relatively slow diffusion. The dissolution in the wormholes is diffusion-controlled, as indicated by G_T being greater than one. The range of the effective Damköhler number indicates that the effective dissolution rate is much lower than the advection rate. Given that the diffusion in the wormholes is slower than both reaction and advection, the dissolution in the wormholes is diffusion-controlled.

5.2.4 Summary on the Dimensional Analysis

The dimensional analysis shows that the dissolution mechanisms in the pore space and the wormhole are different. In both cases, the injection results in a fast advection process, so advection is not a controlling mechanism for dissolution. In the pore space, the diffusion distance is short across the pore diameter, so the diffusion process is relatively fast. The dissolution in the pore space is reaction-controlled. On the contrary, wormhole diameter is three orders of magnitude larger, which results in a longer diffusion distance and relatively slow diffusion. Thus the dissolution in the wormholes is diffusion-controlled.

The study of dissolution mechanisms in the pore space and the wormholes also shed light on the evolution of the overall dissolution kinetics of the rock-fluid systems. During the core flood tests, the enlarging of the wormholes and redistribution of flow in the wormholes cause an evolution of the overall dissolution kinetics. More specifically, in the initial state of the system, the rock-fluid system only contains matrix flow and reaction-controlled dissolution. In the mixed dissolution quasi-steady state, part of the specimen has tube flow because of the wormholes, while part of the specimen still has matrix flow. Reaction-controlled dissolution and diffusion-controlled dissolution coexist in the rock-fluid system before the breakthrough of the wormholes. In the wormhole dissolution quasi-steady state, the flow is localized in the wormholes so the dissolution in the rock-fluid system is diffusion-controlled.

5.3 Dissolution in Wormholed Porous Media

In this section, a continuum model is developed to simulate the dissolution in the rock matrix. A new relation between the effective surface area and the flow rate is proposed, based on the wormhole geometry analysis and parallel tube modeling. For the dissolution in the wormholes, the extended Graetz solution is used to simulate the dissolution process in the evolving wormholes. Combining the continuum model and the extended Graetz solution, a model for core flood test (MCFT) is developed to simulate the flow and dissolution in the specimens during core flood tests. MCFT simulates the wormhole formation, wormhole breakthrough, and the evolution of the dissolution kinetics in the rock-fluid system, which match the core flood test result reasonably well.

5.3.1 Dissolution in the Rock Matrix

Flow and dissolution in the porous rock matrix are usually simulated using continuum models [Carroll et al., 2013; Fu et al., 2015]. In these continuum models, a representative elementary volume (REV) is defined for the rock matrix and pore fluid, so that averaged parameters such as Darcy velocity and concentration can be used for the REV. In the first two states of core flood tests, the flow and dissolution in the porous matrix can be modeled using a continuum model.

Governing equation

A representative elementary volume (REV) is used to analyze the flow and dissolution in the gypsum matrix, as shown in Figure 5-11. Assuming the flow is unidirectional in the z direction as in the core flood tests, the injection flux q_{in} is the injection rate Q normalized by the cross-sectional area of the specimen, which is also known as the Darcy velocity. The REV has the dimensions of ΔX, ΔY, and ΔZ. The fluid enters the REV with a gypsum concentration of C_{in} and exits the REV with a concentration of C_{out} due to dissolution in the REV.

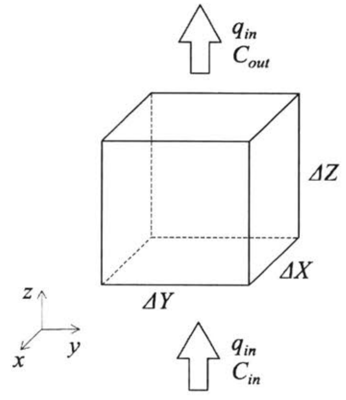

Figure 5-11: A representative elementary volume of the porous rock matrix.

As discussed in Appendix C, the dissolution mass flux of gypsum R_{eff} $[M/(L^2 \cdot T)]$ can be expressed as:

$$R_{eff} = k_{eff}(C_{eq} - C_b), \tag{5.38}$$

where C_{eq} is the equilibrium concentration (solubility); C_b is the bulk concentration. As discussed in Section 5.2, the diffusion in the pores is relatively fast, so the concentration in each pore is relatively uniform and can be used as the bulk concentration. In the REV, the mass conservation of the solute gypsum can be expressed as:

$$q_{in} \Delta X \Delta Y \Delta C = A_{REV} \cdot k_{eff}(C_{eq} - C_b), \tag{5.39}$$

where $\Delta C = (C_{out} - C_{in})$; A_{REV} is the total area in the REV that is reactive with the pore fluid and contributing to the dissolution flux. Equation (5.39) described the change of solute concentration in the fluid after flowing through the REV, which is contributed by dissolution. Equation (5.39) can be normalized by the volume of the REV ($\Delta X \Delta Y \Delta Z$), which yields:

$$q_{in} \cdot \frac{\Delta C_b}{\Delta z} = A_e \cdot k_{eff}(C_{eq} - C_b). \tag{5.40}$$

After taking the limit: $\Delta Z \rightarrow 0$, this equation becomes:

$$q_{in} \cdot \frac{\partial C_b}{\partial z} = A_e \cdot k_{eff}(C_{eq} - C_b). \tag{5.41}$$

$A_e[L^{-1}]$ is the effective surface area, which is the normalized A_{REV}:

$$A_e = \frac{A_{REV}}{\Delta X \Delta Y \Delta Z}. \tag{5.42}$$

A_e represents the total area in a unit volume of REV that is reactive with the pore fluid and contributing to the dissolution flux. Equation (5.41) is the governing equation for simulating the dissolution in the rock matrix using a continuum model. This formulation has been used in many theoretical studies with variations in the estimation of effective surface area A_e, which will be discussed in detail in the following section.

Effective surface area A_e

The key parameter in the governing equation (Equation (5.41)) is the effective surface area A_e. It should be differentiated from the specific area, which is the total pore area in a unit volume (or mass) of rock. The effective surface area is not only determined by the pore structure, but also by the chemical reactions and flow conditions [Guo et al., 2015, 2016; Soulaine et al., 2017]. The effective surface area has been estimated using core flood tests, in which the chosen flow rates are relatively high and usually kept constant for a set of tests [Noiriel et al., 2009]. These studies assume that the effective surface area A_e is constant under different flow conditions. However, this assumption is not necessarily correct, as discussed by Soulaine et al. [2017]; Wen and Li [2017], who studied numerically the effect of flow rate on the effective surface area.

Since the wormholes are the result of flow and dissolution heterogeneities in the porous matrix, the wormhole geometries resulting from different flow rates can be used to evaluate the effect of flow rate on the dissolution in the porous matrix. According to the experimental observations (Section 4.2.5), higher flow rates result in more wormholes and branches in the rock matrix, which indicates that higher flow rates force the fluid to react in more pores in the matrix. The higher number of wormholes and branches developed near the inlet of the specimen in turn distribute flow more uniformly into the porous matrix. This also implies the concept that higher flow rate results in larger effective surface area (A_e).

The quantitative wormhole geometry analysis of the CT data can be used to further explore this concept. The CT data analysis (Section 4.2.5) showed that the number of wormholes N_{wh} is proportional to the 0.42 power of the flux q; the number of branches is proportional to the 0.25 power of the flux q; and the tortuosity is proportional to the 0.05 power of the flux q. Since the wormholes reflect flow and dissolution occurring in the matrix, it is reasonable to propose that the reactive surface area is proportional to the (0.42+0.25+0.05=0.72) power of the injection flux q:

$$A_e \propto q^{0.72}. \tag{5.43}$$

Equation (5.43) proposes a relation between the effective surface area A_e and the injection flux q based on the wormhole geometries. This relation indicates that higher flux in the matrix activates more pore surface to react with the pore fluid. This relation is based on limited experimental data and is likely to be valid only in the range of injection flux similar to the core flood tests. It will be validated using parallel tube modeling (Appendix D) and the model for core flood tests in Section 5.3.3.

5.3.2 Dissolution in the Wormholes

The effluent concentration and dimensional analyses have shown that the dissolution in the wormholes is diffusion-controlled. In the wormhole dissolution quasi-steady state of a core flood test, the flow was pipe flow localized in the major wormholes, which is in the validity domain of the extended Graetz solution. The extended Graetz solution is used to model the effluent concentration in the wormhole dissolution quasi-steady state.

The extended Graetz solution models the diffusion-controlled dissolution in an evolving tapered tube. The Sherwood number accounting for the entrance region and the tapered geometry is used in the extended Graetz solution. More specifically for constant flow rate, the extended Graetz solution predicts that the effluent concentration will be constant despite the evolution of the wormhole geometry. This prediction is consistent with the observation that the effluent concentration in the wormhole dissolution quasi-steady state (WDSS-C_{eff}) is constant, as shown in Figure 4-9.

Since there are several tests with different flow rates, the WDSS-C_{eff} as a function of flow rate can also be compared with the prediction of the extended Graetz solution. As discussed in Section 5.1.6, the normalized effluent concentration (C_{eff}/C_{eq}) is a function of the dimensionless length of the tube (L_{dless}), which is defined as:

$$L_{dless} = \frac{\pi D}{2Q} \cdot L_{wormhole}, \tag{5.44}$$

where D is the diffusion coefficient; Q is the flow rate in the wormhole, $L_{wormhole}$ is the length of the wormhole, which is calculated using the CT scan data (Section 4.2.5). As shown in Equation (5.44), apart from the constants, the dimensionless length is determined by the length of the wormhole and the flow rate Q in the wormhole. The dissolution induced enlargement of the wormhole does not affect the dimensionless length of the wormholes. Therefore, the effluent concentration is constant, despite the evolution of wormhole geometry.

In Figure 5-12, the normalized effluent concentration is plotted as a function of the dimensionless length and compared with the extended Graetz solution. The comparison shows that the effluent concentration predicted by the extended Graetz solution matches the WDSS-C_{eff} from the core flood tests.

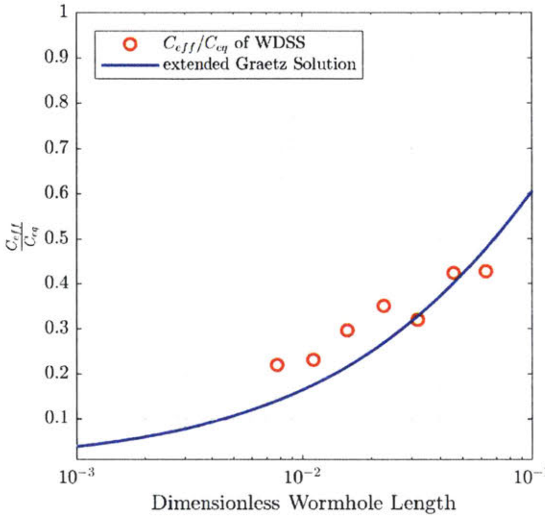

Figure 5-12: Measured wormhole dissolution effluent concentration compared with the effluent concentration predicted by the extended Graetz solution.

The above analysis shows that despite the complex evolving geometry of the wormholes, the dissolution kinetics is relatively simple and can be modeled using the extended Graetz solution. The extended Graetz solution can predict not only the behavior of the effluent concentration but also its quasi-steady state values resulting from different flow rates.

5.3.3 A Model for Core Flood Tests

Sections 5.3.1 and 5.3.2 show that the flow and dissolution in the porous matrix can be modeled using the continuum model (Equation (5.41)), while the flow and dissolution in the wormholes can be modeled using the extended Graetz solution. A conceptual model proposed by Daccrod et al. [1993b] is used here to predict the formation of wormholes. These three models are combined as a model for core flood tests (MCFT) to simulate the evolution of the dissolution kinetics in the rock-fluid system during core flood tests.

More sepcifically, the conceptual model proposed by Daccrod et al. [1993b] divided the specimen into the wormhole section with length L_w and the matrix section with length L_m, as shown in Figure 5-13. This model assumes that the wormhole section has infinite permeability, while the matrix section has the permeability of the intact porous matrix. With this assumption, the lengths of the two sections (L_w and L_m) can be predicted based on the pressure data measured during the core flood tests. Therefore, the core flood tests can be modeled by combining the extended Graetz solution with the length of L_w and the continuum model with the length of L_m.

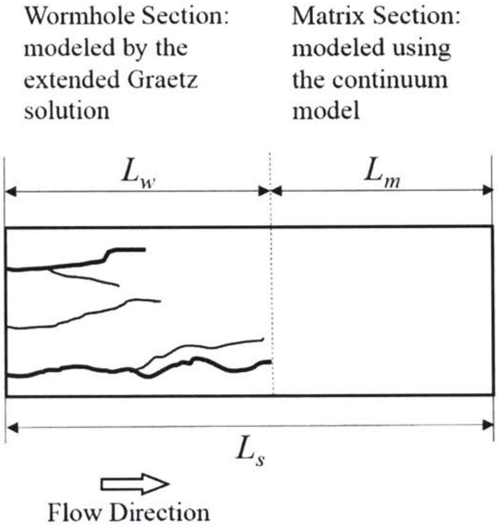

Figure 5-13: Schematic of the model for core flood tests based on the conceptual model by Daccrod et al. [1993b]. The wormhole section is modeled using the extended Graetz solution. The matrix section is modeled using the continuum model.

Based on the pressure data, the length of the wormhole section increases linearly with the injected pore volume (V_p) before the wormhole breakthrough ($V_p < V_{pbt}$) (Section 4.2.2). The rate of increase is a function of the injection flux (q) (Figure 4-7). After the wormhole breakthrough ($V_p \geq V_{pbt}$), the wormhole section has the same length as the specimen. The length of the wormhole section is predicted as:

$$L_w = \begin{cases} L_s \cdot V_p(0.996q^{-0.419}), & for \quad V_p < V_{pbt} \\ L_s, \quad for \quad V_p \geq V_{pbt}; \end{cases} \tag{5.45}$$

where L_s is the specimen length, V_p is the injected pore volume, and V_{pbt} is the breakthrough pore volume. In the wormhole section, there are several wormholes developed from the inlet, the number of wormholes N_{wh} can be predicted using the empirical relation summarized in Section 4.2.6:

$$N_{wh} = A_s \cdot N_{whN} = A_s \cdot 0.42 \cdot q^{0.42}, \tag{5.46}$$

where $A_s[cm^2]$ is the inlet area; N_{whN} is the number of wormholes per unit inlet area; and q is the injection flux. Given the tortuous nature of the wormholes, the lengths of the wormholes are slightly longer than the wormhole section. Therefore, when using the extended Graetz solution, the wormhole length L_{wh} is calculated:

$$L_{wh} = L_w \cdot \tau; \tag{5.47}$$

where τ is the tortuosity of the wormholes. τ, can be predicted using the empirical relation summarized in Section 4.2.6:

$$\tau = 1.14q^{0.05}. \tag{5.48}$$

Therefore, the dissolution in the wormhole section can be modeled as dissolution in N_{wh} wormholes with lengths of L_{wh}. The flow in the wormhole section is assumed to be distributed evenly in the N_{wh} wormholes, before the wormhole breakthrough. The concentration at the end of the wormhole section C_{wh} is calculated using the extended Graetz solution in each wormhole. After the wormhole breakthrough, the flow concentrates in the major wormhole, for which the effluent concentration has already been modeled in Section 5.3.2.

The dissolution in the porous matrix section is modeled using the governing equation (Equation (5.41)). The concentration C_{wh} from the wormhole section is the boundary condition for the dissolution in the matrix section. Thus the governing equation for the matrix section is:

$$q_{in} \cdot \frac{\partial C_b}{\partial z} = A_e \cdot k_{eff}(C_{eq} - C_b) \;\; (0 < z \leq L_m) \tag{5.49a}$$

$$C_b = C_{wh} \;\; (z = 0). \tag{5.49b}$$

Both the assumptions of a constant effective surface area and an effective surface area as a function of injection flux ($A_e \propto q^{0.72}$) are used in the continuum model to simulate the effluent concentration. More specifically, the constant effective surface area assumption uses the value $4.0 \times 10^{-2}\,(cm^{-1})$ for A_e to obtain a good fit to the result. In comparison, the function $A_e = 0.4q^{0.72}\,(cm^{-1})$ is used for the proposed relation in Section 5.3.1. The parameters listed in Table 5.3 are used in the model for core flood tests. The predicted effluent concentration is compared with the test results as shown in Figure 5-14.

Table 5.3: Parameters used in the model for core flood tests

Symbol	Value	Unit	Variable
A_s	9.10	cm^2	Specimen inlet area
C_{eq}	2.6	g/L	Solubility of gypsum in distilled water
D	9.0×10^{-6}	cm^2/s	diffusion coefficient
k_t	7.1×10^{-3}	cm/s	Reaction-controlled dissolution rate coefficient
L_s	8.50	cm	Specimen length
n	$0.46 - 0.48$	1	Porosity
q	$5.5 - 44$	$\mu m/s$	Injection flux

The model for core flood tests (MCFT) predicts the effluent concentrations that have similar trend to the effluent concentration data measured in the tests. The effluent concentration was high before the wormhole breakthrough and low after. The sudden drops in the effluent concentration was caused by the wormhole breakthrough, which concentrated almost all the flow in the one major wormhole. This sudden drop was predicted reasonably well based on the empirical relations (Equation (5.45)). The small difference in the predicted breakthrough pore volumes and the test results are the results of the difference between the power law fitting and the test data in Section 4.2.2.

Before the wormhole breakthrough, the effluent concentration is modeled using the extended Graetz solution and the continuum model (Figure 5-13). With the assumption of constant effective surface area A_e, the model overestimates the effluent concentration when flow rates are low and underestimates the effluent concentration when the flow rates are high. In comparison, with the proposed relation ($A_e \propto q^{0.72}$), the model produced a more accurate effluent concentration. After the wormhole breakthrough, the effluent concentration is predicted by the extended Graetz solution only, since the length of the matrix section is zero. The effluent concentrations predicted by this model match the test result very well, which has been discussed in Section 5.3.2.

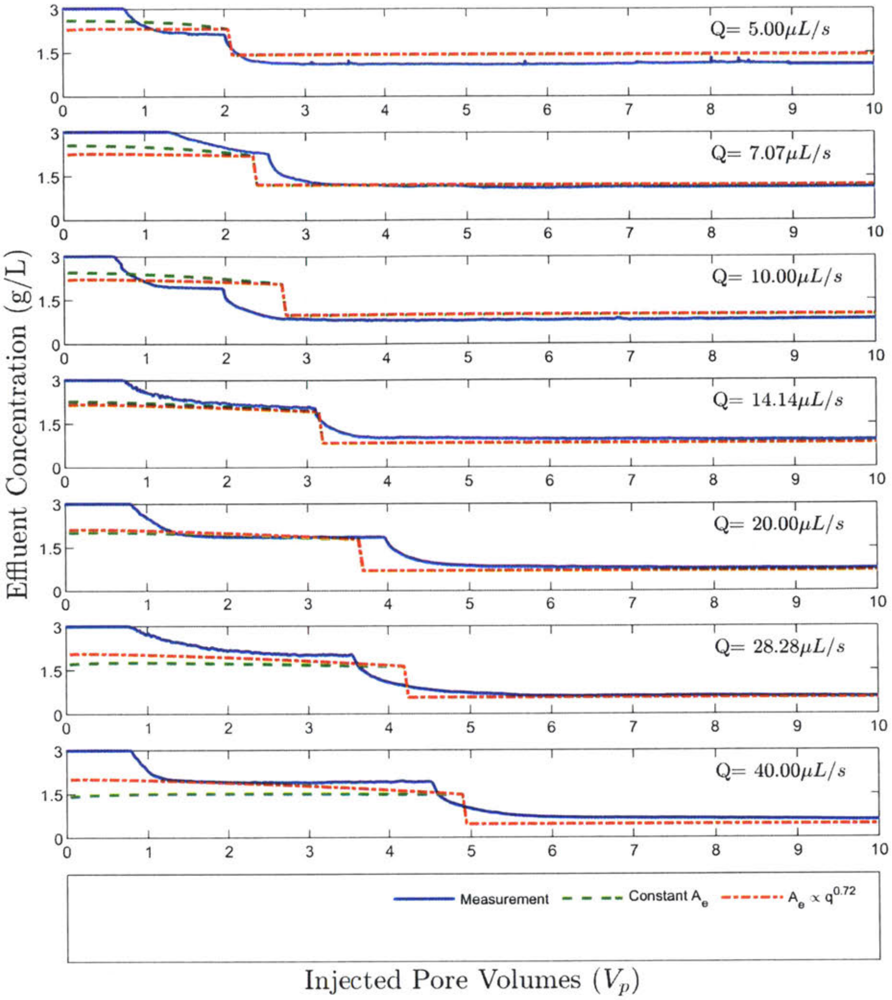

Figure 5-14: Comparison on the effluent concentrations. The effluent concentration predicted by MCFT with constant effective surface area assumption, MCFT with proposed relation $A_e = 0.4q^{0.72}\,(cm^{-1})$ and measured in the core flood tests are compared. The two predicted effluent concentrations match the overall behavior of the measurements in the core flood tests. MCFT with the assumption $A_e = 0.4q^{0.72}\,(cm^{-1})$ provides a prediction that better matches the test results, because it accounts for the effect of flow rate on the effective surface area.

MCFT does not represent the detailed flow and dissolution in the pores and wormholes, however, it provides a simple and fast simulation of the evolution of the rock-fluid system regarding the wormhole formation, wormhole breakthrough, and dissolution kinetics. By dividing the specimen into the wormhole section and the matrix section, this model accommodates application of kinetic models such as the extended Graetz solution and the continuum model. The proposed relation between effective surface area (A_e) and the flux are also validated using MCFT. This could also be extended to other rock-fluid systems with experimental calibration.

5.3.4 Summary on the Dissolution in Wormholed Porous Media

The dissolution in the matrix was modeled using a continuum model. The key parameter in this model, the effective surface area A_e, was discussed, since it was not only determined by the pore structure but also the chemical reactions and flow conditions. A relation between the effective surface area and the injection flux was proposed based on the CT scan analysis and parallel tube modeling. The dissolution in the wormholes was modeled using the extended Graetz solution. After the wormhole breakthrough, the flow was concentrated in the wormholes, and the effluent concentration could be directly predicted using the extended Graetz solution.

The conceptual model proposed by Daccord et al. [1993] was used as a simplified representation for the specimen with wormholes. The specimen was divided into the wormhole section, in which the dissolution was modeled using the extended Graetz solution, and the matrix section, in which the dissolution was modeled using the continuum model. The length of each section was predicted using the empirical equation for wormhole growth rate, as discussed in Section 4.2.2. This combination of the dissolution models and the empirical model resulted in the model for core flood tests (MCFT). This model was able to simulate the wormhole formation, wormhole breakthrough, and the evolution of dissolution kinetics in the rock-fluid system during the core flood tests.

This section proposed a relation between the effective surface area and flow rate (injection flux) based on the CT scan and parallel tube modeling, in order to account for the flow condition when estimating the effective surface area. Even with the somewhat limited number of tests and effluent concentration data, the relation between the effective surface area and flow rate predicted the dissolution kinetics for the gypsum-water system reasonably well. Similar relations between the effective surface area and flow rate should also be expected for other rock-fluid systems. Given the relatively simple reaction of gypsum dissolution in water, this study can be used as a reference for future studies of matrix dissolution and wormhole formation.

Chapter 6

Summary and Conclusions

6.1 Research Summary

Reactive transport processes involve fluid flow and reactions (dissolution, precipitation, and pressure solution) driving the evolution of the rock-fluid systems, which may result in favorable processes such as increased oil production by reservoir acid stimulation, or undesired processes such as ground subsidence or CO_2 reservoir caprock leakage. The flow and reaction in the rock matrix often induce wormholes, which are the long, finger-like channels that form due to the dissolution heterogeneity in the matrix. These wormholes become major flow pathways, which greatly increase the permeability of the rock. At longer time scales, the reactive transport processes further transform the wormholes into larger caves and sinkholes, which become geohazards for human activities. To study the reactive transport processes in the underground rock-fluid systems, new experimental methods and theoretical models have been developed. The new methods and models provided fundamental understanding of the reactive transport processes and accurate predictions of the evolution of the rock-fluid systems.

More specifically, an effluent chemistry monitoring system (ECMS) was designed and integrated into a triaxial system to provide continuous effluent concentration measurements during the tube flow tests and core flood tests. The continuous effluent concentration data were then used to study the overall dissolution rate and the evolution of dissolution kinetics in the rock-fluid system. 3D topological and morphological algorithms were developed to quantitatively analyze the CT data and study the geometry of the tube and wormholes after the tube flow tests and core flood tests, respectively. These 3D algorithms can be used to quantitatively compare the tubes resulting from different flow rates and quantify the effect of flow rate on the complexity of the wormholes.

Tube flow tests were conducted on laboratory cast gypsum specimens each with a preexisting cylindrical hole to study the evolution of the hole geometry and dissolution kinetics. The cylindrical hole was used as simplified geometry for rock cavities in general (fractures and wormholes). The study of dissolution in a cylindrical tube is an initial step towards the better understanding of the dissolution in underground rock-fluid systems. With the controlled material property, initial geometry and flow rates, the effect of dissolution on the evolution of the rock-fluid system can be studied. As discussed in Section 4.1, the effluent concentration is time-invariant after the initial transient state despite the tube enlargement from 0.65-0.75 mm to 1-2 mm. This indicates that the overall dissolution rate in the rock-fluid system is also time-invariant and that the evolution of the tube geometry does not affect the overall dissolution kinetics. The relation between effluent concentration and injection flow rate is also studied using these experimental methods. In addition, the tube flow tests are the basis for the development of an analytical model, the extended Graetz solution as further discussed below. They provided experimental validation for the analytical solution regarding: the evolution of the effluent concentration for tube flow tests with time-invariant flow rates, the relation between the effluent concentration and injection flow rate, and the geometry of the tubes after the flow tests.

Core flood tests were conducted to study the effect of flow rate on the dissolution of gypsum rock matrix and the formation of wormholes. The ECMS and quantitative wormhole geometry analyses provided new perspectives for the current studies regarding the dissolution kinetics and wormhole geometries. Based on the continuous effluent concentration data, the gypsum-water system in the core flood tests went through four states: initial transient state, mixed dissolution quasi-steady state, breakthrough transient state and wormhole dissolution quasi-steady state. A sudden effluent concentration drop was observed at wormhole breakthrough, which indicated that the wormhole breakthrough concentrates almost all of the flow in the major wormhole and in turn changed the dissolution kinetics. The CT analyses quantified the complex geometries of the wormholes, and compared the wormholes resulting from different flow rates using the quantitative parameters such as the number of wormholes and branches. The use of laboratory cast gypsum specimens facilitated the systematic study of the effect of flow rate on the dissolution of the gypsum rock matrix and the formation of wormholes. Given the consistent properties of the gypsum specimen and its relatively simple reaction with water, this experimental study can be used as an analog and a reference for more complex rock-water systems, for example, a calcite-HCl system. The innovations of the experimental methods, especially the ECMS, can also be calibrated to study other rock-fluid systems and the dissolution in rock fractures.

In the theoretical study, the flow and dissolution in a preexisting cylindrical hole in gypsum were studied first. A 2-D axisymmetric analytical model, the extended Graetz solution, was developed to study the transport-controlled dissolution in an enlarged tapered tube. The tapered geometry and induced radial velocity were explicitly considered in the governing equations. The extended Graetz solution showed that the Sherwood number for a tapered tube is the same as that of a cylindrical tube. The extended Graetz solution was validated numerically with finite volume method and experimentally with the tube flow tests as mentioned earlier. The extended Graetz solution, with the quasi-steady state approximation, predicted the the effluent concentration and the tube geometry.

To study the dissolution in the porous rock matrix and the formation of wormholes, dimensional analysis was used to study the controlling mechanisms of dissolution in the matrix and the wormholes. According to the dimensional analysis, the dissolution in the matrix was reaction-controlled, while the dissolution in the wormholes was diffusion-controlled. A continuum model was developed to simulate the dissolution in the rock matrix. For the continuum model, this study developed a relation between effective surface area and flow rate (injection flux) based on the experimental study of the wormholes to account for the flow conditions when estimating the effective surface area. Finally, a model for core flood tests combining the continuum model and the extended Graetz solution was developed to simulate the development of the wormholes, wormhole breakthrough, and the evolution of dissolution kinetics induced by wormhole formation.

In sum, this research used advanced experimental methods and new analytical models to obtain the fundamental understanding of the reactive transport processes and make accurate predictions of the evolution of the rock-fluid systems driven by the reactive transport processes.

6.2 Practical Insights

The experimental and theoretical studies provided the fundamental understanding of the reactive transport processes. The models developed in this study could predict and match the experimental results very well. These studies also provided practical insights into civil, environmental and energy applications. For example, the extended Graetz solution and tube flow tests can be used to estimate the overall dissolution rate when groundwater flows through a soluble layer. The core flood tests with gypsum can be used as analog tests for other rock-fluid systems such as limestone-HCl systems, and carbonate rock-CO_2-water systems.

As discussed in Section 2.6.1, the groundwater flow and rock dissolution induce the formation of karst. Karst poses a potential threat to the structures on the surface and in the subsurface, such as building foundations, dams, and tunnels. The extended Graetz solution can be used to predict the evolution of the underground cavities including karst as shown in the example in Section 5.1.5. In the example, the flow rate in the cavity is assumed to be time-invariant. This assumption is not a necessary condition for the application of the extended Graetz solution. As shown in Equation (5.17), apart from the material constants, the overall dissolution caused by the groundwater flow is related to the length of the tubular cavity and flow rate.

The diameter of the tubular cavity does not affect the calculation, while length of the cavity can be measured using tracer tests. Therefore, the overall dissolution rate can be estimated for a given flow rate. Thus the evolution of a cavity regarding the mass and volume loss over time can be estimated for site studies and risk evaluation.

The core flood tests, with gypsum-water system as an analog system, can be used to study the wormhole formation during oil reservoir acid stimulation. For example, the four states during the core flood tests (Section 4.2.3) can also be used to characterize the stages during an acid stimulation operation in the oil field. As discussed, the overall dissolution rate is higher before the wormhole breakthrough, and lower after the wormhole breakthrough. With higher flow rates, the effluent concentration is lower. The dependence of effluent concentration on the flow rate makes the overall dissolution rate, the product of the flow rate and effluent concentration, higher. Also, the flow rate affects the breakthrough volume and the geometric complexity of wormholes. This could also be taken into consideration in field operations.

6.3 Recommendations for Future Work

The gypsum-water system can be used as an analog system to study other rock-fluid systems, such as the limestone-HCl system, sandstone-HF system, and carbonate rock-CO_2-water system. The acid number N_ac can be used as the parameter to check the analogy between the gypsum-water system and the rock-fluid system of interest. Core flood tests, with the integrated ECMS and the CT analysis before and after the tests, can be used to study the evolution of the system, the effect of experimental parameters on the dissolution of the porous matrix and the formation of wormholes.

The experimental setup can also be used to study the flow and dissolution in rock fractures. Similar to the core flood tests, fracture flow tests can be designed to study the evolution of the fracture permeability, the overall dissolution rate, and the fracture geometry. The coupled mechanical processes such as fracture compression and creep, and thermodynamic effects, for example pressure solution, can also be studied. Such tests would provide more fundamental understanding of the physical processes and at the same time shed light on practical applications such as fracture acid stimulation.

The theoretical study on the flow and dissolution in enlarged tube can be extended to fractures and pore network systems. The analytical solution for transport-controlled dissolution in a single fracture can be obtained similarly as the Graetz solution. The analytical solution, with the help of quasi-steady state approximation, can be used to predict the evolution of the fracture geometry during fracture flow. The extended Graetz solution can be applied to pore network models to more accurately simulate the reactive transport processes in porous rock matrix.

Appendix A

Acid capacity number (N_{ac}) for the gypsum-water system

By assuming that the total volume of the matrix is V_t, the initial pore volume can be expressed as:

$$\phi_0 V_t; \tag{A.1}$$

where ϕ_0 is the initial porosity. The mass of solid that can be dissolved by the volume $\phi_0 V_t$ pore fluid is:

$$\phi_0 V_t C_{eq} \tag{A.2}$$

where $C_{eq}[M/L^3]$ is the equilibrium concentration of the gypsum in water. The mass of the matrix is:

$$(1 - \phi_0) V_t \cdot \rho_s; \tag{A.3}$$

where ρ_s is the density of the mineral. The above derivation yields the acid capacity number:

$$N_{ac} = \frac{\phi_0 C_{eq}}{(1 - \phi_0)\rho_s}. \tag{A.4}$$

Appendix B

Graetz Solution

The steady-state mass conservation for transport-controlled dissolution in a cylindrical tube can be expressed as :

$$0 = -v_z \cdot \frac{\partial C}{\partial z} + D\frac{\partial^2 C}{\partial z^2} + D\frac{1}{r}\frac{\partial}{\partial r}\left(r\frac{\partial C}{\partial r}\right), \tag{B.1}$$

where $C = C(z, r)$ is the solute concentration and D is the diffusion coefficient of dissolved gypsum.

The boundary conditions are:

$$\frac{\partial C}{\partial r}|_{r=0} = 0 \quad \text{(axisymmetric boundary condition)} \tag{B.2a}$$

$$C|_{r=R_0} = C_{eq} \quad \text{(thermodynamic equilibrium boundary condition)} \tag{B.2b}$$

$$C|_{z=0} = 0 \quad \text{(concentration of dissolved gypsum at inflow)} \tag{B.2c}$$

The governing equation above can by written in dimensionless form by defining the following dimensionless quantities:

$$Z = \frac{Dz}{2R_0^2\bar{v}_z} = \frac{z}{R_0 P_e}, \quad P_e = \frac{\bar{v}_z \cdot 2R_0}{D}, \quad Y = \frac{r}{R_0} \quad \text{and} \quad \theta = \frac{C_{eq} - C}{C_{eq}}, \tag{B.3}$$

where Z is the dimensionless axial coordinate; P_e is the Péclet number; Y is the dimensionless radial coordinate; and θ is the dimensionless concentration.

Equations (B.1) and (B.2) can be rewritten with the dimensionless quantities:

$$0 = -(1-Y^2)\frac{\partial \theta}{\partial Z} + \frac{1}{P_e^2}\frac{\partial^2 \theta}{\partial Z^2} + \frac{1}{Y}\frac{\partial}{\partial Y}\left(Y\frac{\partial \theta}{\partial Y}\right) \tag{B.4a}$$

$$\frac{\partial \theta}{\partial Y}|_{Y=0} = 0 \quad \text{(symmetric boundary condition)} \tag{B.4b}$$

$$\theta|_{Y=1} = 0 \quad \text{(equilibrium boundary condition)} \tag{B.4c}$$

$$\theta|_{Z=0} = 1 \quad \text{(distilled water injection at inlet).} \tag{B.4d}$$

In Equation (B.4), the Péclet number is the ratio of the mass transfer rate by advection to that by diffusion. For cases with a Péclet number $P_e \geq 100$, the axial diffusion,$\frac{1}{P_e^2}\frac{\partial^2 \theta}{\partial Z^2}$, can be safely neglected (for the effect of axial diffusion in low P_e cases, please refer to Acrivos, [1980]). The quasi-steady state form of the transport equation Equation (B.4) becomes:

$$(1-Y^2)\frac{\partial \theta}{\partial Z} = \frac{1}{Y}\frac{\partial}{\partial Y}\left(Y\frac{\partial \theta}{\partial Y}\right) \tag{B.5a}$$

$$\theta|_{Y=1} = 0 \tag{B.5b}$$

$$\frac{\partial \theta}{\partial Y}|_{Y=0} = 0 \tag{B.5c}$$

$$\theta|_{Z=0} = 1 \tag{B.5d}$$

Equation (B.5) can be solved by separation of variables, which yields an infinite series solution:

$$\theta(Y, Z) = \sum_{n=0}^{\infty} A_n e^{-\lambda_n^2 Z}\phi_n(Y) \tag{B.6}$$

Where λ_n are the eigenvalues for the confluent hypergeometric function or Kummer function (often written in the form $M(a, b, x)$):

$$M(\frac{1}{2}-\frac{\lambda}{4},1,\lambda)=0. \tag{B.7}$$

$\phi_n(Y)$ is the eigenfunction, which can be expressed in terms of the Kummer's equation:

$$\phi_n(Y)=e^{-\frac{\lambda_n Y^2}{2}}M(\frac{1}{2}-\frac{\lambda_n}{4},1,\lambda_n Y^2). \tag{B.8}$$

And A_n is the coefficient in the solution by separation of variables,

$$A_n=\frac{\int_0^1 \phi_n(Y)Y(1-Y^2)dY}{\int_0^1 \phi_n^2(Y)Y(1-Y^2)dY}. \tag{B.9}$$

Given the Graetz solution of concentration (Equation (B.6)), the bulk concentration and Sherwood number can be expressed as:

$$C_b(Z)=\frac{\int_0^R 2\pi r v_z(r)C(r,z)dr}{Q}=C_{eq}+C_{eq}\cdot 4\sum_{n=1}^{\infty}A_n\frac{exp\,(-\lambda_n^2 Z)}{\lambda_n^2}\frac{\partial\phi_n}{\partial Y}|_{Y=1}; \tag{B.10}$$

$$S_h(Z)=\frac{\sum\limits_{n=1}^{\infty}A_n e^{-\lambda_n^2 Z}\frac{\partial\phi_n}{\partial Y}|_{Y=1}}{2\sum\limits_{n=1}^{\infty}A_n\frac{e^{-\lambda_n^2 Z}}{\lambda_n^2}\frac{\partial\phi_n}{\partial Y}|_{Y=1}}. \tag{B.11}$$

Appendix C

Derivation of the G and D_{ae}

The following derivation is similar to the discussion by Budek and Szymczak [2012]. To provide a consistent notation and definition, the equations are rewritten and some parameters are redefined. To simplify the formulation, the first order reaction model can be used to calculate the reaction-controlled dissolution mass flux R_r $[M/(L^2 \cdot T)]$:

$$R_r = k_r(C_{eq} - C_s), \tag{C.1}$$

where k_r $[L/T]$ is the reaction-controlled dissolution rate coefficient, $C_s[M/L^3]$ is the concentration on the surface, C_{eq} is the equilibrium concentration (solubility). If the dissolution is reaction-controlled, the diffusion is relatively fast and the concentration on the surface can be approximated by the bulk concentration C_b.

The diffusion rate for a tubular geometry with laminar flow can be calculated using the Graetz solution (Section 5.1.1)

$$R_t = k_t(C_{eq} - C_b), \tag{C.2}$$

where k_t is the transport-controlled dissolution rate coefficient and C_b is the bulk concentration in the tube. According to the Graetz solution, k_t can be estimated as:

$$k_t = \frac{S_h \cdot D}{2R}, \tag{C.3}$$

where S_h is the Sherwood number, D is the diffusivity, and R is the radius of the tube. According to Equations (C.1, C.2 and C.3), the kinetic parameter G can be expressed as:

$$G = \frac{2Rk_r}{DS_h}. \tag{C.4}$$

Similar to mixed controlled dissolution model proposed by Budek and Szymczak [2012], the effective dissolution rate coefficient is defined as:

$$k_{eff} = \frac{k_t \cdot k_r}{k_t + k_r} \tag{C.5}$$

Thus, the effective dissolution rate considering both the reaction-controlled and transport-controlled cases can be expressed as:

$$R_{eff} = k_{eff}(C_{eq} - C_b) \tag{C.6}$$

The rate of advection can be expressed as the average flow velocity $\bar{U}$. For matrix flow and tube flow, $\bar{U}$ can be expressed as:

$$\begin{aligned} \bar{U} &= q/n \text{ (matrix flow);} && \text{(C.7)} \\ \bar{U} &= Q/(\pi R_w^2) \text{ (tube flow)} && \text{(C.8)} \end{aligned}$$

Then the effective Damköhler number can be expressed as:

$$D_{ae} = \frac{k_{eff}}{\bar{U}} \tag{C.9}$$

Appendix D

Parallel Tube Modeling

Section 5.3.1 discussed the rationale behind the assumption that the effective surface area in the rock matrix is a function of the injection flux: $A_e \propto q^{0.72}$. As a simple validation to this assumption, the conceptual model of parallel tubes is used to simulate the flow and dissolution in the rock matrix. This conceptual model has been used to study the matrix dissolution and wormhole formation in limestone-acid and limestone-CO_2-water systems [Zhang et al., 2016; Wang et al., 2016]. The parallel tube model uses a large number of parallel tubes connecting the inlet and outlet, to mimic a porous medium as shown in Figure D-1. The flow and dissolution in the tubes can be explicitly calculated using the Poiseuille equation and the extended Graetz solution, respectively.

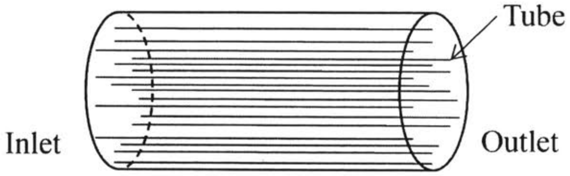

Figure D-1: Schematic of the parallel tube model.

In this validation, a 2000-tube parallel tube model is used. The tube diameters are stochastically generated based on the distribution measured using MIP (Section 3.1.3). The range of flow rates used in the core flood tests are applied to the parallel tube model. To calculate the effective surface area, the definition proposed by Wen and Li [2017] is used: the effective surface area is the area of pores, in which the pore fluid is far from equilibrium. Since the threshold value to determine if the pore fluid is far from equilibrium can be between 0.50 and 0.99 Wen and Li [2017], the threshold value of 0.60 is used. Therefore, when the concentration of the pore fluid satisfies the criterion (Equation (D.1)), the pore surface contributes to the effective surface area.

$$\frac{C}{C_{eq}} < 0.6 \; , \tag{D.1}$$

where C is the concentration of the pore fluid.

In the parallel tube model, the effective surface area is the sum of the area of the tube sections, in which the pore fluid satisfies the criterion in Equation (D.1). The effective surface is normalized to the total tube area as the effective surface ratio (A_{sR}). Since the tube diameters are stochastically generated, a Monte-Carlo scheme is used in which 100 simulations are conducted for each of the seven flow rates used in the core flood tests. The results are plotted in Figure D-2.

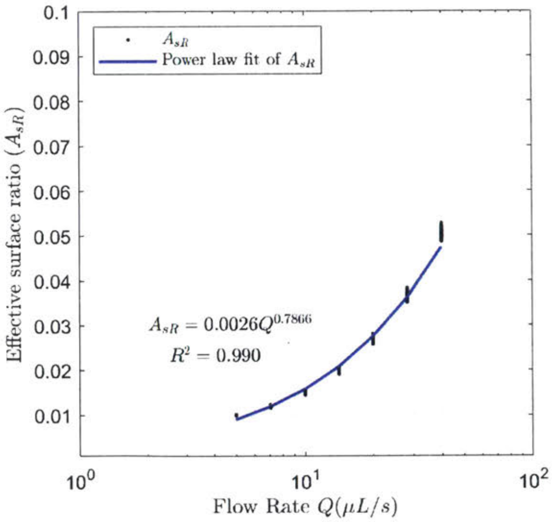

Figure D-2: Effective surface ratio as a function of the injection flow rate.

The effective surface ratio, being in the range of 0.01 to 0.05, shows that the surface area that is reactive with the pore fluid is only a small part of the total surface area, as shown in Figure D-2. This is consistent with the findings by Beckingham et al.

[2016]. The effective surface ratio increases with the increasing flow rates. A power law fit shows that the effective surface ratio is proportional to the 0.79 power of the flow rate.

It should be noted that the parallel tube model does not necessarily reflect the complex flow field and dissolution in the rock matrix. Instead, it is a simplified representation of the flow and dissolution, which could mimic the behavior of the system. The parallel tube model is used here only to prove the concept that the effective surface area is larger when the flow rate is higher. The proposed relation between the effective surface area and flow rate (Equation (5.43)) as used in Section 5.3.3 to model the effluent concentration throughout the core flood tests.

Bibliography

A.C.E.S. (2009). Geotechnical investigation for 15.3 km of mainland link sewers between officer city and al wathba project, abu dhabi, uae. Technical report. in S08000364 - Link Sewer Contract.

Al-Khulaifi, Y., Lin, Q., Blunt, M. J., and Bijeljic, B. (2018). Reservoir-condition pore-scale imaging of dolomite reaction with supercritical co_2 acidified brine: Effect of pore-structure on reaction rate using velocity distribution analysis. *International Journal of Greenhouse Gas Control*, 68:99–111.

Alsharhan, A. and Kendall, C. S. C. (2003). Holocene coastal carbonates and evaporites of the southern arabian gulf and their ancient analogues. *Earth-Science Reviews*, 61(3-4):191–243.

Ameli, P., Elkhoury, J. E., Morris, J. P., and Detwiler, R. L. (2014). Fracture permeability alteration due to chemical and mechanical processes: a coupled high-resolution model. *Rock mechanics and rock engineering*, 47(5):1563–1573.

Barton, A. and Wilde, N. (1971). Dissolution rates of polycrystalline samples of gypsum and orthorhombic forms of calcium sulphate by a rotating disc method. *Transactions of the Faraday Society*, 67:3590–3597.

Bekri, S., Thovert, J.-F., and Adler, P. (1997). Dissolution and deposition in fractures. *Engineering Geology*, 48(3-4):283–308.

Benito, G., Del Campo, P. P., Gutiérrez-Elorza, M., and Sancho, C. (1995). Natural and human-induced sinkholes in gypsum terrain and associated environmental problems in ne spain. *Environmental Geology*, 25(3):156–164.

Berkowitz, B. (2002). Characterizing flow and transport in fractured geological media: A review. *Advances in water resources*, 25(8-12):861–884.

Berkowitz, B. and Zhou, J. (1996). Reactive solute transport in a single fracture. *Water Resources Research*, 32(4):901–913.

Bernabé, Y. (1995). The transport properties of networks of cracks and pores. *Journal of Geophysical Research: Solid Earth*, 100(B3):4231–4241.

Bernabé, Y. (1996). Self-organized fluid flow through heterogeneous networks. *Geophysical research letters*, 23(21):3039–3042.

Bird, R. B., Stewart, W. E., and Lightfoot, E. N. (2007). *Transport phenomena*. John Wiley & Sons.

Birk, S., Liedl, R., Sauter, M., and Teutsch, G. (2003). Hydraulic boundary conditions as a controlling factor in karst genesis: A numerical modeling study on artesian conduit development in gypsum. *Water Resources Research*, 39(1).

Bögli, A. (2012). *Karst hydrology and physical speleology*. Springer Science & Business Media.

Briggs, S., Karney, B. W., and Sleep, B. E. (2017). Numerical modeling of the effects of roughness on flow and eddy formation in fractures. *Journal of Rock Mechanics and Geotechnical Engineering*, 9(1):105–115.

Bryant, S. L., Mellor, D. W., and Cade, C. A. (1993). Physically representative network models of transport in porous media. *AIChE Journal*, 39(3):387–396.

Budek, A. and Szymczak, P. (2012). Network models of dissolution of porous media. *Physical Review E*, 86(5):056318.

Buijse, M. A. et al. (1997). Understanding wormholing mechanisms can improve acid treatments in carbonate formations. In *SPE European Formation Damage Conference*. Society of Petroleum Engineers.

Cameron, D. and Klute, A. (1977). Convective-dispersive solute transport with a combined equilibrium and kinetic adsorption model. *Water Resources Research*, 13(1):183–188.

Carman, P. C. (1939). Permeability of saturated sands, soils and clays. *The Journal of Agricultural Science*, 29(2):262–273.

Chen, J.-D. (1989). Growth of radial viscous fingers in a hele-shaw cell. *Journal of Fluid Mechanics*, 201:223–242.

Christoffersen, M. R. et al. (1976). The kinetics of dissolution of calcium sulphate dihydrate in water. *Journal of Crystal Growth*, 35(1):79–88.

Civan, F. (2015). *Reservoir formation damage*. Gulf Professional Publishing.

Cohen, C. E., Ding, D., Quintard, M., and Bazin, B. (2008). From pore scale to wellbore scale: Impact of geometry on wormhole growth in carbonate acidization. *Chemical Engineering Science*, 63(12):3088–3099.

Cooper, A. (1986). Subsidence and foundering of strata caused by the dissolution of permian gypsum in the ripon and bedale areas, north yorkshire. *Geological Society, London, Special Publications*, 22(1):127–139.

Daccord, G. (1987). Chemical dissolution of a porous medium by a reactive fluid. *Physical review letters*, 58(5):479.

Daccord, G. and Lenormand, R. (1987). Fractal patterns from chemical dissolution. *Nature*, 325(6099):41–43.

Daccord, G., Lenormand, R., and Lietard, O. (1993a). Chemical dissolution of a porous medium by a reactive fluid –i. model for the "wormholing" phenomenon. *Chemical Engineering Science*, 48(1):169–178.

Daccord, G., Lietard, O., and Lenormand, R. (1993b). Chemical dissolution of a porous medium by a reactive fluid –ii. convection vs reaction, behavior diagram. *Chemical engineering science*, 48(1):179–186.

Darcy, H. (1856). Les fontaines publiques de la ville de dijon, dalmont. *Paris: Dalmont.*

Deng, H., Fitts, J. P., and Peters, C. A. (2016). Quantifying fracture geometry with x-ray tomography: Technique of iterative local thresholding (tilt) for 3d image segmentation. *Computational Geosciences*, 20(1):231–244.

Detwiler, R. L. (2008). Experimental observations of deformation caused by mineral dissolution in variable-aperture fractures. *Journal of Geophysical Research: Solid Earth*, 113(B8).

Detwiler, R. L. and Rajaram, H. (2007). Predicting dissolution patterns in variable aperture fractures: Evaluation of an enhanced depth-averaged computational model. *Water resources research*, 43(4).

Detwiler, R. L., Rajaram, H., and Glass, R. J. (2001). Nonaqueous-phase-liquid dissolution in variable-aperture fractures: Development of a depth-averaged computational model with comparison to a physical experiment. *Water Resources Research*, 37(12):3115–3129.

Dijk, P. and Berkowitz, B. (1998). Precipitation and dissolution of reactive solutes in fractures. *Water Resources Research*, 34(3):457–470.

Dreybrodt, W. (1996). Principles of early development of karst conduits under natural and man-made conditions revealed by mathematical analysis of numerical models. *Water Resources Research*, 32(9):2923–2935.

Economides, M. J., Nolte, K. G., et al. (1989). *Reservoir stimulation*, volume 2. Prentice Hall Englewood Cliffs, NJ.

Einstein, H., Hirschfeld, R., Nelson, R., Bruhn, R., et al. (1969). Model studies of jointed-rock behavior. In *The 11th US Symposium on Rock Mechanics (USRMS)*. American Rock Mechanics Association.

Elkhoury, J. E., Ameli, P., and Detwiler, R. L. (2013). Dissolution and deformation in fractured carbonates caused by flow of co2-rich brine under reservoir conditions. *International Journal of Greenhouse Gas Control*, 16:S203–S215.

Faisal, T. F., Chevalier, S., Bernabe, Y., Juanes, R., and Sassi, M. (2015). Quantitative and qualitative study of density driven co2 mass transfer in a vertical hele-shaw cell. *International Journal of Heat and Mass Transfer*, 81:901–914.

Falconer, K. (2004). *Fractal geometry: mathematical foundations and applications*. John Wiley & Sons.

Ford, D. and Williams, P. D. (2013). *Karst hydrogeology and geomorphology*. John Wiley & Sons.

Frash, L., Carey, J., Ickes, T., et al. (2018). Fracturing, fluid flowing, and x-ray imaging through anhydrite at stressed conditions. In *52nd US Rock Mechanics/Geomechanics Symposium*. American Rock Mechanics Association.

Fredd, C. N. and Fogler, H. S. (1998). Influence of transport and reaction on wormhole formation in porous media. *AIChE journal*, 44(9):1933–1949.

Gabrovšek, F. and Dreybrodt, W. (2001). A model of the early evolution of karst aquifers in limestone in the dimensions of length and depth. *Journal of Hydrology*, 240(3-4):206–224.

Germaine, J. T. and Germaine, A. V. (2009). *Geotechnical laboratory measurements for engineers*. John Wiley & Sons.

Gidley, J. L. (1985). Acidizing sandstone formations: A detailed examination of recent experience. In *SPE Annual Technical Conference and Exhibition*. Society of Petroleum Engineers.

Giesche, H. (2006). Mercury porosimetry: a general (practical) overview. *Particle & particle systems characterization*, 23(1):9–19.

Gobran, G. R. and Miyamoto, S. (1985). DISSOLUTION RATE OF GYPSUM IN AQUEOUS SALT SOLUTIONS. *Soil science*, 140(2):89–93.

Gomaa, A. M. and Nasr-El-Din, H. A. (2010). New insights into the viscosity of polymer-based in-situ-gelled acids. *SPE Production & Operations*, 25(03):367–375.

Graetz, v. L. (1882). Ueber die wärmeleitungsfähigkeit von flüssigkeiten. *Annalen der Physik*, 254(1):79–94.

Groves, C. G. and Howard, A. D. (1994a). Early development of karst systems: 1. preferential flow path enlargement under laminar flow. *Water Resources Research*, 30(10):2837–2846.

Groves, C. G. and Howard, A. D. (1994b). Minimum hydrochemical conditions allowing limestone cave development. *Water Resources Research*, 30(3):607–615.

Guo, J., Veran-Tissoires, S., and Quintard, M. (2016). Effective surface and boundary conditions for heterogeneous surfaces with mixed boundary conditions. *Journal of Computational Physics*, 305:942–963.

Hanna, R. B. and Rajaram, H. (1998). Influence of aperture variability on dissolutional growth of fissures in karst formations. *Water Resources Research*, 34(11):2843–2853.

Hoefner, M. and Fogler, H. S. (1988). Pore evolution and channel formation during flow and reaction in porous media. *AIChE Journal*, 34(1):45–54.

Howard, A. D. and Groves, C. G. (1995). Early development of karst systems: 2. turbulent flow. *Water Resources Research*, 31(1):19–26.

Innorta, G., Rabbi, E., and Tomadin, L. (1980). The gypsum-anhydrite equilibrium by solubility measurements. *Geochimica et Cosmochimica Acta*, 44(12):1931–1936.

Izgec, O. (2009). *Reactive flow in vuggy carbonates: Methods and models applied to matrix acidizing of carbonates.* Texas A&M University.

James, A. N. and Lupton, A. R. R. (1978). Gypsum and anhydrite in foundations of hydraulic structures. *Geotechnique*, 28(3):249–272.

Jeschke, A. A., Vosbeck, K., and Dreybrodt, W. (2001). Surface controlled dissolution rates of gypsum in aqueous solutions exhibit nonlinear dissolution kinetics. *Geochimica et Cosmochimica Acta*, 65(1):27–34.

Johnson, K. S. (2008). Gypsum-karst problems in constructing dams in the usa. *Environmental geology*, 53(5):945–950.

Kalia, N. and Balakotaiah, V. (2007). Modeling and analysis of wormhole formation in reactive dissolution of carbonate rocks. *Chemical Engineering Science*, 62(4):919–928.

Kang, P. K., Brown, S., and Juanes, R. (2016). Emergence of anomalous transport in stressed rough fractures. *Earth and Planetary Science Letters*, 454:46–54.

Kaufmann, G. and Romanov, D. (2008). Cave development in the swabian alb, south-west germany: A numerical perspective. *Journal of hydrology*, 349(3):302–317.

Keisling, T., Rao, P., and Jessup, R. (1978). Pertinent criteria for describing the dissolution of gypsum beds in flowing water. *Soil Science Society of America Journal*, 42(2):234–236.

Kemper, W., Olsen, J., DeMooy, C., et al. (1975). Dissolution rate of gypsum in flowing water 1. *Soil Science Society of America Journal*, 39(3):458–463.

Levich, V. G. (1962). *Physicochemical hydrodynamics.* Prentice-Hall Inc.

Li, L., Maher, K., Navarre-Sitchler, A., Druhan, J., Meile, C., Lawrence, C., Moore, J., Perdrial, J., Sullivan, P., Thompson, A., et al. (2017). Expanding the role of reactive transport models in critical zone processes. *Earth-Science Reviews*, 165:280–301.

Li, L., Peters, C. A., and Celia, M. A. (2006). Upscaling geochemical reaction rates using pore-scale network modeling. *Advances in water resources*, 29(9):1351–1370.

Li, L., Steefel, C. I., and Yang, L. (2008). Scale dependence of mineral dissolution rates within single pores and fractures. *Geochimica et Cosmochimica Acta*, 72(2):360–377.

Li, W. and Einstein, H. H. (2017). Theoretical and numerical investigation of the cavity evolution in gypsum rock. *Water Resources Research*, 53(11):9988–10001.

Lienhard, J. H. (2013). *A heat transfer textbook.* Courier Corporation.

Liu, S.-T. and Nancollas, G. H. (1970). The kinetics of crystal growth of calcium sulfate dihydrate. *Journal of Crystal Growth*, 6(3):281–289.

Liu, S.-T. and Nancollas, G. H. (1971). The kinetics of dissolution of calcium sulfate dihydrate. *Journal of Inorganic and Nuclear Chemistry*, 33(8):2311–2316.

Liu, S.-T. and Nancollas, G. H. (1973). The crystal growth of calcium sulfate dihydrate in the presence of additives. *Journal of Colloid and Interface Science*, 44(3):422–429.

Liu, X., Zhao, G., et al. (2005). A fractal wormhole model for cold heavy oil production. *Journal of Canadian Petroleum Technology*, 44(09).

Lowell, R. P., Van Cappellen, P., and Germanovich, L. N. (1993). Silica precipitation in fractures and the evolution of permeability in hydrothermal upflow zones. *Science*, 260(5105):192–194.

Mandelbrot, B. B. (1982). *The fractal geometry of nature*, volume 2. WH freeman New York.

McLeod, H. O. (1984). Matrix acidizing. *Journal of Petroleum Technology*, 36(12):2–055.

Ming, L., Zhang, S., and Jianye, M. (2012). Fractal nature of acid-etched wormholes and the influence of acid type on wormholes. *Petroleum Exploration and Development*, 39(5):630–635.

Mohamed, I. M., He, J., and Nasr-El-Din, H. A. (2013). Experimental analysis of co2 injection on permeability of vuggy carbonate aquifers. *Journal of Energy Resources Technology*, 135(1):013301.

Moukalled, F., Mangani, L., Darwish, M., et al. (2016). *The finite volume method in computational fluid dynamics*. Springer.

Muljadi, B. P., Blunt, M. J., Raeini, A. Q., and Bijeljic, B. (2016). The impact of porous media heterogeneity on non-darcy flow behaviour from pore-scale simulation. *Advances in water resources*, 95:329–340.

Navas, A. (1990). The effect of hydrochemical factors on the dissolution rate of gypsiferous rocks in flowing water. *Earth Surface Processes and Landforms*, 15(8):709–715.

Nitters, G., Roodhart, L., Jongma, H., Yeager, V., Buijse, M., Fulton, D., Dahl, J., Jantz, E., et al. (2000). Structured approach to advanced candidate selection and treatment design of stimulation treatments. In *SPE Annual Technical Conference and Exhibition*. Society of Petroleum Engineers.

Noiriel, C. (2015). Resolving time-dependent evolution of pore-scale structure, permeability and reactivity using x-ray microtomography. *Reviews in Mineralogy and Geochemistry*, 80(1):247–285.

Noiriel, C., Bernard, D., Gouze, P., and Thibault, X. (2005). Hydraulic properties and microgeometry evolution accompanying limestone dissolution by acidic water. *Oil & gas science and technology*, 60(1):177–192.

Noiriel, C., Luquot, L., Madé, B., Raimbault, L., Gouze, P., and Van Der Lee, J. (2009). Changes in reactive surface area during limestone dissolution: An experimental and modelling study. *Chemical Geology*, 265(1-2):160–170.

Ohmoto, H., Hayashi, K., Onuma, K., Tsukamoto, K., Kitakaze, A., Nakano, Y., and Yamamoto, Y. (1991). Solubility and reaction kinetics of solution–solid reactions determined by in situ observations. *Nature*, 351(6328):634.

Oka, S. and Takami, A. (1967). The steady slow motion of a non-newtonian liquid through a tapered tube. *Japanese Journal of Applied Physics*, 6(4):423–426.

Osselin, F., Kondratiuk, P., Budek, A., Cybulski, O., Garstecki, P., and Szymczak, P. (2016). Microfluidic observation of the onset of reactive-infitration instability in an analog fracture. *Geophysical Research Letters*, 43(13):6907–6915.

Pashin, J. C. and Dodge, R. L. (2010). Carbon dioxide sequestration in geological mediaâĂŤstate of the science. *Carbon dioxide sequestration in geological media: State of the Science, AAPG Studies in Geology*, 59:59.

Pyrak-Nolte, L. and Morris, J. (2000). Single fractures under normal stress: The relation between fracture specific stiffness and fluid flow. *International Journal of Rock Mechanics and Mining Sciences*, 37(1-2):245–262.

Raines, M. A. and Dewers, T. A. (1997). Mixed transport/reaction control of gypsum dissolution kinetics in aqueous solutions and initiation of gypsum karst. *Chemical Geology*, 140(1):29–48.

Ramsay, W. B. (1996). *A modified triaxial permeameter for physical characterization of parameters affecting contaminant transport through wetland deposits.* PhD thesis, Massachusetts Institute of Technology.

Romanov, V., Soong, Y., Carney, C., Rush, G. E., Nielsen, B., and O'Connor, W. (2015). Mineralization of carbon dioxide: A literature review. *ChemBioEng Reviews*, 2(4):231–256.

Sagan, H. (2012). *Space-filling curves.* Springer Science & Business Media.

Sakhaee-Pour, A. and Bryant, S. (2012). Gas permeability of shale. *SPE Reservoir Evaluation & Engineering*, 15(04):401–409.

Seiphoori, A., Whittle, A. J., Krakowiak, K. J., and Einstein, H. H. (2017). Insights into diagenesis and pore structure of opalinus shale through comparative studies of natural and reconstituted materials. *Clays and Clay Minerals*, 65(2):135–153.

Smith, M. M., Hao, Y., and Carroll, S. (2017). Development and calibration of a reactive transport model for carbonate reservoir porosity and permeability changes based on co2 core-flood experiments. *International Journal of Greenhouse Gas Control*, 57:73–88.

Smith, M. M., Hao, Y., Mason, H. E., and Carroll, S. A. (2014). Experiments and modeling of variably permeable carbonate reservoir samples in contact with co2-acidified brines. *Energy Procedia*, 63(C).

Smith, M. M., Sholokhova, Y., Hao, Y., and Carroll, S. A. (2013). Co $_2$ -induced dissolution of low permeability carbonates. part i: Characterization and experiments. *Advances in Water Resources*, 62:370–387.

Soulaine, C., Roman, S., Kovscek, A., and Tchelepi, H. A. (2017). Mineral dissolution and wormholing from a pore-scale perspective. *Journal of Fluid Mechanics*, 827:457–483.

Steefel, C. I., DePaolo, D. J., and Lichtner, P. C. (2005). Reactive transport modeling: An essential tool and a new research approach for the earth sciences. *Earth and Planetary Science Letters*, 240(3-4):539–558.

Steefel, C. I. and Lichtner, P. C. (1998). Multicomponent reactive transport in discrete fractures: I. controls on reaction front geometry. *Journal of Hydrology*, 209(1-4):186–199.

Sudicky, E. and Frind, E. (1982). Contaminant transport in fractured porous media: Analytical solutions for a system of parallel fractures. *Water Resources Research*, 18(6):1634–1642.

Sudicky, E. A. and Frind, E. O. (1984). Contaminant Transport in Fractured Porous

Media: Analytical Solution for a Two-Member Decay Chain in a Single Fracture. *Water Resources Research*, 20(7):1021–1029.

Szulczewski, M., Hesse, M., and Juanes, R. (2013). Carbon dioxide dissolution in structural and stratigraphic traps. *Journal of Fluid Mechanics*, 736:287–315.

Szulczewski, M. L., MacMinn, C. W., Herzog, H. J., and Juanes, R. (2012). Lifetime of carbon capture and storage as a climate-change mitigation technology. *Proceedings of the National Academy of Sciences*, 109(14):5185–5189.

Szymczak, P. and Ladd, A. (2004). Microscopic simulations of fracture dissolution. *Geophysical research letters*, 31(23).

Szymczak, P. and Ladd, A. (2006). A network model of channel competition in fracture dissolution. *Geophysical Research Letters*, 33(5).

Szymczak, P. and Ladd, A. (2009). Wormhole formation in dissolving fractures. *Journal of Geophysical Research: Solid Earth*, 114(B6).

Szymczak, P. and Ladd, A. J. (2012). Reactive-infiltration instabilities in rocks. fracture dissolution. *Journal of Fluid Mechanics*, 702:239–264.

Tang, D., Frind, E., and Sudicky, E. A. (1981). Contaminant transport in fractured porous media: Analytical solution for a single fracture. *Water resources research*, 17(3):555–564.

Tardy, P. M. J., Lecerf, B., Christanti, Y., et al. (2007). An experimentally validated wormhole model for self-diverting and conventional acids in carbonate rocks under radial flow conditions. In *European Formation Damage Conference*. Society of Petroleum Engineers.

Taylor, C. J. and Greene, E. A. (2008). Hydrogeologic characterization and methods used in the investigation of karst hydrology. *US Geological Survey*.

Taylor, K. and Nasr-El-Din, H. (2002). Coreflood evaluation of in-situ gelled acids. In *International Symposium and Exhibition on Formation Damage Control*. Society of Petroleum Engineers.

Van Genuchten, M. T. and Wierenga, P. (1976). Mass transfer studies in sorbing porous media i. analytical solutions 1. *Soil Science Society of America Journal*, 40(4):473–480.

Vicsek, T. (1992). *Fractal growth phenomena*. World scientific.

Wang, H., Bernabé, Y., Mok, U., and Evans, B. (2016). Localized reactive flow in carbonate rocks: Core-flood experiments and network simulations. *Journal of Geophysical Research: Solid Earth*, 121(11):7965–7983.

Witherspoon, P. A., Wang, J. S., Iwai, K., and Gale, J. E. (1980). Validity of cubic law for fluid flow in a deformable rock fracture. *Water resources research*, 16(6):1016–1024.

Yang, J. (2012). Reactive silica transport in fractured porous media: Analytical solution for a single fracture. *Computers & geosciences*, 38(1):80–86.

Yasuhara, H., Polak, A., Mitani, Y., Grader, A. S., Halleck, P. M., and Elsworth, D. (2006). Evolution of fracture permeability through fluid–rock reaction under hydrothermal conditions. *Earth and Planetary Science Letters*, 244(1-2):186–200.

Zerkle, R. D. and Sunderland, J. (1968). The effect of liquid solidification in a tube upon laminar-flow heat transfer and pressure drop. *Journal of Heat Transfer*, 90(2):183–189.

Zimmerman, R., Kumar, S., and Bodvarsson, G. (1991). Lubrication theory analysis of the permeability of rough-walled fractures. *International Journal of Rock Mechanics and Mining Sciences and*, 28(4):325–331.